SPH DEM coupling for solid particle erosion

A Thesis
Submitted in partial fulfillment of
the requirements for the degree of
Doctor of Philosophy
by

Dinesh Adepu
(Roll No. 153010009)

Supervisor:
Prof. Prabhu Ramachandran

Department of Aerospace Engineering
Indian Institute of Technology Bombay
Mumbai 400076 (India)
26 December 2022

Dedicated to $\cdots$

Acceptance Certificate

Department of Aerospace Engineering
Indian Institute of Technology, Bombay

The thesis entitled "SPH DEM coupling for solid particle erosion" submitted by Dinesh Adepu (Roll No. 153010009) may be accepted for being evaluated.

Date: 26 December 2022

Prof. Prabhu Ramachandran

Declaration

I declare that this written submission represents my ideas in my own words and where others' ideas or words have been included, I have adequately cited and referenced the original sources. I declare that I have properly and accurately acknowledged all sources used in the production of this report. I also declare that I have adhered to all principles of academic honesty and integrity and have not misrepresented or fabricated or falsified any idea/data/fact/source in my submission. I understand that any violation of the above will be a cause for disciplinary action by the Institute and can also evoke penal action from the sources which have thus not been properly cited or from whom proper permission has not been taken when needed.

<div style="text-align: right">

_____

Dinesh Adepu

</div>

Date: 26 December 2022   (Roll No. 153010009)

Acknowledgements

Abstract

Table of Contents

List of Figures

List of Tables

Chapter 1

Introduction

1.1 Abrasive water jet machining

Material erosion with a high-pressure water jet with abrasives is widely found in the industry applied to design machining of metals (Llanto *et al.*, 2021), composites Alberdi *et al.* (2013). Such machining is widely known as abrasive water jet machining (AWJM). AWJM is used for cutting metallic sheet, glass, and composite materials for automobile, housing, and aircraft industries (Alberdi *et al.*, 2013; Aich *et al.*, 2014; Llanto *et al.*, 2021), respectively. Figure 1.1 describes the erosion of brittle solid due to the impact of rigid bodies in a fluid flow. To model AWJM accurately, we need to model the incoming fluid dynamics, elastic-plastic behavior of the target, rigid body dynamics of the impactor, collision handling among the impactors and between the impactor and the target, two way coupling between the fluid flow and impactor, and the elastic structure, called as fluid-structure interaction. An analytical study of AWJM is not possible as it is highly nonlinear and involves several different multi-physical processes. Therefore, we choose

Figure 1.1

1

numerical modeling due to its flexibility in handling nonlinear behavior. Test cases with exact analytical solutions and experimental cases can be used to develop numerical techniques while handling each physical process. Mesh-based and meshless techniques are used to model the AWJM numerically.

1.2   State of the art

Modeling of fluid and elastic dynamics in SPH

The smoothed particle hydrodynamics (SPH) method has been widely applied since it was originally proposed to simulate hydrodynamic problems in astrophysics independently by Lucy (1977), and Gingold and Monaghan (1977a). It has been extensively applied to simulate problems involving fluids (Dalrymple and Knio, 2001; Shao and Lo, 2003) in particular to both compressible (Monaghan, 2005a), incompressible fluid flows (Monaghan, 1994; Cummins and Rudman, 1999) as well as elastic dynamics problems (Randles and Libersky, 1996; Gray *et al.*, 2001b), fluid-structure interaction (Khayyer *et al.*, 2018; He *et al.*, 2017), granular physics (Bui *et al.*, 2008; Bui and Nguyen, 2021) among other areas. Monaghan (2012) provides a detailed review of SPH and its applications.

The SPH method is meshless and Lagrangian, and therefore particles move with the local velocity. This motion can introduce disorder in the particles and thereby significantly reduce the accuracy of the method. Xu *et al.* (2009a) proposed an approach to shift the particles so as to obtain a uniform distribution of particles. This significantly improves accuracy and the method is referred to as the Particle Shifting Technique (PST). Many different kinds of PST methods are available in the literature (Lind *et al.*, 2012; Skillen *et al.*, 2013; Huang *et al.*, 2019; Ye *et al.*, 2019). An alternative approach that ensures particle homogenization for incompressible fluid flow was proposed as the Transport Velocity Formulation (TVF) (Adami *et al.*, 2013a). The method introduced an additional stress term to account for the motion introduced by the particle shifting. The TVF produces very accurate results but only works for internal flows. Zhang *et al.* (2017b) proposed the Generalized Transport Velocity Formulation (GTVF) thereby allowing the TVF to be used for free-surface problems as well as elastic dynamics problems. This allows for a unified treatment of both fluids and solids. Similarly, Oger *et al.* (2016) introduce ideas from a consistent ALE formulation for improving the accuracy of SPH. They employ a Riemann-based formulation to solve fluid mechanics problems and introduce particle shifting to obtain highly accurate simulations for internal and free-surface problems may also be handled. The PST has also been employed in the context of the δ-SPH schemes(Sun *et al.*, 2019a).

The Entropically Damped Artificial Compressibility SPH scheme (EDAC-SPH) (Ramachandran and Puri, 2019) introduces an evolution equation for the pressure and significantly reduces the noise in the pressure since it features a pressure diffusion term. The approach has a thermodynamic justification (Clausen, 2013) and produces very accurate results (Ramachandran and Puri, 2019).

Recently, Antuono *et al.* (2021) carefully combine the ALE-SPH method of Oger *et al.* (2016) and the consistent δ-SPH formulation of Sun *et al.* (2019a) to improve the accuracy of the δ-SPH method. They show the importance of the additional terms to the accuracy.

Modeling of elastic solids in SPH was first proposed by Libersky and Petschek (1991), where the authors studied the high-speed impact problems. Despite SPH being applied to elastic solid modeling, it suffers from tensile instability (Swegle *et al.*, 1995). The tensile instability problem has given rise to the total Lagrangian SPH (Bonet and Kulasegaram, 2002; Vignjevic *et al.*, 2006; Belytschko *et al.*, 2000), where the derivatives of particle properties are computed in the reference configuration using the deformation gradient. The updated Lagrangian approach is used by Gray *et al.* (2001a) and Monaghan (2000) where an artificial stress term is introduced to control instabilities. Many other variants of the updated Lagrangian SPH have been proposed. Godunov SPH (Sugiura and Inutsuka, 2017) utilizes a Riemann solver to reduce the usage of artificial viscosity and a new equation of state is formulated to solve the tensile instability problem. Dyka and Ingel (1995) uses two sets of particles, where one set of particles stress is computed, and the other set of particles are used for the evolution of other properties, through which the tensile instability has been overcome. Zhang *et al.* (2017a) extended the transport velocity formulation (TVF) of Adami *et al.* (2013b) to structural dynamics problems and free-surface fluid mechanics problems. Here the particles are moved with a transport velocity rather than the momentum velocity to ensure a more homogeneous particle distribution. This approach also solves the tensile instability problem.

Collision SPH

The dynamics of the projectiles can be modeled by assuming the bodies to be rigid, as done in the discrete element method (DEM) ((Zhan *et al.*, 2021)). However, this does not consider any elastic or elastic-plastic deformations of these colliding bodies. In these cases either finite element methods (FEM) (Rodrigues *et al.*, 2019) or meshless methods such as material point method(Sulsky *et al.*, 1994) or smoothed particle hydrodynamics (SPH) (Gingold and Monaghan, 1977b) can be used. In this context meshless methods,

such as the SPH method, are advantageous when modeling large deformation of solids as they do not suffer from issues such as mesh entanglement.

SPH has been successful in modeling the collision between the elastic as well as elastic-plastic solids (Gray *et al.*, 2001a; Cleary, 2010). Yan *et al.* (2021) introduced the interfacial SPH scheme, where the SPH forces are computed only within each body but the interaction between two bodies is computed using a repulsive force inspired from ABAQUS. Vyas *et al.* (2021) has modeled the interaction between a rigid body with an elastic solid, using a penalty-based contact force model. Mohseni-Mofidi *et al.* (2021) use a contact model in order to simulate the collision between non-smooth rigid bodies with elasto-plastic targets. In both (Vyas *et al.*, 2021) and (Mohseni-Mofidi *et al.*, 2021) the friction between the rigid body and target is considered.

Fluid-structure interaction

The interaction between the ductile target and the incoming jet can be considered as a fluid-structure interaction phenomenon. Mesh-based schemes such as finite element method (FEM) (Lozovskiy *et al.*, 2015) and finite volume method (FVM) (Jasak, 2007) have been used for the last few decades in modeling the FSI problems. However, mesh-based methods are not favorable when dealing with free surface flow problems or problems involving large deformation of the structure. This is due to explicit free surface tracking, and mesh distortion (Moresi *et al.*, 2003) while dealing with large deformation solids. Therefore, meshless methods are preferred while handling FSI problems involving free surfaces, multiphase flows, and large deformation in solids. The smoothed particle hydrodynamics (SPH) and material point method (MPM) are more commonly used to model the fluid phase. While the solids are modeled with SPH or Reproducing Kernel Particle Methods (RKPM), or the Discrete Element Method (DEM) (Hu *et al.*, 2010; Li *et al.*, 2022). These meshless techniques have been coupled for the past two decades to model the fluid-structure interaction. A few schemes with SPH and MPM are SPH-DEM (Wu *et al.*, 2016), SPH-TLSPH (Salehizadeh and Shafiei, 2022), SPH-RKPM (Peng *et al.*, 2021), SPH-Peridynamics (Sun *et al.*, 2020), MPM-DEM (Singer *et al.*, 2022). For more, see the review by (Khayyer *et al.*, 2022).

Rigid-fluid coupling and rigid-rigid interaction

Assuming the incoming projectiles as rigid bodies, the influence of rigid body on the incoming jet and vice versa is modeled as rigid fluid coupling. In rigid fluid coupling problems, mesh-based schemes (Dettmer and PeriÄĞ, 2006) have been in practice to model

fluid dynamics for several decades. However, these schemes are unfavorable when deal-
ing with free surface flows and mediums undergoing huge deformation (Walkley *et al.*,
2005). Meshless methods have been advantageous in modeling free surfaces and large
deformations problems. Therefore, meshless techniques are preferred in addressing these
problems. Among many meshless techniques, moving particle semi-implicit (MPS) - dis-
crete element method (DEM) (Guo *et al.*, 2017) and smoothed particle hydrodynamics
(SPH)-DEM (Canelas *et al.*, 2016) are two coupling strategies used to handle rigid-fluid
coupling problems. The rigid body interaction is modeled with DEM. In addition to
DEM, works where SPH (Amicarelli *et al.*, 2015) is used to model the rigid-rigid interac-
tion. However, it lacks to incorporate the friction between the bodies. MPS and SPH are
used to model the fluid phase, and a coupling strategy is utilized to model the interaction
between the rigid body and the fluid phase.

   Cundall and Strack (1979) proposed DEM to study discrete granular materials. In
DEM, the particle dynamics follow simple Newtonian force laws and interact at their sur-
faces through a contact force. A shape, mass, and moment of inertia are assigned to each
particle, and originally the particles are assumed to have a spherical shape. Variations of
the DEM were proposed to handle bodies with different shapes, such as dilated polyhedral
DEM Liu and Ji (2020), Fourier series-based discrete element method Lai *et al.* (2020)
Gilbert-Johnson-Keerthi(GJK)-DEM (Wachs *et al.*, 2012), discrete function representa-
tion based DEM (Lu *et al.*, 2012), level set DEM method (Duriez and Bonelli, 2021). In-
teraction between bodies with irregular geometries is modeled by multi-sphere approach
(Kruggel-Emden *et al.*, 2008), surface mesh represented(SMR)-DEM Zhan *et al.* (2021).

Solid particle erosion

In theoretical studies, Finnie (1972), Bitter (1963) studied the surface erosion of ductile
and brittle materials. An analytical expression for the material removal at different an-
gles of impact is derived in these studies. Further, an analytical study is carried out by
Hutchings (1977), who provides various results relating the crater depth, erosion rate re-
lated to the impactor particles. In numerical modeling, mesh based methods are in use for
the past few decades in modeling the solid particle erosion. Molinari and Ortiz (2002);
Takaffoli and Papini (2009) has studied the single impact problem using FEM. Meshless
techniques are been used in studying the erosion process, this is due to its advantage in
handling problems with large deformation. Dong *et al.* (2016) uses smoothed particle
hydrodynamics (SPH) to model the erosion of a ductile target.

1.3 Motivation

Numerical modeling of fluid and elastic dynamics in SPH

SPH in modeling fluid and structural dynamics. Faces several issues and many different additions were proposed to solve the issues. Transport velocity formulation is used extensively to solve the particle homogenization problems. With the notable exception of the GTVF scheme (Zhang *et al.*, 2017b), most other applications of the PST have been in the context of fluid mechanics. The GTVF method provides a unified approach to solve both weakly-compressible fluids as well as solids. However, the method suffers from a few issues. In order to work for free-surface problems the method relies on using a different background pressure for each particle and introduces a few numerical corrections to work around issues. For example, the smoothing length of the homogenization force is different from that used by the other equations and this parameter is somewhat ad-hoc. For solid mechanics problems the method uses the transport velocity of the particle rather than the true velocity in order to compute the strain and rotation tensor. In addition there are some terms in the governing equations that are ignored which play a major role. We also note that the method is not robust to a change in the particle homogenization force. The EDAC-SPH method uses the TVF formulation for internal flows and for free-surface flows it does not employ any form of particle shifting.

Elastic solids collision

Though, SPH (Gray *et al.*, 2001a) has been successful in modeling the collision between the elastic solids, it does not consider friction between the colliding solids. Another problem is that the model generates spurious forces on bodies which are moving close to each other (within the influence radius of the SPH particles) but not actually interacting. Yan *et al.* (2021) introduced the interfacial SPH scheme, which eliminates the spurious interactions but it can not handle friction between the solids. The interaction force does not consider the shape of the solids in contact. Mohseni-Mofidi *et al.* (2021) models the interaction between a rigid body and a ductile solid using a contact force model, where the bodies are divided as being primary and a secondary. In (Mohseni-Mofidi *et al.*, 2021), the primary body is usually treated as the rigid body and the body on which the erosion is simulated is treated as secondary. Vyas *et al.* (2021) also consider the collision between a rigid and elastic body. Vyas *et al.* (2021) where too there is a clear distinction between primary and secondary bodies. It is not clear what would happen if both bodies were elastic or if there is no clear way to distinguish between a primary and secondary body. Vyas

et al. (2021); Mohseni-Mofidi *et al.* (2021) works are not applied to model the interaction between elastic solids.

Fluid-structure interaction and rigid-fluid coupling

The dynamics of the interaction between ductile target and the incoming jet is considered as fluid-structure interaction. With meshless techniques preferred in free surface and large deformation problems. Several different meshless techniques are coupled in order to simulate the FSI phenomenon. FSI in SPH alone is modeled by several works, such as, WCSPH-Total Lagrangian SPH (TLSPH) (Zhan *et al.*, 2019), WCSPH-Updated Lagrangian SPH (ULSPH) (Antoci *et al.*, 2007), ISPH-TLSPH(Salehizadeh and Shafiei, 2022). However, using only an updated Lagrangian framework with transport velocity formulation no work is reported in modeling FSI.

Movement of arbitrarily shaped rigid projectiles are modeled using a multi-sphere and SMR-DEM approach. However, multi-sphere approach fails to handle the contact accurately with bodies involving sharp corners, as the force law assumes the contact between two spherical particles. SMR-DEM requires additional information to handle the collision, such as connectivity between the particles comprising the body in addition to the particle positions. However, we need additional sets of particles to handle the interaction between the rigid body and the fluid particles. Mohseni-Mofidi *et al.* (2021) proposed a new contact force law, which handles the collision between the bodies based on particle positions alone. Here the amount of overlap between the bodies is computed using an SPH method. Utilizing (Mohseni-Mofidi *et al.*, 2021) to model contact between the bodies allows us to handle the interaction between the fluid particles with the same set of particles in contrast to SMR-DEM Zhan *et al.* (2021). However, (Mohseni-Mofidi *et al.*, 2021) is applied to contacts involving rigid and a ductile solids. (Mohseni-Mofidi *et al.*, 2021) is not applied to model the interaction between inelastic rigid bodies, and in problems involving fluids.

Solid particle erosion

FEM (Takaffoli and Papini, 2009) is successful in modeling solid particle erosion, however, it fails to model the erosion due to many particles. Further, FEM is not suitable for modeling multiphysics problems, as AWJM has rigid fluid coupling, FSI in addition to modeling fluid and elastic dynamics. Dong *et al.* (2016) uses smoothed particle hydrodynamics (SPH) to model the erosion of a ductile target. However, Dong *et al.* (2016) does not consider the arbitrary shape of the projectile. Further, collision among the projectiles

while interacting with the target is not modeled in SPH. To the authors knowledge there is no open-source implementation in the literature which can model the solid particle erosion in SPH.

To develop an open-source framework to model the physics involved in AWJM in SPH. The following are the key goals of the work.

- Develop a unified technique in SPH to solve both fluid and solid dynamics problems.

- Handle the collision between the elastic solids using a penalty-based contact force.

- Develop a fluid-structure interaction solver.

- Handle the collision among the arbitrarily shaped rigid projectiles in fluid flow. Solve the two-way coupling between the fluid and the rigid bodies.

- Provide an open-source implementation for solid particle erosion in SPH.

In this work we propose a scheme which we called Corrected Transport Velocity Formulation (CTVF) that is inspired by the various recent developments but is consistent and which works for both solid mechanics and fluid mechanics problems. We derive the transport velocity equations afresh and note that there are some important terms that are ignored in earlier approaches using TVF. These terms are significant and improve the accuracy of the method. Similar to Oger *et al.* (2016); Sun *et al.* (2019a), we detect the free surface particles and compute their normals using a simpler and computationally efficient approach which does not require the computation of eigenvalues. This allows the method to work with free-surfaces without the introduction of numerical parameters or a variable background pressure. We employ the EDAC formulation and show that there are additional correction terms in the EDAC scheme that should be introduced to improve the accuracy of the method. Furthermore, we show how the EDAC scheme can be used in the context of solid mechanics problems. We make use of the particle velocity rather than the transport velocity to compute the velocity gradient, strain, and rotation rate tensors. Our method can be used with any PST and we consider the method of Sun *et al.* (2019a) as well as the iterative PST of Huang *et al.* (2019). The method is also robust to the choice of the smoothing kernel. The resulting method works for both weakly-compressible fluids as well as solids. The new method may be thought of as an improved extension of the EDAC-SPH method that can be used for free-surface problems as well as solid mechanics problems.

In the current work, the collision between elastic solids is modeled using a penalty-based contact force model. Unlike the approach of Yan *et al.* (2021), the proposed contact

force model can handle friction between the solids as well. The bodies themselves are
elastic and this is simulated using the CTVF SPH method Adepu and Ramachandran
(2021). The penalty-based force considered here is the one proposed by Mohseni-Mofidi
et al. (2021). In the original model proposed by Mohseni-Mofidi *et al.* (2021), the contact
force is between a primary body and a secondary body. In Mohseni-Mofidi *et al.* (2021),
the primary body is usually treated as the rigid body and the body on which the erosion is
simulated is treated as secondary. It is not clear what would happen if both bodies were
elastic or if there is no clear way to distinguish between a primary and secondary body.
We explore the importance of choosing the primary and secondary body under collision.

In the current work, we handle FSI problems by the CTVF method, where both
fluids and solid phases are modeled using CTVF alone. We couple CTVF with DEM to
model the rigid fluid coupling problems. The fluid phase is handled using a corrected
transport velocity formulation developed by Adepu and Ramachandran (2021), which
provides smooth pressure distribution with EDAC formulation and homogeneous particle
distribution, resulting in accurate fluid modeling. While DEM is used to handle rigid-
rigid interactions and applied to 3D problems, and it is further modified to handle inelastic
collisions by introducing a damping term in the contact force equation. The interaction
between the fluid phase and rigid bodies is handled using the dummy particle approach
(Adami *et al.*, 2012).

1.4 Overview

The current thesis is organized in the following way. The current chapter introduces the
basic formalism of SPH. In the next chapter, chapter 2, we introduce corrected transport
velocity formulation in SPH and apply it to model the dynamics of fluids and elastic struc-
tures. The new formulation eliminates several issues SPH faces. Chapter 3 improvises the
collision model by incorporating a contact force model in SPH while the bodies are collid-
ing. This essentially eliminates spurious interaction between the bodies and incorporates
friction between the interacting bodies. Chapter 4 is utilized to model the interaction be-
tween the elastic structure and the incoming jet. This is modeled with coupling the solver
developed in chapter 2, here both fluid and solid phases and coupled using a dummy par-
ticle approach. In chapter 5, we study the dynamics of the projectiles onto the target in an
incoming high-speed jet. We couple CTVF with DEM to model the rigid fluid coupling
phenomenon. The interaction between the rigid bodies is handled with DEM. Chapter 6
models the solid particle erosion of the ductile body due to an impact of the projectile.
The contact force implemented in chapter 3 is used to handle the interaction between the

rigid body and the ductile solid. Johnson-Cook constitutive model is utilized to model the plasticity of the target.

In the next section we introduce the SPH methodology and show how a function, derivative and divergence operators are approximated.

1.5   Smoothed particle hydrodynamics

In the current section, we introduce the basics of smoothed particle hydrodynamics. A fundamental overview of the discrete approximations of function, derivative, and divergence is discussed. Advanced approximations are derived, keeping the conservation of quantities in mind.

1.5.1   Function approximation

The function value of a smooth function A defined over a domain Ω at point x can be written as

$$A(\mathbf{x}) = \int_{\Omega} A(\mathbf{x}') \, \delta(\mathbf{x} - \mathbf{x}') \, d\mathbf{x}'^m, \tag{1.1}$$

where $\delta(\mathbf{x} - \mathbf{x}')$ is a Dirac-delta function having the following properties,

$$\delta(\mathbf{x}) = \begin{cases} +\infty, & \mathbf{x} = \mathbf{0} \\ 0, & \mathbf{x} \neq \mathbf{0} \end{cases} \tag{1.2}$$

and

$$\int_{\Omega} \delta(\mathbf{x}) \, d\mathbf{x} = 1. \tag{1.3}$$

Here, m chosen depending on the dimension of the space, 2 and 3 for 2D and 3D space. The exact function value at x can be retrieved by the following steps,

$$A(\mathbf{x}) = \int_{\Omega} A(\mathbf{x}') \, \delta(\mathbf{x} - \mathbf{x}') \, d\mathbf{x}'$$

$$A(\mathbf{x}) = A(\mathbf{x}) \int_{\Omega} \delta(\mathbf{x} - \mathbf{x}') \, d\mathbf{x}'$$

$$A(\mathbf{x}) = A(\mathbf{x})$$

In SPH, the Dirac delta function is replaced with a compact smooth function W, chosen to be as even function. The function value of A at $\mathbf{x}$ interpolated with the smooth kernel W is given by

$$A(\mathbf{x}) = \int_{\Omega} A(\mathbf{x}') \, W(\mathbf{x} - \mathbf{x}', h) \, d\mathbf{x}' + O(h^2). \tag{1.4}$$

Here, kernel W satisfies the unity condition, given by

$$\int_{\Omega} W(\mathbf{x} - \mathbf{x}', h) \, d\mathbf{x}' = 1. \tag{1.5}$$

$$\lim_{h\to 0} W(\boldsymbol{x} - \boldsymbol{x}', h) = \delta(\boldsymbol{x} - \boldsymbol{x}', h) \tag{1.6}$$

$$W(\boldsymbol{x} - \boldsymbol{x}', h) = 0 \quad \text{when} \quad |\boldsymbol{x} - \boldsymbol{x}'| > kh \tag{1.7}$$

In the current work we have used Quintic spline in all our simulation cases. Quintic spline is given as,

$$W(r, h) = \begin{cases} \sigma_5 \left((3-q)^5 - 6(2-q)^5 + 15(1-q)^5\right), & \text{for } 0 \le q \le 1, \\ \sigma_5 \left((3-q)^5 - 6(2-q)^5\right), & \text{for } 1 < q \le 2, \\ \sigma_5 \, (3-q)^5, & \text{for } 2 < q \le 3, \\ 0, & \text{for } q > 3, \end{cases} \tag{1.8}$$

This type of interpolation leads to a 2nd order function accuracy (cite references). Much better kernels can be used to approximate the function, but that may result in negative density which we want to avoid.

Assume that the domain is discretized into N particles with mass m_i and volume dv_i. We have

$$m_j = dv_i \, \rho_i \tag{1.9}$$

Using (1.9), (1.4) is converted to discrete form as follows

$$A_i = \sum \frac{m_j}{\rho_j} A_j \, W(\mathbf{x}_i - \mathbf{x}_j, h) \tag{1.10}$$

Where A_i is the value of the field property of particle i, similarly for A_j.

1.5.2   Derivative approximation

Similarly, the continuous SPH interpolation of the derivative of a field variable is written as

$$\nabla A(\mathbf{x}) = \int_\Omega \nabla A(\mathbf{x}') \, W(\mathbf{x} - \mathbf{x}', h) \, d\mathbf{x}'^m \tag{1.11}$$

By applying integration by parts to the right hand side results in,

$$\nabla A(\mathbf{x}) = - \int_\Omega A(\mathbf{x}') \, \nabla_{\mathbf{x}'} W(\mathbf{x} - \mathbf{x}', h) \, d\mathbf{x}'^m + - \int_\Omega \nabla \left(A(\mathbf{x}') \, W(\mathbf{x} - \mathbf{x}', h)\right) \, d\mathbf{x}'^m \tag{1.12}$$

From symmetric property of the kernel W, we get the derivative of the kernel as antisymmetric and thus

$$\nabla_{\mathbf{x}'} W(\mathbf{x} - \mathbf{x}', h) = -\nabla_{\mathbf{x}} W(\mathbf{x} - \mathbf{x}', h) \tag{1.13}$$

Furthermore, using the Stokes theorem, the last term of eq. (1.12) can be written as a surface integral, the resulting equation is

$$\nabla A(\mathbf{x}) = \int_\Omega A(\mathbf{x}') \, \nabla_{\mathbf{x}} W(\mathbf{x} - \mathbf{x}', h) \, d\mathbf{x}'^m + - \int_{\partial\Omega} \left(A(\mathbf{x}') \, W(\mathbf{x} - \mathbf{x}', h)\right) \mathbf{n}_{\mathbf{x}'} \, d\Gamma(\mathbf{x}') \tag{1.14}$$

With the domain being unbounded, and with the compact support property of the kernel, the above integral becomes,

$$\nabla A(\mathbf{x}) = \int_{\Omega} A(\mathbf{x}') \, \nabla_{\mathbf{x}} W(\mathbf{x} - \mathbf{x}', h) \, d\mathbf{x}'^m. \tag{1.15}$$

The discretized form of the above integral derivative approximation is

$$\nabla A(\mathbf{x}_i) = \sum \frac{m_j}{\rho_j} A_j \, \nabla W(\mathbf{x}_i - \mathbf{x}_j, h). \tag{1.16}$$

A symmetric expression of the derivative approximation is derived by employing density, i.e,

$$\nabla(A\rho^n) = nA\rho^{n-1}\nabla\rho + \rho^n\nabla A, \tag{1.17}$$

where n is a real number. The new identity for the derivative of A is

$$\nabla A = \frac{1}{\rho^n} \left[nA\rho^{n-1}\nabla\rho + \rho^n\nabla A \right], \tag{1.18}$$

using eqs. (1.10) and (1.21), the new derivative approximation can be written as

$$\nabla A(\mathbf{x}_i) = \frac{1}{\rho^n(\mathbf{x}_i)} \sum m_j \left(A_j\rho^{n-1}(\mathbf{x}_j) - nA_i\rho^{n-1}(\mathbf{x}_i) \right) \nabla W(\mathbf{x}_i - \mathbf{x}_j, h). \tag{1.19}$$

For a symmetric derivative expression used in the current work, we chose $n = -1$, resulting in

$$\nabla A(\mathbf{x}_i) = \rho_i \sum_j m_j \left(\frac{p_i}{\rho_i^2} + \frac{p_j}{\rho_j^2} \right) \nabla W_{ij} \tag{1.20}$$

$$\nabla A(\mathbf{x}_i) = \frac{1}{\rho^n(\mathbf{x}_i)} \sum m_j \left(A_j\rho^{n-1}(\mathbf{x}_j) - nA_i\rho^{n-1}(\mathbf{x}_i) \right) \nabla W(\mathbf{x}_i - \mathbf{x}_j, h). \tag{1.21}$$

1.5.3 Divergence approximation

$$\nabla \cdot \mathbf{v}_i = \sum \frac{m_j}{\rho_j} \mathbf{v}_j \cdot \nabla W(\mathbf{x}_i - \mathbf{x}_j, h) \tag{1.22}$$

Similar to derivative approximation, we utilize the following calculus identity to,

$$\nabla \cdot (\mathbf{v}\rho^n) = \rho^n\nabla \cdot \mathbf{v} + n\rho^{n-1}\mathbf{v} \cdot \nabla\rho. \tag{1.23}$$

A discrete SPH approximation for $n = 1$ is given by,

$$\nabla \cdot (\mathbf{v}\rho^n) = \rho^n\nabla \cdot \mathbf{v} + n\rho^{n-1}\mathbf{v} \cdot \nabla\rho. \tag{1.24}$$

1.6   Summary

We gave an overview of modeling the abrasive water jet machining. After reviewing the possible techniques to simulate it through mesh-based schemes and meshless methods, due to the computational limits and ease of modeling, we chose meshless methods. Among many meshless methods, we have chosen the SPH method in the current work, and this is due to the developed software available in the group and work done in literature on SPH history. At the same time, DEM is used to model the interaction between the rigid bodies. An outline of the current thesis is set. We start with the present chapter to handle the fluid and elastic dynamics.

In the current chapter, among all the required physics to be simulated, we have chosen to handle the fluid and elastic dynamics. In the such process we introduced the equations governing the fluid and structural dynamics. We introduced the basic SPH equations and how SPH approximates functions and derivatives. SPH is applied to solve the fluid and elastic dynamics, through which better SPH approximations are discussed. We found that the SPH without any corrections has several issues, like tensile instability, and inhomogeneous particle distribution leading to poorer accuracy of the simulation. SPH has accuracy issues, and it cannot produce 2nd order accurate results.

In the next chapter, we will propose a particle shifting technique into SPH and move the particles with transport velocity rather than momentum velocity. And check solve the particle homogenization problems, tensile instability. Problems involving boundaries are handled as well.

Chapter 2

Corrected transport velocity formulation

2.1 Introduction

To model the abrasive water jet machining, in the previous chapter, we introduced the numerical method to model the fluid fluid and elastic solid phase. SPH is a meshless numerical technique, which is used to discretize the governing equations. SPH suffers from inhomogeneous particle distribution leading to poor accuracy and tensile instability. In the current chapter, we propose developments to the existing technique through a transport velocity formulation. The developed technique is applied to a different class of problems involving boundaries and free surfaces in both fluid and solid dynamics for validation.

In this current chapter, we propose a scheme which we called Corrected Transport Velocity Formulation (CTVF) that is inspired by the various recent developments but is consistent and which works for both solid mechanics and fluid mechanics problems. We derive the transport velocity equations afresh and note that there are some important terms that are ignored in earlier approaches using TVF. These terms are significant and improve the accuracy of the method. Similar to (Oger *et al.*, 2016; Sun *et al.*, 2019a), we detect the free surface particles and compute their normals using a simpler and computationally efficient approach which does not require the computation of eigenvalues. This allows the method to work with free-surfaces without the introduction of numerical parameters or a variable background pressure. We employ the EDAC formulation and show that there are additional correction terms in the EDAC scheme that should be introduced to improve the accuracy of the method. Furthermore, we show how the EDAC scheme can be used in the context of solid mechanics problems. We make use of the particle velocity rather than the

transport velocity to compute the velocity gradient, strain, and rotation rate tensors. Our method can be used with any PST and we consider the method of Sun *et al.* (2019a) as well as the iterative PST of Huang *et al.* (2019). The method is also robust to the choice of the smoothing kernel. The resulting method works for both weakly-compressible fluids as well as solids. The new method may be thought of as an improved extension of the EDAC-SPH method that can be used for free-surface problems as well as solid mechanics problems.

The method is implemented using the PySPH framework (Ramachandran, 2016; Ramachandran *et al.*, 2020). The source code for all the problems demonstrated in this manuscript is made available at `https://gitlab.com/pypr/ctvf`. Every result produced in the manuscript is fully automated using the `automan` package (Ramachandran, 2018a).

We next discuss the formulation for fluid mechanics as well as solid mechanics along with the use of particle shifting. The consistent correction terms are derived. We then consider a suite of benchmark problems for both fluids and solids and compare our results with those of other methods where applicable.

2.2   Governing equations

For elastic dynamics we use the same equations as in (Gray *et al.*, 2001b; Zhang *et al.*, 2017b) which we summarize below. The governing equations of motion involve the conservation of mass, which in Lagrangian form is,

$$\frac{d\rho}{dt} = -\rho \, \frac{\partial u_i}{\partial x_i}, \tag{2.1}$$

and conservation of linear momentum,

$$\frac{du_i}{dt} = \frac{1}{\rho} \, \frac{\partial \sigma_{ij}}{\partial x_j} + g_i, \tag{2.2}$$

where ρ is the density, u_i is the ith component of the velocity field, x_j is the jth component of the position vector, g_i is the component of body force per unit mass and σ_{ij} is stress tensor.

The stress tensor is split into isotropic and deviatoric parts,

$$\sigma_{ij} = -p \, \delta_{ij} + \sigma'_{ij}, \tag{2.3}$$

where p is the pressure, δ_{ij} is the Kronecker delta function, and σ'_{ij} is the deviatoric stress.

The Jaumann's formulation for Hooke's stress provides us with the rate of change of deviatoric stress,

$$\frac{d\sigma'_{ij}}{dt} = 2G(\dot{\epsilon}_{ij} - \frac{1}{3}\dot{\epsilon}_{kk}\delta_{ij}) + \sigma'_{ik}\Omega_{jk} + \Omega_{ik}\sigma'_{kj}, \tag{2.4}$$

where G is the shear modulus, $\dot{\epsilon}_{ij}$ is the strain rate tensor,

$$\dot{\epsilon}_{ij} = \frac{1}{2}\left(\frac{\partial u_i}{\partial x_j} + \frac{\partial u_j}{\partial x_i}\right),\tag{2.5}$$

and Ω_{ij} is the rotation tensor,

$$\Omega_{ij} = \frac{1}{2}\left(\frac{\partial u_i}{\partial x_j} - \frac{\partial u_j}{\partial x_i}\right).\tag{2.6}$$

For a weakly-compressible or incompressible fluid, a viscous force is added:

$$\sigma_{ij} = -p\delta_{ij} + 2\eta\frac{\partial u_i}{\partial x_j}\tag{2.7}$$

where η is the kinematic viscosity of the fluid.

In both fluid and solid modelling the pressure is computed using an isothermal equation of state, given as,

$$p = K\left(\frac{\rho}{\rho_0} - 1\right),\tag{2.8}$$

where $K = \rho_0 c_0^2$ is the bulk modulus. Here, the constants c_0 and ρ_0 are the reference speed of sound and density, respectively. For solids, c_0 is computed as $\sqrt{\frac{E}{3(1-2\nu)\rho_0}}$, ν is the Poisson ratio.

2.3   Numerical method

Following the TVF (Adami *et al.*, 2013a) and similar formulations (Oger *et al.*, 2016), we move the particles with a *transport velocity*, $\tilde{\mathbf{u}}$. The material derivative in this case is written as,

$$\frac{\tilde{d}}{dt} = \frac{\partial}{\partial t} + \tilde{u}_j\frac{\partial}{\partial x_j}.\tag{2.9}$$

We therefore recast the governing equations to incorporate the transport velocity starting with the conservation of mass, equation (5.57),

$$\frac{\tilde{d}\rho}{dt} = -\rho\frac{\partial u_j}{\partial x_j} + (\tilde{u}_j - u_j)\frac{\partial\rho}{\partial x_j}.\tag{2.10}$$

Since,

$$(\tilde{u}_j - u_j)\frac{\partial\rho}{\partial x_j} = \frac{\partial(\rho(\tilde{u}_j - u_j))}{\partial x_j} - \rho\frac{\partial(\tilde{u}_j - u_j)}{\partial x_j},\tag{2.11}$$

we write equation (2.10), as

$$\frac{\tilde{d}\rho}{dt} = -\rho\frac{\partial\tilde{u}_j}{\partial x_j} + \frac{\partial(\rho(\tilde{u}_j - u_j))}{\partial x_j}.\tag{2.12}$$

By combining the continuity equation (5.57) and momentum equation (2.2) one can obtain the conservative form of the momentum equation as,

$$\frac{\partial(\rho u_i)}{\partial t} + \frac{\partial}{\partial x_j}(\rho u_i u_j) = \rho g_i + \frac{\partial \sigma_{ij}}{\partial x_j}$$
$$= \text{RHS}_i, \tag{2.13}$$

where g_i is the body force acceleration, and σ_{ij} the stress tensor. We write the left hand side in terms of a transport derivative as,

$$\frac{\tilde{d}(\rho u_i)}{dt} + (u_j - \tilde{u}_j)\frac{\partial}{\partial x_j}(\rho u_i) + \rho u_i \frac{\partial u_j}{\partial x_j} = \text{RHS}_i. \tag{2.14}$$

Similar to eq. (2.11), we write,

$$(\tilde{u}_j - u_j)\frac{\partial}{\partial x_j}(\rho u_i) = \frac{\partial}{\partial x_j}(\rho u_i(\tilde{u}_j - u_j)) - \rho u_i \frac{\partial}{\partial x_j}(\tilde{u}_j - u_j). \tag{2.15}$$

Substituting, this in eq. (2.14), we have,

$$\frac{\tilde{d}(\rho u_i)}{dt} = \frac{\partial}{\partial x_j}(\rho u_i(\tilde{u}_j - u_j)) - \rho u_i \frac{\partial}{\partial x_j}(\tilde{u}_j) + \text{RHS}_i. \tag{2.16}$$

In Adami *et al.* (2013a), the second term is neglected but at this stage we do not neglect this term. We simplify this further and write,

$$\rho \frac{\tilde{d}u_i}{dt} + u_i \frac{\tilde{d}\rho}{dt} = \frac{\partial}{\partial x_j}(\rho u_i(\tilde{u}_j - u_j)) - \rho u_i \frac{\partial}{\partial x_j}(\tilde{u}_j) + \text{RHS}_i. \tag{2.17}$$

Using, eq. (4.16), we write

$$\begin{aligned}
\rho \frac{\tilde{d}u_i}{dt} &= \frac{\partial}{\partial x_j}(\rho u_i(\tilde{u}_j - u_j)) - u_i \frac{\partial}{\partial x_j}(\rho(\tilde{u}_j - u_j)) + \text{RHS}_i \\
&= \rho(\tilde{u}_j - u_j)\frac{\partial u_i}{\partial x_j} + \text{RHS}_i \\
&= \rho \frac{\partial}{\partial x_j}(u_i(\tilde{u}_j - u_j)) - \rho u_i \frac{\partial}{\partial x_j}(\tilde{u}_j - u_j) + \text{RHS}_i.
\end{aligned} \tag{2.18}$$

We therefore write the momentum equation as,

$$\frac{\tilde{d}u_i}{dt} = \frac{\partial}{\partial x_j}(u_i(\tilde{u}_j - u_j)) - u_i \frac{\partial}{\partial x_j}(\tilde{u}_j - u_j) + g_i + \frac{1}{\rho}\frac{\partial \sigma_{ij}}{\partial x_j}. \tag{2.19}$$

We note that this equation encompasses both fluid dynamics as well as elastic dynamics by simply changing the way σ_{ij} is modeled. The first term on the right-hand-side of eq. (2.19) is the additional artificial stress term that is included in the TVF (Adami *et al.*, 2013a). The second term involves the divergence of the transport velocity field. In the case of the TVF, the term includes a background pressure acceleration that is of the form,

$$\left(\frac{d\mathbf{u}_a}{dt}\right)_c = -p_a^0 \sum_{b \in N(a)} \frac{m_b}{\rho_b^2} \nabla W(\mathbf{r}_{ab}, \tilde{h}_{ab}), \tag{2.20}$$

where p_a^0 is the background pressure for the given particle a, $\mathbf{r}_{ab} = \mathbf{r}_a - \mathbf{r}_b$, $\tilde{h}_{ab} = (h_a + h_b)/2$, and index b refers to the neighbors of particle a. The divergence of this term results in the Laplacian of the kernel W. For most kernels used in SPH, this term is certainly not zero and therefore this should not be ignored. We investigate the importance of including these terms in section 5.4. We note that in the case of elastic dynamics that these terms are negligible and do not make a significant difference. This has also been pointed out by Zhang *et al.* (2017b).

The Jaumann stress rate is also similarly modified to account for the transport velocity as,

$$\frac{\tilde{d}\sigma'_{ij}}{dt} = 2G(\dot{\epsilon}_{ij} - \frac{1}{3}\dot{\epsilon}_{kk}\delta_{ij}) + \sigma'_{ik}\Omega_{jk} + \Omega_{ik}\sigma'_{kj} +$$
$$\frac{\partial}{\partial x_k}(\sigma'_{ij}(\tilde{u}_k - u_k)) - \sigma'_{ij}\frac{\partial}{\partial x_k}(\tilde{u}_k - u_k). \quad (2.21)$$

2.3.1   The EDAC-SPH method

We apply the EDAC-SPH (Ramachandran and Puri, 2019) in order to evolve the pressure accurately and reduce the amount of noise in the pressure field. In the original EDAC-SPH implementation, internal flows were evolved using the TVF whereas for cases with a free-surface the traditional WCSPH was employed. In this work we propose a unified approach by carefully incorporating free-surfaces. The original EDAC-SPH scheme also did not accurately incorporate the transport velocity which we include here. This allows us to use the same scheme for both internal and external flows.

The δ-SPH (Antuono *et al.*, 2010) implementation is in principle similar to the EDAC-SPH method but requires the use of the kernel gradient corrections which involve the solution of a small matrix (3×3 in 3D), for each particle. The EDAC-SPH method does not require this and is therefore simpler and in principle more efficient. In (Ramachandran and Puri, 2019), the EDAC pressure evolution equation was,

$$\frac{dp}{dt} = -\rho c_s^2 \text{div}(\mathbf{u}) + \nu_{edac}\nabla^2 p, \quad (2.22)$$

where ν_{edac} is a viscosity parameter for the smoothing of the pressure and c_s is the (artificial) speed of sound. We discuss this term later. However, in the context of the consistent evolution using the transport velocity, we note that the above should be evolved using,

$$\frac{\tilde{d}p}{dt} = (p - \rho c_s^2)\text{div}(\mathbf{u}) - p\,\text{div}(\tilde{\mathbf{u}}) + \text{div}(p(\tilde{\mathbf{u}} - \mathbf{u})) + \nu_{edac}\nabla^2 p. \quad (2.23)$$

The value of ν_{edac} is,

$$\nu_{edac} = \frac{\alpha_{edac}h c_s}{8}, \quad (2.24)$$

where h is the smoothing length of the kernel and a value of $\alpha_{\text{edac}} = 0.5$ is recommended as suggested in (Ramachandran and Puri, 2015).

This along with the momentum equation and evolution of volume or density may be employed. A state equation is often used even for elastic dynamics problems, we propose to use the EDAC approach for elastic equations as well as this reduces the amount of artificial viscosity that is needed.

2.3.2 SPH discretization

In the current work, both fluid and solid modelling uses the same continuity and pressure evolution equation. The SPH discretization of the continuity equation (4.16) and the pressure evolution equation (2.23) respectively are,

$$\frac{\tilde{d}\rho_a}{dt} = \sum_b \frac{m_b}{\rho_b} \left(\rho_a \, \tilde{\mathbf{u}}_{ab} \, + \, (\rho \, (\tilde{\mathbf{u}} \, - \, \mathbf{u}))_{ab}\right) \cdot \nabla_a W_{ab}, \tag{2.25}$$

$$\frac{\tilde{d}p_a}{dt} = \sum_b \frac{m_b}{\rho_b} \left((p_a - \rho_a c_s^2) \, \mathbf{u}_{ab} \, + \, p_a \, \tilde{\mathbf{u}}_{ab} \, - \, (p \, (\tilde{\mathbf{u}} - \mathbf{u}))_{ab} \, + \right.$$
$$\left. 4 \, \nu_{edac} \frac{p_a - p_b}{(\rho_a + \rho_b)(r_{ab}^2 + 0.01 h_{ab}^2)} \mathbf{r}_{ab}\right) \cdot \nabla_a W_{ab}. \tag{2.26}$$

Similarly, the discretized momentum equation for fluids is written as,

$$\frac{\tilde{d}\mathbf{u}_a}{dt} = - \sum_b m_b \left[\left(\frac{p_a}{\rho_a^2} + \frac{p_b}{\rho_b^2}\right)\mathbf{I} - \left(\frac{\mathbf{A}_a}{\rho_a^2} + \frac{\mathbf{A}_b}{\rho_b^2}\right)\right] \cdot \nabla_a W_{ab}$$
$$+ \mathbf{u}_a \sum_b \frac{m_b}{\rho_b} \, \tilde{\mathbf{u}}_{ab} \cdot \nabla_a W_{ab} + \sum_b m_b \frac{4\eta \nabla W_{ab} \cdot \mathbf{r}_{ab}}{(\rho_a + \rho_b)(r_{ab}^2 + 0.01 h_{ab}^2)} \mathbf{u}_{ab} + \mathbf{g}_a, \tag{2.27}$$

where $\mathbf{A}_a = \rho_a \mathbf{u}_a \otimes (\tilde{\mathbf{u}}_a - \mathbf{u}_a)$, $\mathbf{I}$ is the identity matrix, η is the kinematic viscosity of the fluid and Morris *et al.* (1997a) formulation is used to discretize the viscosity term.

We add to the momentum equation an additional artificial viscosity term Π_{ab} (Monaghan, 2005a) to maintain the stability of the numerical scheme, given as,

$$\Pi_{ab} = \begin{cases} \frac{-\alpha h_{ab} \bar{c}_{ab} \phi_{ab}}{\bar{\rho}_{ab}} & \mathbf{u}_{ab} \cdot \mathbf{r}_{ab} < 0, \\ 0 & \mathbf{u}_{ab} \cdot \mathbf{r}_{ab} \geq 0, \end{cases} \tag{2.28}$$

where,

$$\phi_{ab} = \frac{\mathbf{u}_{ab} \cdot \mathbf{r}_{ab}}{r_{ab}^2 + 0.01 h_{ab}^2}, \tag{2.29}$$

where $\mathbf{r}_{ab} = \mathbf{r}_a - \mathbf{r}_b$, $\mathbf{u}_{ab} = \mathbf{u}_a - \mathbf{u}_b$, $h_{ab} = (h_a + h_b)/2$, $\bar{\rho}_{ab} = (\rho_a + \rho_b)/2$, $\bar{c}_{ab} = (c_a + c_b)/2$, and α is the artificial viscosity parameter.

For solid mechanics the momentum equation is written as,

$$\frac{\tilde{d}\mathbf{u}_a}{dt} = -\sum_b m_b\left[\left(\frac{p_a}{\rho_a^2} + \frac{p_b}{\rho_b^2}\right)\mathbf{I} - \left(\frac{\sigma_a'}{\rho_a^2} + \frac{\sigma_b'}{\rho_b^2} + \Pi_{ab}\mathbf{I}\right)\right] \cdot \nabla_a W_{ab} + \mathbf{g}_a, \qquad (2.30)$$

we have not considered the correction stress term $\mathbf{A}$ in momentum equation of solid mechanics as it has a negligible effect.

In addition to these three equations, the Jaumann stress rate equation is also solved. In the current work we use the momentum velocity $\mathbf{u}$ rather than $\tilde{\mathbf{u}}$ as in the GTVF (Zhang *et al.*, 2017b) in the computation of gradient of velocity. The SPH discretization of the gradient of velocity is given as,

$$\nabla\mathbf{u}_a = -\sum_b \frac{m_b}{\rho_b}(\mathbf{u}_a - \mathbf{u}_b) \otimes (\nabla_a W_{ab}), \qquad (2.31)$$

where $\otimes$ is the outer product.

The SPH discretization of the modified Jaumann stress rate eq. (2.21) is given as,

$$\frac{\tilde{d}\sigma_a'}{dt} = 2G(\dot{\epsilon}_a - \frac{1}{3}\dot{\epsilon}_a\mathbf{I}) + \sigma_a'\Omega_a^T + \Omega_a\sigma_a' +$$
$$+ \sum_b \frac{m_b}{\rho_b} (\sigma' \otimes (\tilde{\mathbf{u}} - \mathbf{u}))_{ab} \cdot \nabla_a W_{ab} + \sigma_a' \sum_b \frac{m_b}{\rho_b} (\tilde{\mathbf{u}} - \mathbf{u})_{ab} \cdot \nabla_a W_{ab}. \quad (2.32)$$

2.3.3 Particle transport

The particles in the current scheme are moved with the transport velocity,

$$\frac{d\mathbf{r}_a}{dt} = \tilde{\mathbf{u}}_a. \qquad (2.33)$$

The transport velocity is updated using,

$$\tilde{\mathbf{u}}_a(t + \Delta t) = \mathbf{u}_a(t) + \Delta t \frac{\tilde{d}\mathbf{u}_a}{dt} + \left(\frac{d\mathbf{u}_a}{dt}\right)_c \Delta t, \qquad (2.34)$$

where $\left(\frac{d\mathbf{u}_a}{dt}\right)_c$ is the homogenization acceleration which ensures that the particle positions are homogeneous. In the current work we have explored two kinds of homogenization accelerations, one is a displacement based technique due to Sun *et al.* (2017), which here after we refer as SPST and the other is the iterative particle shifting technique due to Huang *et al.* (2019) referred as IPST. These are discussed in the following.

Sun 2019 PST

In Sun *et al.* (2017), the particle shifting technique was implemented as a particle displacement ($\delta\mathbf{r}$). This was modified in Sun *et al.* (2019a) to be computed as a change to

the velocity. In the present work we modify this to be treated as an acceleration to the particle in order to unify the treatment of different PST methods.

Firstly, the velocity deviation based equation is given as,

$$\delta \mathbf{u}_a = -\text{Ma} \, (2h) c_0 \sum_b \left[1 + R \left(\frac{W_{ab}}{W(\Delta x)} \right)^n \right] \nabla_a W_{ab} V_b, \qquad (2.35)$$

it is modified to force based as,

$$\left(\frac{d\mathbf{u}_a}{dt} \right)_c = -\frac{\text{Ma} \, (2h) c_0}{\Delta t} \sum_b \left[1 + R \left(\frac{W_{ab}}{W(\Delta x)} \right)^n \right] \nabla_a W_{ab} V_b, \qquad (2.36)$$

where R is an adjustment factor to handle the tensile instability, and Ma is the mach number of the flow. V_b is the volume of the bth particle. The acceleration is changed to account for particles that are on the free surface. We use $R = 0.2$ and $n = 4$ as suggested by Sun *et al.* (2019a).

IPST

The Iterative PST of Huang (Huang *et al.*, 2019) builds on the work of Xu *et al.* (2009b). The method iteratively moves the particles every timestep in order to achieve a uniform particle distribution determined by a convergence criterion. The properties of the particles are corrected using a Taylor series expansion.

In the original IPST, the shifting vector is computed as,

$$\delta r_a^m = U_{\max} \, \Delta t \, \sum_b (V_b \, \mathbf{n}_{ab} \, W_{ab})^m, \qquad (2.37)$$

where m is the number of iterations, $m = (1, 2, 3, \dots)$, $\mathbf{n}_{ab}$ is the unit vector between particle a and b. The particles are then moved using this displacement using,

$$\mathbf{r}_a^{m+1} = \mathbf{r}_a^m + \delta \mathbf{r}_a^m. \qquad (2.38)$$

This is repeated until the convergence criterion is achieved. The convergence criterion is defined as

$$|\max(\chi_a^m) - \overline{\chi_a^m}| \le \epsilon, \qquad (2.39)$$

where

$$\chi_a^m = h^2 \sum W_{ab}^m, \qquad (2.40)$$

and $\overline{\chi_a^m}$ is the value of χ_a^m computed with the initial configuration of the particles. For problems where there is no free surface this value is a constant computed using the initial configuration. For free-surface problems it is computed as the maximum value of χ_a^m at the initial configuration, which corresponds to the a free surface particle.

The initial and final positions of the particles are used to determine an acceleration on the particle that would produce such a displacement. This is computed as

$$\left(\frac{d\mathbf{u}_a}{dt}\right)_{\text{c}} = 2\,\frac{\mathbf{r}_a^M - \mathbf{r}_a^0}{\Delta t^2},$$

(2.41)

where $\mathbf{r}_a^M$ is the final position of the particle, a.

2.3.4   Free surface identification algorithm

Free surfaces must be handled with care especially in the context of the PST algorithm. The original TVF (Adami *et al.*, 2013a) is not designed to handle free-surface problems. Lind *et al.* (2012) was the first to handle free-surfaces carefully in the context of the PST. Lind *et al.* (2012); Oger *et al.* (2016), and Sun *et al.* (2019a) identify the particles that are on the free-surface or near it and adjust the particle shifting algorithm so the free surface particles remain intact. Zhang *et al.* (2017b) on the other hand relies on the pressure being zero at the free surface and scales the homogenization force with the pressure.

Both (Oger *et al.*, 2016) and (Sun *et al.*, 2019a) identify the free-surface particles by computing the eigenvalues of the correction matrix employed for the SPH scheme. This is based on the work of (Marrone *et al.*, 2010). This method is computationally expensive and in this work we use a much simpler approach that was introduced in (Muta *et al.*, 2020) to find the free-surface particles as well as their normals. We first compute the normals of all the particles in the medium whose free surface need to be identified. The normals are computed as,

$$\mathbf{n}_a^* = \sum_b -\frac{m_b}{\rho_b}\nabla_a W_{ab}$$

(2.42)

If the magnitude of the resulting vector is less than $\frac{1}{4h_a}$, then the $\mathbf{n}^*$ is set to zero otherwise we normalize the vector by its magnitude. Then, we smooth these normals using an SPH approximation,

$$\hat{\mathbf{n}}_a = \sum_b \frac{m_b}{\rho_b}\mathbf{n}_b^* W_{ab}.$$

(2.43)

Finally, we normalize $\hat{\mathbf{n}}_a$ so they are unit vectors. We note that for particles that are isolated and have no neighbors the above algorithm will not work. We identify all such particles by computing the summation density of all particles and any particles with a summation density that is lower than half the fluid density are marked as free-surface particles. For the quintic spline kernel used in this work we find that the cutoff value of half the fluid density is effective in differentiating particles that are away from the bulk fluid.

figures/ctvf/figures/free_surface... figures/ctvf/figures/free_surface...

(a)   (b)
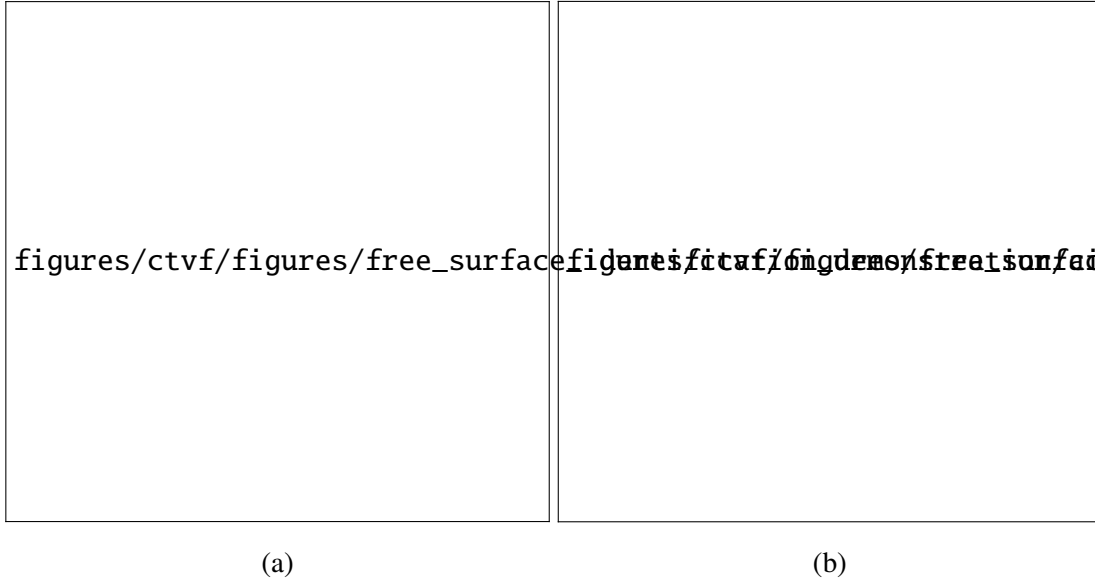
Figure 2.1: Identification of free surface particles of a circular ring of fluid. Depicts (a) normals of the fluid particles, (b) boundary particles of the fluid particles

The current algorithm is tested with to two simple cases. We first consider a circular ring of fluid. As can be seen from fig. 2.1a, three layers of particles which are near the free surface have a normal. From these normals we need to find the surface particles. We loop over all the particles in the medium, and any particles which have a non-zero normal are considered for further analysis. For each of these potential surface particles we find the angle between the particle and each of its neighbors. For a 2d case, if the angle between the normal of the particle and that of the line joining the particle to its neighbor is less than 60 degrees then this particle is *not* considered as a free-surface particle. If no such neighbor exists, then the particle is considered to be a free-surface particle. As can be seen in fig. 2.1b, the free surface particles are correctly identified. As a second test case we consider a patch of fluid resting on a wall. As a first step we compute the normals of the particles, see fig. 2.2a and then loop over all the particles and by considering only the particles which have non-zero normals, we determine the boundary particles, as in fig. 2.2b. Finally this is applied to the case of a dam break. As can be seen from fig. 2.3 and fig. 2.4, the free surface particles are identified correctly.

2.3.5   PST close to the free surface

Near the free-surface the PST has to be performed with some care for both fluids and solids. This is because of the lack of support for the particles near the free-surface. After the free surface particles are identified by using the algorithm described in section 2.3.4, we mark the particles which are in close proximity to the free surface particles. This is

figures/ctvf/figures/free_surface_identification_demonstration/...

(a)

figures/ctvf/figures/free_surface_identification_demonstration/...

(b)
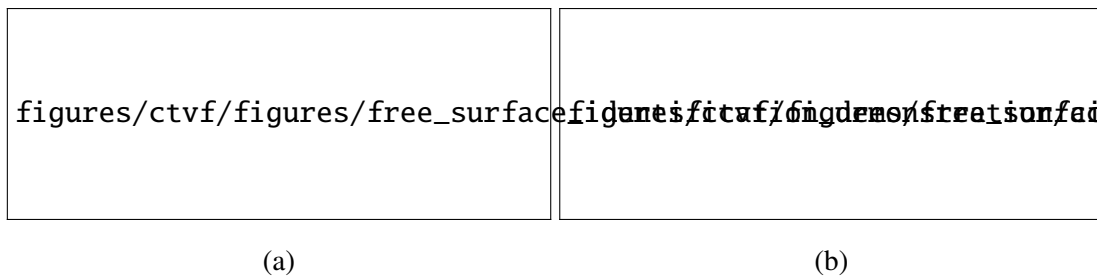
Figure 2.2: Identification of free surface particles of a fluid resting on a wall. Depicts (a) normals of the fluid particles, (b) boundary particles of the fluid particles

figures/ctvf/figures/free_surface_identification_demonstration/normals_dam_brea...

Figure 2.3: Identification of normals of fluid in a dam break simulation. Shows us the normals of all the fluid particles

figures/ctvf/figures/free_surface_identification_demonstration/boundary_particles_f

Figure 2.4: Identification of boundary particles of fluid at an instance in a dam break. Shows boundary particles of all the fluid particles

(b)

(a)
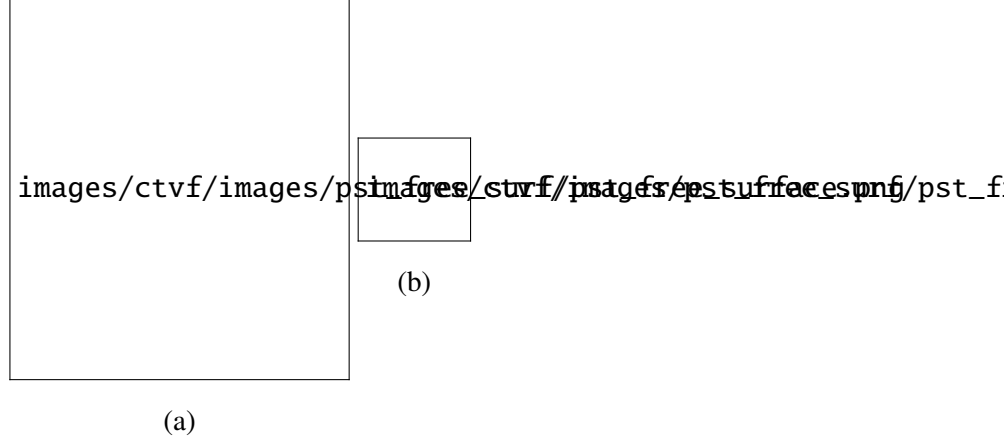
Figure 2.5: Set h_b of the particles. (a) Particles with a free surface whose free particles are identified (b) Minimum distance between the particle in the vicinity of the free surface to the free surface particle.

done through a variable associated with each particle called h_b, which is initialized to the initial smoothing length of the particles.

We loop over all the particles that are not on the boundary, and their h_b is adjusted to the distance to the closest boundary particle divided appropriately by a kernel-dependent factor such that the kernel support is up to the closest boundary particle. In the current work, we have used a quintic spline kernel for which the factor is 3. The algorithm is shown in section 2.3.5 and depicted in fig. 2.5. We note that this h_b is only used for the PST force/displacement computation. This process allows us to ensure that the homogenization force does not push these particles towards the free-surface.

[!ht] [1] particle i in all particles i is a boundary particle set $h_{b,i} = 0$ set $h_{b,i} = h$ particle i in all non-boundary particles particle i has a boundary particle in its neighborhood $x_{\text{dist},i} \leftarrow$ Distance to nearest boundary particle Set $h_{b,i} = \frac{x_{\text{dist, i}}}{3}$

In the PST of Sun *et al.* (2019a), the shifting acceleration is adjusted using

$$\left(\frac{d\mathbf{u}_a}{dt}\right)_{\text{c}} = \begin{cases} 0 & \text{if boundary,} \\ (\frac{d\mathbf{u}_a}{dt})_{\text{c}} - ((\frac{d\mathbf{u}_a}{dt})_{\text{c}} \cdot \mathbf{n}_a)\mathbf{n}_a & \text{if } h_b < h, \\ (\frac{d\mathbf{u}_a}{dt})_{\text{c}} & \text{if } h_b = h. \end{cases} \quad (2.44)$$

Whereas while using IPST (Huang *et al.*, 2019), rather than adjusting the final shifting acceleration, we adjust the increment in the position of eq. (3.11),

$$\delta\mathbf{r}_a^m = \begin{cases} 0 & \text{if boundary,} \\ \delta\mathbf{r}_a^m - (\delta\mathbf{r}_a^m \cdot \mathbf{n}_a)\mathbf{n}_a & \text{if } h_b < h, \\ \delta\mathbf{r}_a^m & \text{if } h_b = h. \end{cases} \quad (2.45)$$

2.3.6   Boundary conditions

The ghost particle approach of Adami *et al.* (2012) is used to model the boundaries. We use three layers of ghost particles to model the solid wall. The properties of the solid wall are interpolated from the fluid particles.

When computing the divergence of the velocity field on fluid particles, we enforce a no-penetration boundary condition and not a no-slip boundary condition. The velocity of the fluid is projected onto the ghost particles using,

$$\hat{\mathbf{u}}_a = \frac{\sum_b \mathbf{u}_b W_{ab}}{\sum_b W_{ab}}, \tag{2.46}$$

$$\check{\mathbf{u}}_a = \frac{\sum_b \tilde{\mathbf{u}}_b W_{ab}}{\sum_b W_{ab}}, \tag{2.47}$$

where $\mathbf{u}_b$, $\tilde{\mathbf{u}}_b$ are the momentum and transport velocity of the fluid respectively and W_{ab} is the kernel value between the fluid particle and the ghost particle.

The normal component of this projected velocity is then reflected and set as the ghost particle velocity,

$$\mathbf{u}_{\mathrm{Ga}} = 2\hat{\mathbf{n}}((\mathbf{u}_{\mathrm{p}} - \hat{\mathbf{u}}_{\mathrm{a}}) \cdot \hat{\mathbf{n}}) + \hat{\mathbf{u}}_{\mathrm{a}}, \tag{2.48}$$

where $\mathbf{u}_{\mathrm{p}}$ is the local velocity of the boundary and $\hat{\mathbf{n}}$ is the unit normal to the boundary particle a. Similarly the transport velocity of the ghost particle is set as,

$$\tilde{\mathbf{u}}_{\mathrm{Gi}} = 2\hat{\mathbf{n}}((\mathbf{u}_{\mathrm{p}} - \check{\mathbf{u}}_{\mathrm{i}}) \cdot \hat{\mathbf{n}}) + \check{\mathbf{u}}_{\mathrm{i}}, \tag{2.49}$$

When the viscous force is computed, the no slip boundary condition is used, where the velocity on the boundary set as,

$$\mathbf{u}_{\mathrm{Ga}} = 2\mathbf{u}_{\mathrm{p}} - \hat{\mathbf{u}}_{\mathrm{a}}, \tag{2.50}$$

a similar form is used for the transport velocity here too,

$$\tilde{\mathbf{u}}_{\mathrm{Ga}} = 2\mathbf{u}_{\mathrm{p}} - \check{\mathbf{u}}_{\mathrm{a}}. \tag{2.51}$$

The pressure of the boundary particle is extrapolated from its surrounding fluid particles by the following equation,

$$p_w = \frac{\Sigma_f p_f W_{wf} + (\mathbf{g} - \mathbf{a_w}) \cdot \Sigma_f \rho_f \mathbf{r}_{wf} W_{wf}}{\Sigma_f W_{wf}}, \tag{2.52}$$

where $\mathbf{a}_w$ is the acceleration of the wall. The subscript f denotes the fluid particles and w denotes the wall particles.

For solid mechanics problems, in addition to the extrapolation of pressure, we also extrapolate the deviatoric shear stress on to the boundary particles using,

$$\sigma'_{ij} = \frac{\Sigma_s \sigma'_{ij} W_{ws}}{\Sigma_s W_{ws}}, \tag{2.53}$$

where s denotes the solid particles.

2.3.7   Time integration

We use the kick-drift-kick scheme for the time integration. We first move the velocities of the particles to half time step,

$$\mathbf{u}_a^{n+\frac{1}{2}} = \mathbf{u}_a^n + \frac{\Delta t}{2}\left(\frac{\tilde{d}\mathbf{u}_a}{dt}\right)^n, \tag{2.54}$$

$$\tilde{\mathbf{u}}_a^{n+\frac{1}{2}} = \mathbf{u}_a^{n+\frac{1}{2}} + \frac{\Delta t}{2}\left(\frac{d\mathbf{u}_a}{dt}\right)^n_c. \tag{2.55}$$

Then the time derivatives of density and deviatoric stresses are calculated using the eq. (5.27) and eq. (3.7). The new time step density, deviatoric stresses and particle position are updated by,

$$\rho_a^{n+1} = \rho_a^n + \Delta t\left(\frac{\tilde{d}\rho_a}{dt}\right)^{n+\frac{1}{2}}, \tag{2.56}$$

$$p_a^{n+1} = p_a^n + \Delta t\left(\frac{\tilde{d}p_a}{dt}\right)^{n+\frac{1}{2}}, \tag{2.57}$$

$$\sigma_a'^{\,n+1} = \sigma_a'^{\,n} + \Delta t\left(\frac{\tilde{d}\sigma_a'}{dt}\right)^{n+\frac{1}{2}}, \tag{2.58}$$

$$\mathbf{r}_a^{n+1} = \mathbf{r}_a^n + \Delta t\,\tilde{\mathbf{u}}_a^{n+1}. \tag{2.59}$$

Finally, at new time-step particle position, the momentum velocity is updated

$$\mathbf{u}_a^{n+1} = \mathbf{u}_a^{n+\frac{1}{2}} + \frac{\Delta t}{2}\left(\frac{\tilde{d}\mathbf{u}_a}{dt}\right)^{n+1}. \tag{2.60}$$

For the numerical stability, the time step depends on the CFL condition as,

$$\Delta t = \min\left(0.25\,\frac{h}{c+|U|}, 0.25\,\frac{h^2}{\nu}, 0.25\,\frac{h^2}{g}\right), \tag{2.61}$$

where $|U|$ is the maximum velocity magnitude, c is the speed of sound typically chosen as $10|U|$ for fluids in this work.

For solid mechanics, the timestep is set based on the following,

$$\Delta t \leq 0.25\left(\frac{h}{c_0 + |U|}\right), \tag{2.62}$$

where c_0 is the speed of sound of the solid body.

2.4   Results

We validate the proposed scheme using a suite of benchmark problems for both fluid and solid mechanics. We first consider fluids where we look at the Taylor-Green vortex problem, the lid-driven cavity, and the two-dimensional dam-break problem. We then consider problems in elastic dynamics like the oscillating plate, a uniaxial compression problem, the collision of rubber rings, and a high-velocity impact problem.

We show how the proposed method is an improvement on previous work. Every result shown is produced using an automation framework (Ramachandran, 2018a). The source code is available at `https://gitlab.com/pypr/ctvf`.

2.4.1   Taylor-Green vortex

In the first benchmark, we test the accuracy of the correction terms and evaluate the different particle shifting schemes introduced in the proposed scheme by simulating a Taylor-Green vortex. It consists of a periodic unit box with no solid boundaries. Taylor-Green vortex problem has an exact solution given as,

$$u = -Ue^{bt}\cos(2\pi x)\sin(2\pi y) \tag{2.63}$$

$$v = Ue^{bt}\sin(2\pi x)\cos(2\pi y) \tag{2.64}$$

$$p = -U^2 e^{2bt}(\cos(4\pi x) + \cos(4\pi y))/4, \tag{2.65}$$

where U is chosen as $1\,\mathrm{m\,s^{-1}}$, $b = -8\pi^2/Re$, $Re = UL/v$, and $L = 1$ m. We initialize the fluid using this at $t = 0$ and compare the results with the exact solution. The Reynolds number, Re, is initially chosen to be 100. The quintic spline with $h/\Delta x = 1.0$ is used. We use summation density to compute the density and evolve pressure with eq. (5.31). No artificial viscosity is used for this problem. The decay rate of the velocity is studied using the evolution of maximum velocity $|\mathbf{u}_{max}|$ in time. We compute the L_1 error in the velocity magnitude as,

$$L_1 = \frac{\sum_i |\mathbf{u}_{i,computed}| - |\mathbf{u}_{i,exact}|}{\sum_i |\mathbf{u}_{i,exact}|}, \tag{2.66}$$

where $\mathbf{u}_{i,exact}$ is found at the position of the i'th particle.

In fig. 2.6a we compare the decay of $|\mathbf{u}_{max}|$ with that of the exact solution for the case where we use SPST for particle shifting. As can be seen, the results are in excellent agreement with the expected decay. The same is seen in fig. 2.7a for the case using IPST. This shows the accuracy and robustness of the scheme with respect to changing the PST method. Figure 2.6b and fig. 2.7b show the L_1 error of velocity magnitude for various resolutions simulated using the two PST techniques. Figure 2.10 depicts the L_1 error of velocity magnitude for a Reynolds number of 100 and 1000 using SPST with and without

figures/ctvf/figures/taylor_green/tg_decay.pdf   figures/ctvf/figures/taylor_green/tg_l1.pdf

(a)   (b)
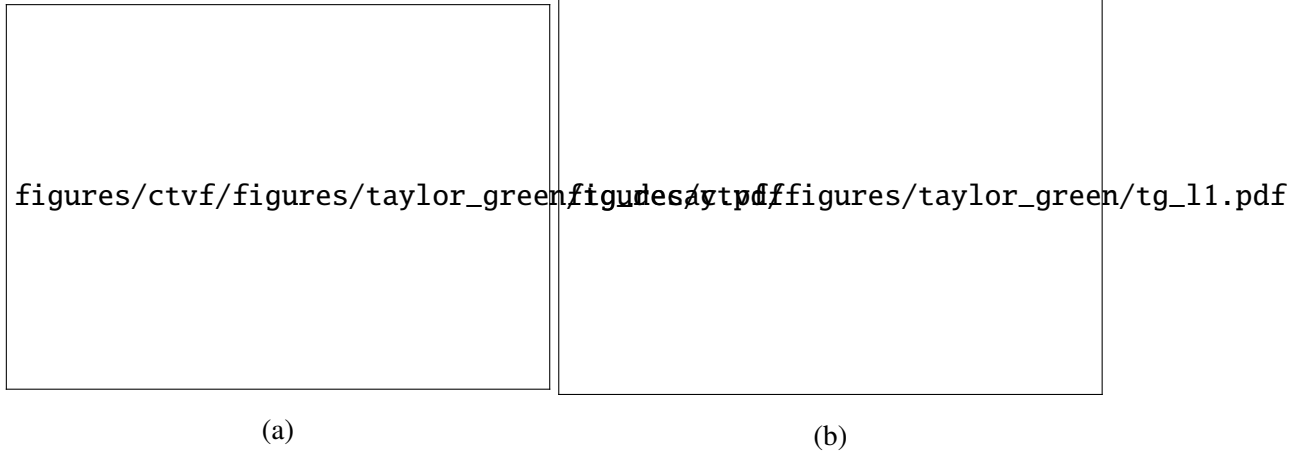
Figure 2.6: Taylor-Green vortices for an initial particle distribution of 50×50, 100×100 and 150×150 is simulated with a Reynolds number of 100 using SPST. Plots shown are (a) decay in maximum velocity (b) L_1 error in velocity magnitude.

correction terms. Figure 2.11 shows the same but using the IPST. The improvement due to the correction terms is clearly seen as a significant reduction in the error.

One can see that the IPST has lower errors at initial times. However, we do note that there appears to be a lack of convergence in the result as the resolution is increased. As the number of particles is increased the L_1 error does not correspondingly reduce. This is due to the low Reynolds number and the discretization of the viscous term that is being used. We show the results of the velocity decay and the L_1 error when a Reynolds number of 1000 is used in fig. 2.8 for IPST and in fig. 2.9 with SPST. In this case the convergence is clearly seen as the resolution is increased. Figure 2.12 shows distribution of particles with the color representing pressure. The Reynolds number of 1000 with a resolution of 150×150. We can see that the pressure distribution is smooth.

An inspection of figures 2.6b, 2.7b and 2.8b, 2.9b suggests that the IPST appears to be better than that of SPST.

2.4.2 Lid driven cavity

We evaluate the ability of the proposed scheme to handle solid wall boundary conditions by simulating a lid-driven cavity. The lid-driven cavity is a classic problem that can be challenging to simulate in the context of the SPH. It has been simulated by (Adami *et al.*, 2013a), (Huang *et al.*, 2019), (Ramachandran and Puri, 2019) to note a few. A rectangular cavity with length 1 m which is filled with fluid is constrained by four walls. Top wall has a velocity of $U = 1 \text{ m s}^{-1}$. A unit density is assumed for the fluid. The speed of sound of the fluid particle is set to $c = 10U_{max}$. We use the summation density to

figures/ctvf/figures/taylor_green figures/ctvf/figures/taylor_green/tg_l1_ipst.pdf

(a)
(b)

Figure 2.7: Taylor-Green vortices for an initial particle distribution of 50×50, 100×100 and 150×150 is simulated with a Reynolds number of 100 using IPST. Plots shown are (a) decay in maximum velocity (b) L_1 error in velocity magnitude.

figures/ctvf/figures/taylor_green_re_1000/tg_decay figures/ctvf/figures/taylor_green_re_1000/tg_l1_i

(a)
(b)

Figure 2.8: Taylor-Green vortices for an initial particle distribution of 50×50, 100×100 and 150×150 is simulated with a Reynolds number of 1000 using IPST. Plots shown are (a) decay in maximum velocity (b) L_1 error in velocity magnitude.

figures/ctvf/figures/taylor_green_re_1000/tg_decay.pdf figures/ctvf/figures/taylor_green_re_1000/tg_

(a)

(b)
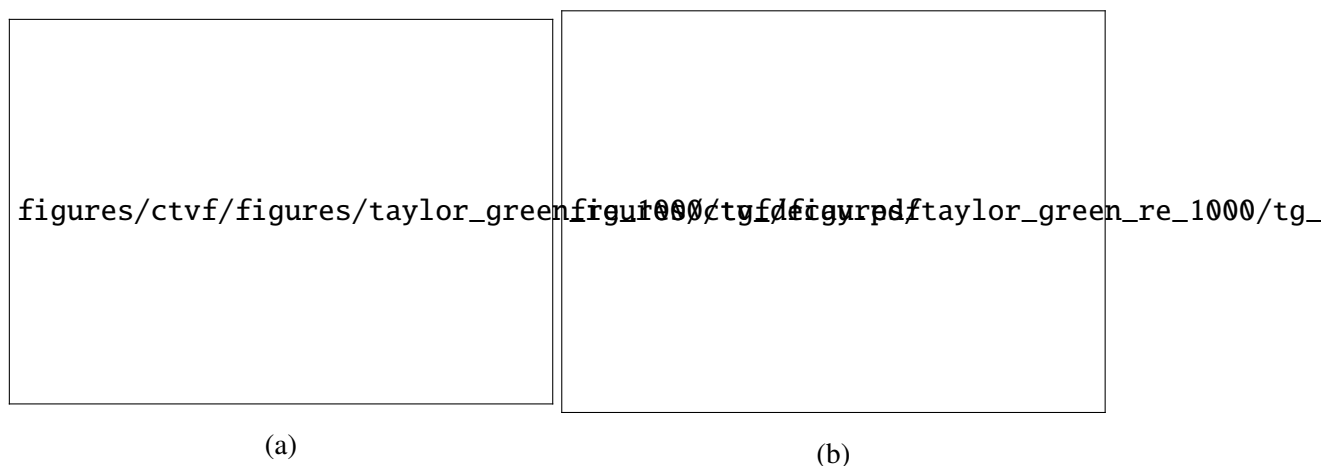
Figure 2.9: Taylor-Green vortices for an initial particle distribution of 50×50, 100×100 and 150×150 is simulated with a Reynolds number of 1000 using SPST. Plots shown are (a) decay in maximum velocity (b) L_1 error in velocity magnitude.

figures/ctvf/figures/taylor_green_re_100/tg_l1.pdf figures/ctvf/figures/taylor_green_re_1000/tg_l1_cor

(a)

(b)
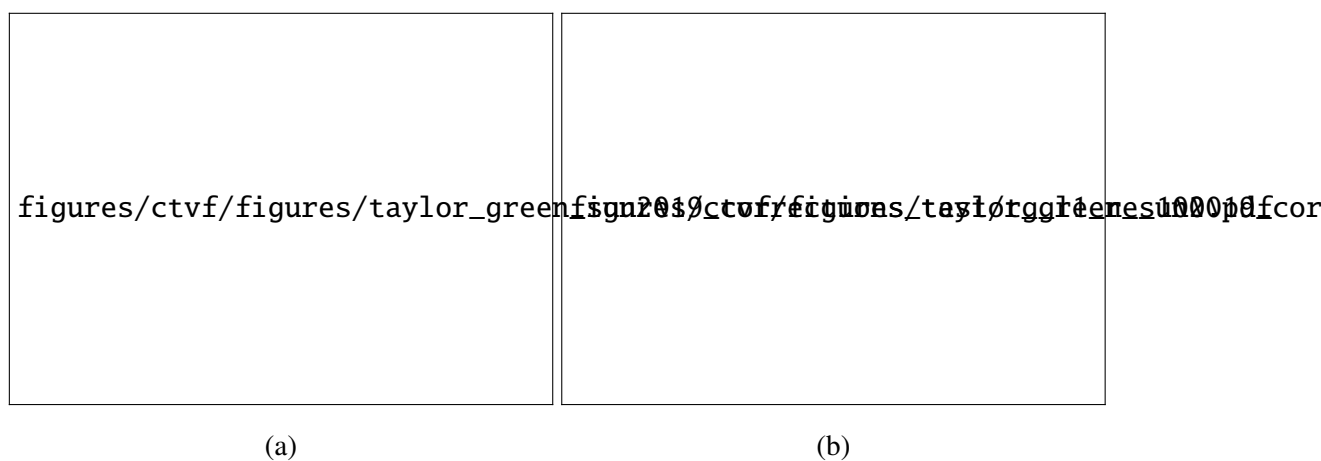
Figure 2.10: L_1 error for nx with 150×150 with and without corrections with SPST with a Reynolds number of a) 100 and b) 1000

(a)   (b)
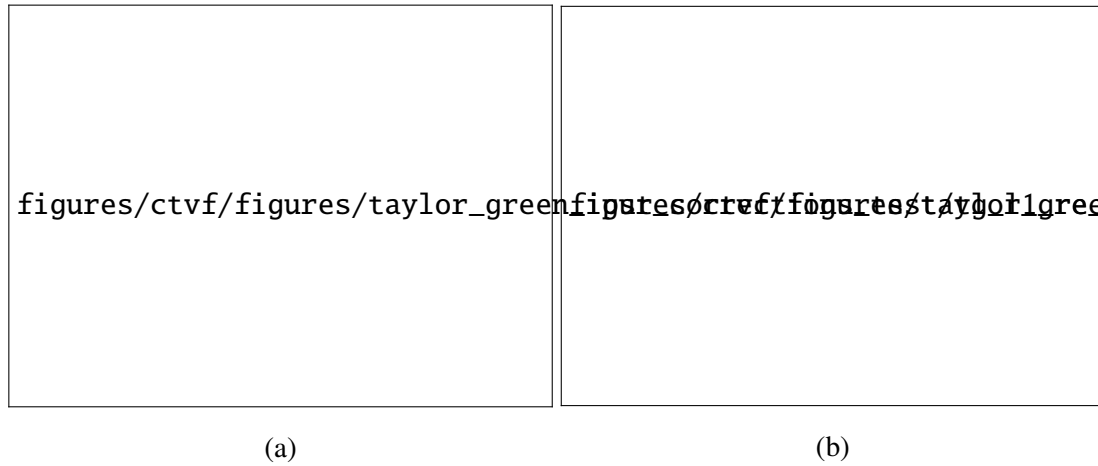
Figure 2.11: L_1 error for nx with 150×150 with and without corrections with IPST with a Reynolds number of a) 100 and b) 1000
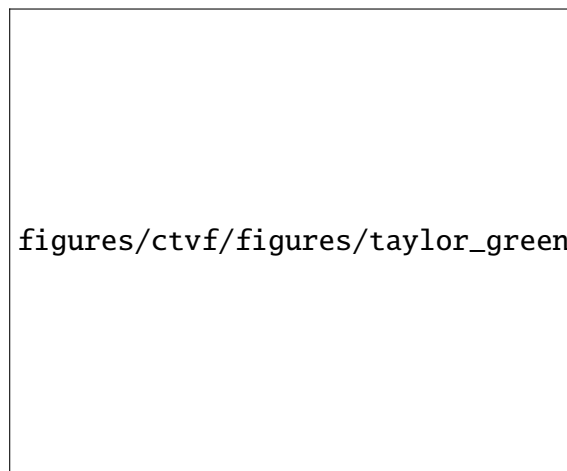
Figure 2.12: Particle plot of Taylor green vortices for a Reynolds number of 1000 with a resolution of 150×150. The colors represent the pressure.

figures/ctvf/figures/cavity_sun2019_corrections_test/good_vs_bad.pdf

Figure 2.13: Particle plot of cavity with a *Re* = 100 with particle arrangement of 150×150, left side with corrections and right side without correction terms.

compute the density. The viscosity of the fluid is set through the Reynolds number of the flow, $v = \frac{Re}{U}$. No artificial viscosity is used in the current problem.

We first simulate the cavity problem with a Reynolds number of 100 with and without corrections. In fig. 2.13 we can see that an unphysical void is produced when no corrections are employed. This is eliminated with the current scheme.

We now study convergence of the method as we vary the resolution. Figure 2.14 and fig. 2.15 show the center-line velocities *u* versus *y* and *v* versus *x* for the Reynolds numbers 100 and 1000 respectively. For the *Re* = 100 case we use three different resolutions of $50 \times 50, 100 \times 100$ and 150×150. For the *Re* = 1000 case, we use an initial 50×50, 100×100, and 200×200 grid of particles. These are compared against the results of (Ghia *et al.*, 1982). As we can see that the current scheme is able to predict the velocity profiles well.

2.4.3   2D Dam-break

We apply the proposed scheme to free surface flows by simulating a dam-break. This problem has been extensively studied before for example in (Muta *et al.*, 2020), (Zhang *et al.*, 2017b), and (Ramachandran and Puri, 2019).

A block of fluid having width 1m and a height of 2 m is allowed to settle under the influence of gravity inside a tank of length 4 m. The fluid block is initially placed to the left of the tank. The acceleration due to gravity is $g = 9.81$ m s^{-2}. To simulate the free surface flows we use the continuity equation to evolve the density using (5.27) and the (5.31) to evolve the pressure. We use free slip boundary conditions to compute

figures/ctvf/figures/cavity/uv_re100.pdf
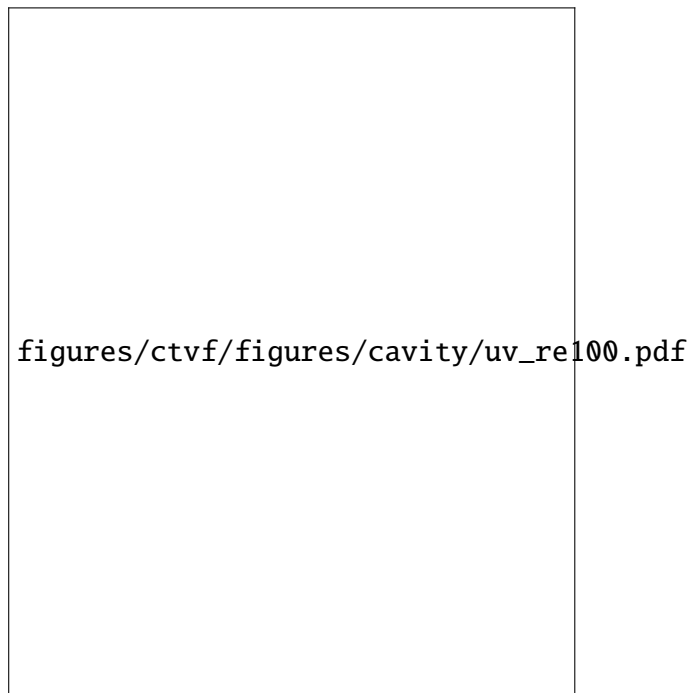
Figure 2.14: Velocity profiles u vs. y and v vs. x for the lid-driven-cavity problem at $Re = 100$ with three initial particle arrangement of 50×50, 100×100, and 150×150.

figures/ctvf/figures/cavity/uv_re1000.pdf
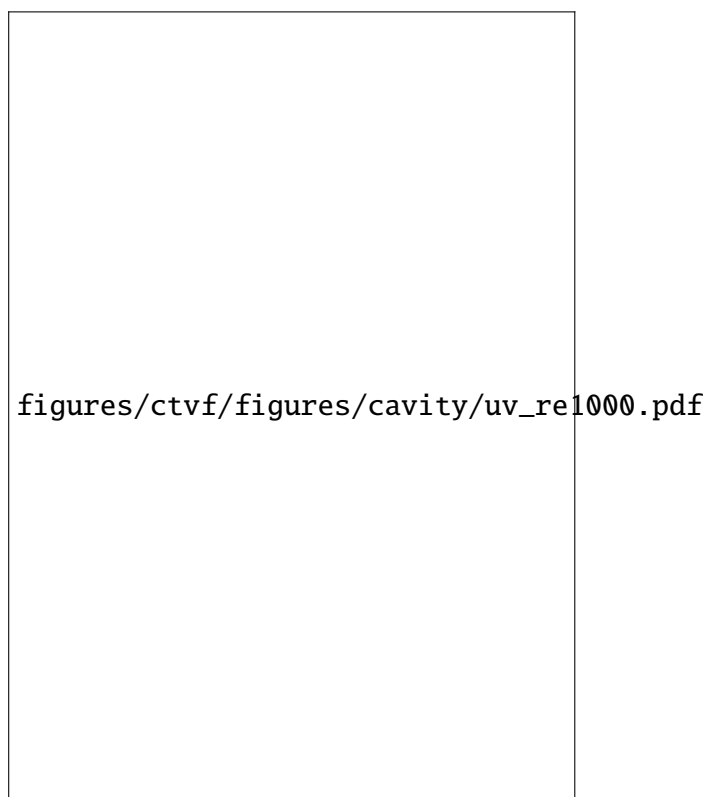
Figure 2.15: Velocity profiles for the lid-driven-cavity using the steady state simulation procedure for $Re = 1000$ with initial partial arrangement of 50×50, 100×100, and 200×200 compared with the results of (Ghia *et al.*, 1982).

figures/ctvf/figures/dam_break_2d/etvf_sun2019/x_vs_t.png

Figure 2.16: Position of the toe of the water versus time of CTVF as compared with the simulation of (Koshizuka and Oka, 1996). Z is the distance of toe of the dam from the left wall and L is the initial width of the dam

the divergence of the velocities and a no-slip boundary condition while computing the viscous forces. The value of $\alpha = 0.05$ is used for the artificial viscosity eq. (5.29) term.

Figure 2.16 compares the position of the toe of the fluid block with time against (Koshizuka and Oka, 1996), where the authors use the moving particle semi-implicit scheme to simulate the same.

The evolution of the fluid at three different time instants t= 0.6, 1.1, 2.0 seconds, is shown in fig. 2.17. As can be seen from fig. 2.17, at time 2.0 seconds we have captured the void created due to the splashing of the fluid. The colors in fig. 2.17 shows the velocity magnitude.

2.4.4   Oscillating plate

In this section, we test the improvement due to the correction terms while simulating elastic solids. We show the elimination of tensile instability while extending the transport velocity formulation (Adami *et al.*, 2013a) scheme to more particle shifting techniques. We consider a thin oscillating plate that is clamped on one side. Landau *et al.* (1960) provide an analytical solution for this problem. This is also simulated numerically in (Gray *et al.*, 2001b) and (Zhang *et al.*, 2017b).

figures/ctvf/figures/dam_break_2d/db2d_vmag.pdf

Figure 2.17: Particle plots of fluid in dam break at time $t = 0.6, 1.1, 2.0$ second, showing velocity magnitude as contour.

An oscillating plate with a length of 0.2 m and a height of 0.02 m is initially given with a velocity profile of,

$$v_y(x) = V_f \, c_0 \frac{F(x)}{F(L)},$$

where V_f varies for different cases. L is the length of the plate. $F(x)$ is given by,

$$F(x) = (\cos(kL) + \cosh(kL))\,(\cosh(kx) - \cos(kx)) +$$

$$(\sin(kL) - \sinh(kL))\,(\sinh(kx) - \sin(kx)). \quad (2.67)$$

In the present example kL is 1.875. The material properties of the plate are as follows, Young's modulus $E = 2.0 \times 10^6$ Pa, a Poisson's ratio of $v = 0.3975$. c_0 is speed of sound, and a density of $\rho = 1000 \, \text{kg m}^{-3}$, as done in (Gray *et al.*, 2001b). In all the cases simulated here, we use an α of 1 for artificial viscosity.

The GTVF (Zhang *et al.*, 2017b) eliminates the tensile instability while using the special PST proposed in the original paper. We show that the GTVF (Zhang *et al.*, 2017b) scheme is unable to eliminate numerical fracture when a different PST algorithm is employed. Instead of using the standard GTVF homogenization acceleration we use Sun's particle shifting technique (SPST). This results in a numerical fracture, as seen in fig. 2.18b. We reproduced the same case with original GTVF scheme, where no numerical fracture has found as seen in fig. 2.18a. This numerical fracture is eliminated by the current scheme. This is due to the incorporation of the additional terms in the current scheme as well as the use of momentum velocity in the computation of the velocity gradient. Note that a particle spacing of $\Delta x = 0.002$ m and $V_f = 0.05 \, \text{m s}^{-1}$ has been used.

This is further demonstrated by a case where an oscillating plate of length of 0.2 m and a height of 0.02 m is simulated for a time of 0.22 seconds. Similarly, another case where plate of height 0.01 m and a width of 0.2 m is run for a time of 0.51 s. Figure 2.19 and fig. 2.20 shows particles of the plate at time $t = 0.22$ s and 0.51 s of these two cases respectively. As we can see from the figure that the plate is free of numerical fracture, thus the tensile instability is eliminated.

figures/ctvf/figures/oscillating_plate/gtvf/figures/oscillating_plate/gtv

(a)   (b)
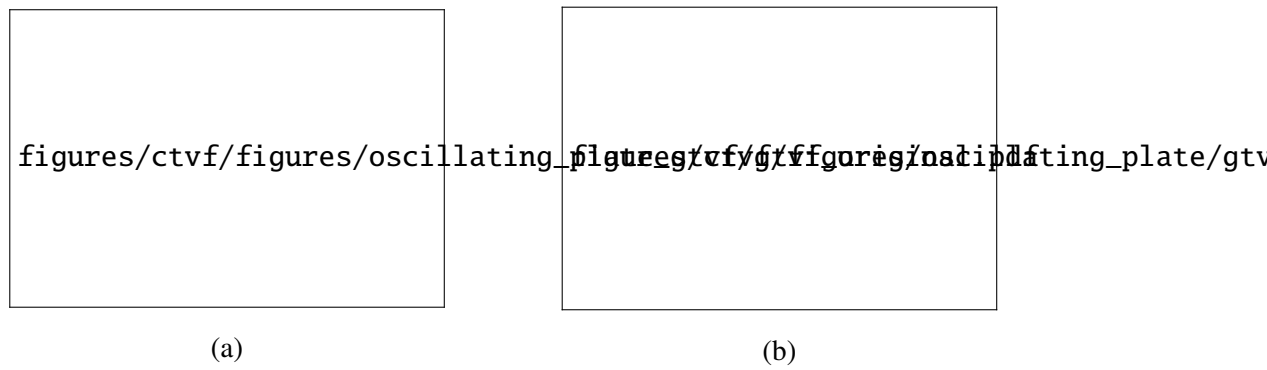
Figure 2.18: Oscillating plate with a length of 0.2m and height of 0.02m when simulated with GTVF Scheme. Figure in left is original GTVF scheme and right is while using SPST with GTVF scheme.

figures/ctvf/figures/oscillating_plate/etvf_sun2019_l_0_2_h_0_02.pdf

Figure 2.19: Oscillating plate at time $t = 0.22$s with a length of 0.2m and height of 0.02m simulated with SPST with CTVF scheme.

Figure 2.20: Oscillating plate at time $t = 0.51$s with a length of 0.2m and height of 0.01m simulated with SPST with CTVF scheme.

The accuracy of the current scheme is evaluated by comparing with the analytical results and with a convergence study. In table 2.1 we compare the time period for the oscillation by the analytical and the numerical results with varying V_f, where we consider an oscillating plate whose H/L ratio is 0.1. The difference between the analytical result and the numerical result is due to the fact that the analytical results are based on thin plate theory where as the plate considered here has a finite thickness. Further, we can see that the current numerical results are in agreement with the previously reported numerical results (Gray *et al.*, 2001b; Zhang *et al.*, 2017b). In fig. 2.21, we have performed a convergence study of an oscillating plate, with a $v = 0.3975$, and $V_f = 0.05$ m s^{-1}, and IPST is used for particle homogenization. The trend of the current scheme matches well with the other updated Lagrangian SPH schemes (Gray *et al.*, 2001b; Zhang *et al.*, 2017b). Hence the current scheme is able to work with different PST methods and remove the tensile instability.

V_f	0.001	0.01	0.03	0.05
T_{CTVF}	0.284	0.283	0.283	0.284
T_{GTVF}	0.284	0.283	0.284	0.285
$T_{analytical}$	0.254	0.252	0.254	0.254

Table 2.1: Comparison between the CTVF and the analytical solution for the time period of the oscillating plate with a length of 0.2m and height of 0.02m with various V_f
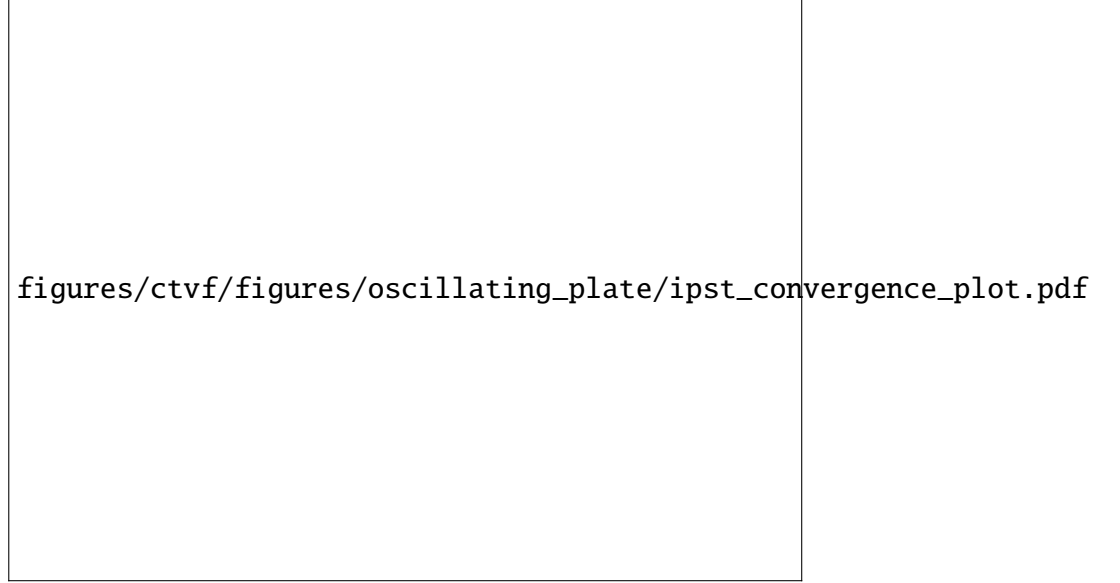
Figure 2.21: The vertical position of the particle at the end of the plate as a function of time. Here we consider a three particle variations, 10, 20 and 30 particles across the plate width.

2.4.5 Uniaxial compression

This benchmark is used to test the proposed scheme. A uniaxial bar is compressed by a moving piston on top of it. This problem has been simulated by Das and Cleary (2015). We compare the von Mises stress at the center point of the bar with the result of the FEM analysis and SPH provided in (Das and Cleary, 2015).

The numerical model consists of three parts. It has an axially loaded rectangular specimen of width 82 mm and height of 140 mm. The specimen has the properties of a sand stone (Crossley Sandstone) with a Young's modulus of 7.5 GPa and Poisson ratio of 0.398 and with a density of 2300 $\mathrm{kg\,m^{-3}}$. The speed of sound resulting from such properties is 2303 $\mathrm{m\,s^{-1}}$. We run three particle resolutions, $\Delta x = 0.5$ mm, 1 mm and 2 mm. The particles are placed on a regular square grid pattern. The velocity of the top plate is 1.5 $\mathrm{mm\,s^{-1}}$, which is used to apply the load on the specimen in such a fashion, such that the loaded end is deformed at the required constant rate. This is described in fig. 2.22. An α of 1 is used in the current simulation for the artificial viscosity.

We use the von Mises stress as the criterion for analysing the stress field. It combines the normal and shear components of the deviatoric stress tensor, and is a commonly used criterion to assess failure strength of materials. The von Mises stress σ_{vm} can be expressed in 2D in terms of principle stress σ_1 and σ_2 as

$$\sigma_{vm} = \sqrt{\left(\sigma_1^2 + \sigma_2^2 - \sigma_1\,\sigma_2\right)} \tag{2.68}$$

images/ctvf/images/uniaxial_compression/uniaxial_compression.pr

Figure 2.22: Test configuration of sand stone under uniaxial compression.

Where the principal stress are found by

$$\sigma_1 = \frac{\sigma_{xx} + \sigma_{yy}}{2} + \sqrt{\left(\left(\frac{\sigma_{xx} + \sigma_{yy}}{2}\right)^2 + \sigma_{xy}^2\right)} \tag{2.69}$$

$$\sigma_2 = \frac{\sigma_{xx} + \sigma_{yy}}{2} - \sqrt{\left(\left(\frac{\sigma_{xx} + \sigma_{yy}}{2}\right)^2 + \sigma_{xy}^2\right)} \tag{2.70}$$

Figure 2.23 shows the von Mises stress versus time of the current scheme, when simulated with three different resolutions compared against with the finite element result and SPH result provided in (Das and Cleary, 2015). It also shows the result with the GTVF scheme using the medium resolution. As can be seen in fig. 2.23 the GTVF result does not match very well with FEM and SPH result provided by Das and Cleary (2015), and the current scheme performs significantly better.

2.4.6 Colliding Rings

Having shown the flexibility of proposed scheme to work with different PST methods in section 2.4.4, in the current example, we compare the robustness of the PST methods by investigating the collision of rubber rings with different Poisson ratios. This was first studied in SPH by Swegle *et al.* (1995).

The inner ring radius of the ring is $r_{min} = 0.03$ m and the outer ring radius $r_{max} = 0.04$ m. Both the rings have the same material properties: Young's modulus $E = 0.01$ GPa and

Figure 2.23: von Mises stress at point A in uniaxial compression with three different resolutions compared against those from (Das and Cleary, 2015).

density $\rho = 1.2 \times 10^3$ kg m^{-3}. The initial speed of the rings are equal to $v_0 = 0.12c_0$ m s^{-1} with an initial inter particle spacing of $\Delta x = 0.001$ m. Where c_0 is the speed of sound of the material. We use an $\alpha = 1$ for the artificial viscosity in the current simulation.

Two different Poisson ratios are simulated. Figure 2.24 shows the particle positions of rings with a Poisson ratio of 0.3975 when simulated with SPST. The recovery of the colliding rings without any tensile instability can be seen.

We also consider higher Poisson ratios, such as 0.47. Figure 2.25 shows the particle positions of rings when simulated with SPST and fig. 2.26 with IPST. Even though both the particle shifting techniques are able to eliminate the numerical fracture, IPST gives better results as in the distribution of particles through out the simulation, see fig. 2.25b and fig. 3.10b. For the case where SPST is used, the final particle distribution is not very uniform. This is not the case when IPST is used. We can therefore say that IPST performs better than SPST. In order to compare the different schemes quantitatively for this problem, we plot the x and y positions of the point A of the left ring, as can be seen in fig. 2.27. Figure 2.28 shows the results and as can be seen excellent agreement of the different methods for this problem.

figures/ctvf/figures/rings/etvf_smooth_spots_for_figures/Di3037_etvf_sup_2019_poisson_r

(a) t = 2.5e-03 sec

(b) t = 4e-03 sec

figures/ctvf/figures/rings/etvf_smooth_spots_for_figures/Di3037_etvf_sup_2019_poisson_r

(c) t = 7.3e-03 sec

(d) t = 1.45e-02 sec

Figure 2.24: Rings with a Poisson ratio of 0.3975 colliding head on, simulated with CTVF using SPST.

figures/ctvf/figures/rings/etvf_smooth_spots_for_figures/Di47_etvf_sup_2019_poisson_r

(a) t = 2.5e-03 sec

(b) t = 4e-03 sec

figures/ctvf/figures/rings/etvf_smooth_spots_for_figures/Di47_etvf_sup_2019_poisson_r

(c) t = 7.3e-03 sec

(d) t = 1.45e-02 sec
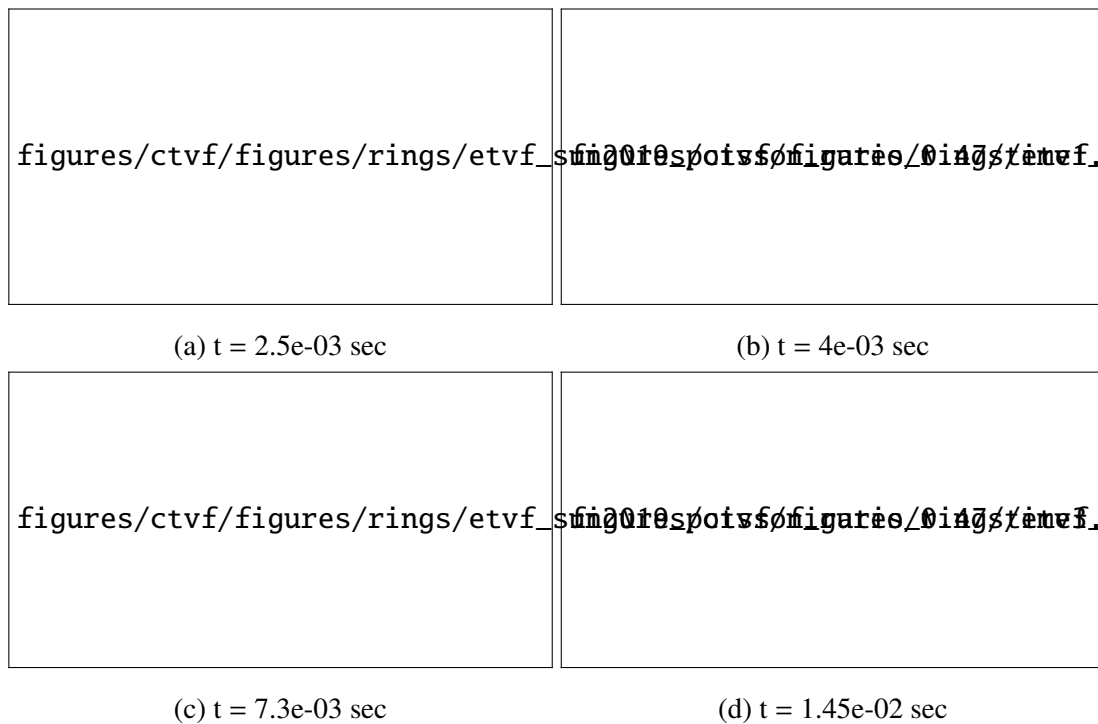
Figure 2.25: Rings with a Poisson ratio of 0.47 colliding head on, simulated with CTVF using SPST.

figures/ctvf/figures/rings/etvf_ipst_poisson_configuration_47/image.png ... ipst_poisson_

(a) t = 2.5e-03 sec   (b) t = 4e-03 sec

figures/ctvf/figures/rings/etvf_ipst_poisson_configuration_47/image.png ... ipst_poisson_

(c) t = 7.3e-03 sec   (d) t = 1.45e-02 sec
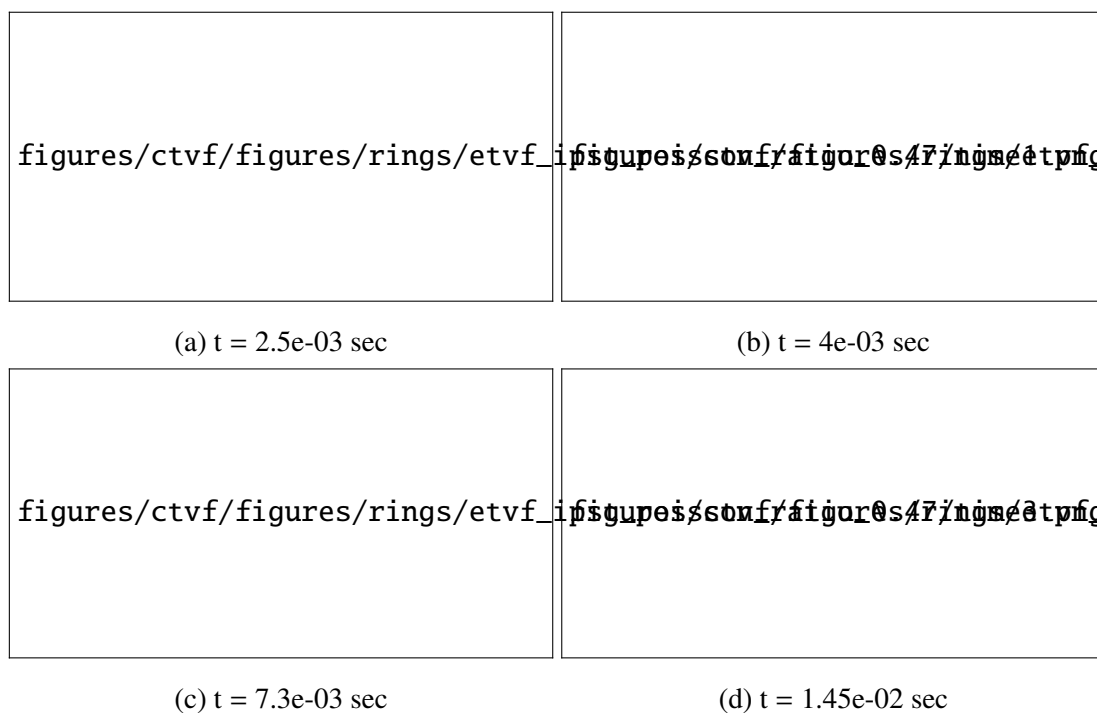
Figure 2.26: Rings with a Poisson ratio of 0.47 colliding head on, simulated with CTVF using IPST.

images/ctvf/images/rings/rings_initial.png
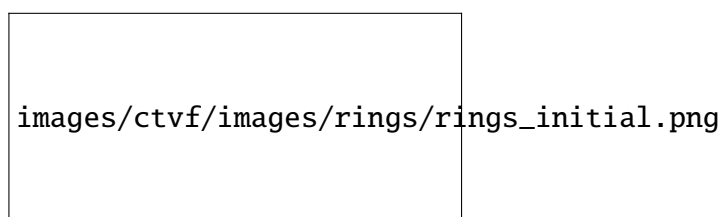
Figure 2.27: Schematic diagram of two rings colliding. Points A and B are marked.

figures/ctvf/figures/rings/sun_vs_ctvf_sun_vs_ipst_vs_gray_pdf_vs_ipst_vs_gra

(a) *x* coordinate of the point A   (b) *y* coordinate of the point A
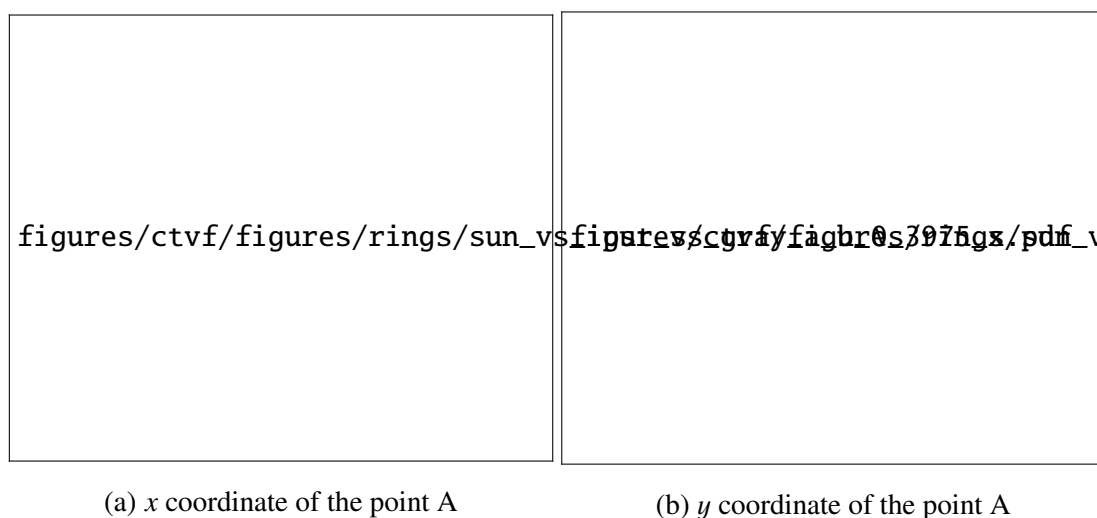
Figure 2.28: The evolution of the *x* and *y* coordinates of points A and B for the CTVF using SPST, IPST, and compared with that of Gray (Gray *et al.*, 2001b).

figures/ctvf/figures/high_velocity/figures/high_velocity/figures/high_velocity/time

(a) t = 0 sec   (b) t = 2.5e-03 sec   (c) t = 4e-03 sec

figures/ctvf/figures/high_velocity/figures/high_velocity/figures/high_velocity/time

(d) t = 7.3e-03 sec   (e) t = 1.45e-02 sec   (f) t = 1.5e-02 sec

figures/ctvf/figures/high_velocity/figures/high_velocity/figures/high_velocity/time

(g) t = 1.5e-02 sec   (h) t = 1.5e-02 sec   (i) t = 1.5e-02 sec

Figure 2.29: High velocity impact of cylinder on to a structure

2.4.7   High velocity impact

High-velocity impact problems are important in various contexts like space debris applications. This case tests if the scheme is capable of hand large deformation problems.

The projectile and the target are made of aluminium material. The projectile is 10mm in diameter and the rectangular target has a size of 2×50 mm. The projectile and the target have the following material properties: density $\rho = 2785$ kg m^{-3}, sound speed $c_0 = 5328$ m s^{-1}, shear modulus $G = 2.76 \times 10^7$ kPa, yield modulus $Y_0 = 3.0 \times 10^5$ kPa, as studied in (Zhang *et al.*, 2017b). The impact velocity is set to $V_0 = 3100.0$m s^{-1}. The initial particle spacing is $\Delta x = 0.5$ mm. Here the aluminium follows an elastic-perfectly plastic constitutive model. In elastic perfectly plastic model, the material is assumed to be elastic up to the yield point and once the material reaches the yield point, there will be no further increase in the stress, and is bounded by a factor $\beta = \min\left(\frac{Y_0^2}{3J_2}, 1\right)$, where J_2 is calculated from $J_2 = \frac{1}{2}\sigma' : \sigma'$. We use an $\alpha = 1$ in eq. (5.29) in the current case.

Figure 2.29 shows the plots of cylinder impacting the structure at different time instants. This is computed using the particle shifting technique of Sun (Sun *et al.*, 2019a). The color contour represents the pressure of the particles. The width of the hole created by the cylinder is 19.6 mm. When computed using the GTVF scheme (Zhang *et al.*, 2017b) the hole has a size of 19.8 mm. In Howell and Ball (2002), the value citepd is 19.2 mm. We can see, that the current scheme is closer to the one simulated by (Howell and Ball, 2002), which is taken as reference in (Zhang *et al.*, 2017b).

2.5 Summary

The proposed CTVF scheme builds on the original TVF scheme of Adami *et al.* (2013a) and is as an improvement on the GTVF of Zhang *et al.* (2017b). In addition it generalizes the implementation of the EDAC-SPH method (Ramachandran and Puri, 2019) where the TVF formulation was used for internal flows and a separate WCSPH formulation used for fluid flows with a free-surface. The current work proposes the addition of a few correction terms which improve the accuracy of the method as demonstrated in the earlier section. The addition of the terms imposes a small computational cost but compensates through the improved accuracy. As an example, in simulating the lid-driven cavity problem with a resolution of 50×50, the original EDAC scheme without any of the correction terms with a one step predictor corrector integrator takes 251 seconds for a time of 25 seconds, the new scheme with a kick-drift-kick scheme takes 293 seconds. Despite the change of the integrator this is a small increase in the performance. For solid mechanics problems we consider the colliding rings problem simulated for a total time of 0.016 seconds. This takes 98 seconds of time to simulate with the full CTVF scheme, and takes 73 seconds without the corrections (run on Intel i5-7400, quad core machine). Free-surfaces are handled carefully. The method produces smoother pressure fields due to the use of the EDAC scheme. Finally the method is robust to changes in the PST method used. This has been demonstrated using both the PST of Sun *et al.* (2019a) and the IPST of Huang *et al.* (2019).

An important feature of the proposed scheme is that it works well in the context of both fluid mechanics and solid mechanics. For elastic dynamics we propose correction terms that improve the accuracy and robustness of the method. The GTVF (Zhang *et al.*, 2017b) method fails when the PST method is changed as demonstrated in section 2.4.4, however the proposed method is more robust. Furthermore, our method uses the true velocity in order to compute the velocity gradient. The results of the uniaxial compression problem in section 2.4.5 suggest that that the proposed method is more accurate than the

GTVF. The main difference between the GTVF and the current scheme in the context of solid mechanics is the addition of the correction terms to the continuity equation, the usage of momentum velocity **u** in the computation of the velocity gradient, and the new particle shifting technique incorporation. We have found that the additional terms arising in the equation for the Jaumann stress rate eq. (3.7) has negligible influence and can be safely ignored. However, the computations in this work have included this term. The additional stress term in the momentum equation is negligible and has not been employed. We reiterate that for the fluid mechanics simulations the additional stress terms in the momentum equation are not negligible.

We note that for solid mechanics problems the method works well with either the traditional state equation used for the pressure evolution or the use of the EDAC equation. This does not make a significant difference for these problems since there is no additional damping added to the evolution equation for the deviatoric stresses. The EDAC evolution equation does make a significant improvement to the pressure evolution in the fluid mechanics problems as discussed earlier in (Ramachandran and Puri, 2019).

The newly proposed method has not been applied to three dimensional problems or to fluid structure interaction (FSI) problems. We believe that the method would be easier to use in the context of FSI since it can handle both fluids and solids in the same formulation. We propose to investigate these in the future.

In the current chapter, we have developed a transport velocity formulation-based method in SPH to solve fluid and solid dynamics problems. The developed method is robust and is able to eliminate several issues raised in conventional SPH. We have an updated Lagrangian solver with reasonable fidelity, which can solve fluid and elastic problems. As part of developing a water jet machining framework, we can couple the improved technique to handle various multiphysics problems in water jet machining. In the next chapter, we will model the collision among impacting bodies when they are assumed as elastic. We will extend the current solver to handle the collision between the elastic solids, where the collision is dealt with a contact force using the boundary particles. Using a contact force model, we will eliminate various issues SPH faces while handling the collision of elastic objects, and additionally, we will incorporate friction between the colliding bodies.

Chapter 3

Collision SPH

3.1 Introduction

With several particles impinging the target while solid particle erosion, the particles among themselves collide. One needs to model the interaction between these impacting bodies to handle the collision among these colliding bodies when they are elastic. Such contact modeling allows us to handle the interaction between the target and the impactor when they are assumed as elastic or elastic-plastic. The currently developed solver leads to unphysical interactions in modeling the collision of objects when they are close by but not touching. Further, the solver doesn't incorporate the friction between the colliding bodies. In the current chapter, a contact force model is incorporated into the existing solver to handle the interaction between the colliding solids. Specifically, we consider bodies with arbitrary shapes.

The collision of arbitrary solid bodies occurs everywhere around us. Apart from the elastic collision of bodies, other important examples include surface erosion, waterjet machining (Natarajan *et al.*, 2020), and machining processes (Islam *et al.*, 2020) to note a few. It is important to be able to simulate such problems accurately.

In the current work, the collision between elastic solids is modeled using a penalty-based contact force model. Unlike the approach of (Yan *et al.*, 2021), the proposed contact force model can handle friction between the solids as well. The bodies themselves are elastic and this is simulated using the CTVF SPH method (Adepu and Ramachandran, 2021). The penalty-based force considered here is the one proposed by Mohseni-Mofidi *et al.* (2021). In the original model proposed by (Mohseni-Mofidi *et al.*, 2021), the contact force is between a primary body and a secondary body. In (Mohseni-Mofidi *et al.*, 2021), the primary body is usually treated as the rigid body and the body on which the erosion is simulated is treated as secondary. It is not clear what would happen if both bodies were

elastic or if there is no clear way to distinguish between a primary and secondary body. We explore these questions in the present work. The work of Mohseni-Mofidi *et al.* (2021) takes inspiration from that of Vyas *et al.* (2021) where too there is a clear distinction between primary and secondary bodies. Vyas *et al.* (2021) also consider the collision between a rigid and elastic body. In the present work we only implement the collision model of (Mohseni-Mofidi *et al.*, 2021) due to its simplicity. The model proposed by Vyas *et al.* (2021) is more complex to implement. Several examples are simulated to validate the current scheme, ranging from simulations compared with FEM, analytical results as well as experimental. Finally, in the interest of reproducibility and easier ability for researchers to build on this work, our code is open source and can be found at `https://gitlab.com/pypr/collision_sph`. We use the `automan` package (Ramachandran, 2018b) to automate all the results generated in the current manuscript.

This current chapter is structured as follows. In section 3.2, we demonstrate the numerical method utilized to model the dynamics of collision of frictional elastic solids. In section 3.3, we present the contact force model used to resolve the collision among the elastic bodies. The results are provided in section 5.4, where different problems from the literature are simulated to show the capability of the current solver. Problems with collision involving two and multiple frictional and friction-less elastic solids are simulated.

3.2   SPH model for structural dynamics

3.2.1   Discrete governing equations

The governing equations of CTVF(Adepu and Ramachandran, 2021) scheme including the new contact force term are:

$$\frac{\tilde{d}\rho_a}{dt} = \sum_{b \in A} \frac{m_b}{\rho_b} \left(\rho_a \, \tilde{\mathbf{u}}_{ab} \; + \; (\rho \, (\tilde{\mathbf{u}} \; - \; \mathbf{u}))_{ab} \right) \cdot \nabla_a W_{ab}, \tag{3.1}$$

$$\frac{\tilde{d}\mathbf{u}_a}{dt} = - \sum_{b \in A} m_b \left[\left(\frac{p_a}{\rho_a^2} + \frac{p_b}{\rho_b^2} \right) \mathbf{I} - \left(\frac{\sigma'_a}{\rho_a^2} + \frac{\sigma'_b}{\rho_b^2} + \Pi_{ab}\mathbf{I} \right) \right] \cdot \nabla_a W_{ab} + \mathbf{g}_a + \frac{1}{m_a} \sum_{b \in B} \mathbf{F}^{\text{cont}}_{a \leftarrow b}. \tag{3.2}$$

In the above equations, the density, mass, pressure, deviatoric stress, momentum velocity, and transport velocity of particle a are denoted by ρ_a, m_a, p_a, σ'_a, $\mathbf{u}_a$ and $\tilde{\mathbf{u}}_a$ respectively. $\mathbf{g}_a$, is the acceleration due to gravity and $\mathbf{F}^{cont}_a$ is the force acting on particle a due to

contact with the other elastic bodies which will be discussed in section 3.3. The pressure p_a is evaluated using an equation of state:

$$p_a = K \left(\frac{\rho_a}{\rho_0} - 1 \right). \tag{3.3}$$

Figure 3.1: Bodies under collision which are divided into primary and secondary.

Where, $K = \rho_0 c_0^2$ is bulk modulus of the body, with $c_0 = \sqrt{\frac{E}{3(1-2\nu)\rho_0}}$ is speed of sound, while ρ_0 as the initial density of the particles. Here, E and ν are Young's modulus and Poisson ratio of the body. The modified material derivative ($\frac{\tilde{d}}{dt}$) is given as,

$$\frac{\tilde{d}}{dt} = \frac{\partial}{\partial t} + \tilde{u}_j \frac{\partial}{\partial x_j}. \tag{3.4}$$

The additional artificial viscosity term Π_{ab} (Monaghan, 2005b) in the momentum eq. (3.2) is to maintain the stability of the numerical scheme, given as,

$$\Pi_{ab} = \begin{cases} \frac{-\alpha h_{ab} \bar{c}_{ab} \phi_{ab}}{\bar{\rho}_{ab}} & \mathbf{u}_{ab} \cdot \mathbf{r}_{ab} < 0, \\ 0 & \mathbf{u}_{ab} \cdot \mathbf{r}_{ab} \ge 0, \end{cases} \tag{3.5}$$

where,

$$\phi_{ab} = \frac{\mathbf{u}_{ab} \cdot \mathbf{r}_{ab}}{r_{ab}^2 + 0.01 h_{ab}^2}, \tag{3.6}$$

where $\mathbf{r}_{ab} = \mathbf{r}_a - \mathbf{r}_b$, $r_{ab} = |\mathbf{r}_{ab}|$, $\mathbf{u}_{ab} = \mathbf{u}_a - \mathbf{u}_b$, $h_{ab} = (h_a + h_b)/2$, $\bar{\rho}_{ab} = (\rho_a + \rho_b)/2$, $\bar{c}_{ab} = (c_a + c_b)/2$, α is the artificial viscosity parameter, and h_a is the smoothing length.

Deviatoric stress σ_a evolution follows the Hooke's stress as,

$$\frac{d\sigma'_{ij}}{dt} = 2G(\dot{\epsilon}_{ij} - \frac{1}{3}\dot{\epsilon}_{kk}\delta_{ij}) + \sigma'_{ik}\Omega_{jk} + \Omega_{ik}\sigma'_{kj}, \tag{3.7}$$

where, G is the shear modulus, $\dot{\epsilon}_{ij}$ is the strain rate tensor, $\dot{\epsilon}_{ij} = \frac{1}{2}\left(\frac{\partial u_i}{\partial x_j} + \frac{\partial u_j}{\partial x_i}\right)$, and $\Omega_{ij} = \frac{1}{2}\left(\frac{\partial u_i}{\partial x_j} - \frac{\partial u_j}{\partial x_i}\right)$ is the rotation tensor. Here, SPH discretization of the gradient of velocity is given as, $\nabla \mathbf{u}_a = -\sum_{b \in A} \frac{m_b}{\rho_b}(\mathbf{u}_a - \mathbf{u}_b) \otimes (\nabla_a W_{ab})$, where $\otimes$ is the outer product.

The position of the particle is moved using the transport velocity, given as,

$$\frac{d\mathbf{r}_a}{dt} = \tilde{\mathbf{u}}_a, \tag{3.8}$$

where, $\mathbf{r}_a$ is the position of the particle a. The transport velocity $\tilde{\mathbf{u}}_a$ is computed with,

$$\tilde{\mathbf{u}}_a(t + \Delta t) = \mathbf{u}_a(t) + \Delta t \frac{\tilde{d}\mathbf{u}_a}{dt} + \left(\frac{d\mathbf{u}_a}{dt}\right)_{\mathrm{c}} \Delta t. \tag{3.9}$$

$\left(\frac{d\mathbf{u}_a}{dt}\right)_{\mathrm{c}}$ is the homogenization acceleration in eq. (3.9) and is computed with an iterative particle shifting technique (IPST) (Huang *et al.*, 2019). In IPST, at each time instant a shifting vector of particle a is computed as

$$\delta r_a^k = U_{\mathrm{IPST}} \, \Delta t \sum_{b \in A} (V_b \, \mathbf{n}_{ab} \, W_{ab}), \tag{3.10}$$

where k is the iteration number, $k = (1, 2, 3, \dots)$. U_{IPST} is taken to be four times the maximum velocity of the particles, can possibly achieve in a given simulation, found from the numerical experiments. The particles are then moved as,

$$\mathbf{r}_a^{k+1} = \mathbf{r}_a^k + \delta \mathbf{r}_a^k. \tag{3.11}$$

New particle positions are found until the convergence criterion is achieved, defined as,

$$|\max(\chi_a^k) - \overline{\chi_a^k}| \le \epsilon, \tag{3.12}$$

where

$$\chi_a^k = h^2 \sum_{b \in A} W_{ab}^k. \tag{3.13}$$

Here $\overline{\chi_a^k}$ is set to the maximum value of all the particles at initial configuration, which corresponds to the free surface particle. We find setting the value to the maximum gives better tensile instability control.

Using the initial ($\mathbf{r}_a^0$) and final ($\mathbf{r}_a^K$) positions at the given time instant, $\left(\frac{d\mathbf{u}_a}{dt}\right)_{\mathrm{c}}$ is computed as,

$$\left(\frac{d\mathbf{u}_a}{dt}\right)_{\mathrm{c}} = 2 \frac{\mathbf{r}_a^K - \mathbf{r}_a^0}{\Delta t^2}, \tag{3.14}$$

where $\mathbf{r}_a^K$ is the final position of the particle a.

The particle shifting force needs to be adjusted near the free surface, this is due to the lack of support for the particles near the free-surface. In order to do so we first identify the particles on the free surface, which starts with the computation of $\mathbf{n}_a^*$,

$$\mathbf{n}_a^* = \sum_{b \in A} -\frac{m_b}{\rho_b} \nabla_a W_{ab}, \tag{3.15}$$

where, particles with the magnitude of $\mathbf{n}_a^*$ less than $\frac{1}{4h_a}$, is set to zero else we normalize. Next, we smooth $\mathbf{n}_a^*$ using an SPH approximation,

$$\hat{\mathbf{n}}_a = \sum_{b \in A} \frac{m_b}{\rho_b} \mathbf{n}_b^* W_{ab}. \tag{3.16}$$

Finally, we compute the normals by normalizing $\hat{\mathbf{n}}_a$,

$$\mathbf{n}_a = \frac{\hat{\mathbf{n}}_a}{\|\hat{\mathbf{n}}_a\|}. \tag{3.17}$$

The PST is treated near the free surface by adjusting the increment in the position near the free surface. We employ a new variable, h_b, initialized to smoothing length h. For particles near the free surface, it is readjusted to a value such that its kernel support is up to the closest boundary particle. This algorithm identifies the particles close to the free surface. By using the identified free surface particles, and particles near the free surface, the increment of the position is adjusted as,

$$\delta\mathbf{r}_a = \begin{cases} 0 & \text{if free-surface,} \\ \delta\mathbf{r}_a - (\delta\mathbf{r}_a \cdot \mathbf{n}_a)\mathbf{n}_a & \text{if } h_b < h, \\ \delta\mathbf{r}_a & \text{if } h_b = h. \end{cases} \tag{3.18}$$

3.2.2 Time integration

The time integration follows a kick-drift-kick scheme: first we move the velocities of the particles to half time step by using the acceleration at the nth time step,

$$\begin{aligned} \mathbf{u}_a^{n+\frac{1}{2}} &= \mathbf{u}_a^n + \frac{\Delta t}{2}\left(\frac{\tilde{d}\mathbf{u}_a}{dt}\right)^n, \\ \tilde{\mathbf{u}}_a^{n+\frac{1}{2}} &= \mathbf{u}_a^{n+\frac{1}{2}} + \frac{\Delta t}{2}\left(\frac{d\mathbf{u}_a}{dt}\right)^n_c. \end{aligned} \tag{3.19}$$

The time derivatives of density and deviatoric stresses are calculated using the eq. (3.1) and eq. (3.7) by utilizing the velocities at $n+\frac{1}{2}$ time step. The density, deviatoric stresses and particle position are updated by,

$$\rho_a^{n+1} = \rho_a^n + \Delta t\left(\frac{\tilde{d}\rho_a}{dt}\right)^{n+\frac{1}{2}}, \tag{3.20}$$

$$\sigma_a^{\prime\,n+1} = \sigma_a^{\prime\,n} + \Delta t\left(\frac{\tilde{d}\sigma_a^\prime}{dt}\right)^{n+\frac{1}{2}}, \tag{3.21}$$

$$\mathbf{r}_a^{n+1} = \mathbf{r}_a^n + \Delta t\,\tilde{\mathbf{u}}_a^{n+1}. \tag{3.22}$$

Finally, the momentum velocity is updated to the n+1 time step

$$\mathbf{u}_a^{n+1} = \mathbf{u}_a^{n+\frac{1}{2}} + \frac{\Delta t}{2}\left(\frac{\tilde{d}\mathbf{u}_a}{dt}\right)^{n+1}. \tag{3.23}$$

For the numerical stability, the time step is set based on the CFL criterion,

$$\Delta t \le 0.25\left(\frac{h}{c_0 + |U|}\right), \tag{3.24}$$

and $|U|$ is the maximum velocity magnitude.

3.3   Contact algorithm

In the current work we have utilized the contact force model proposed by Mohseni-Mofidi *et al.* (2021). The force acting on a particle *a* of body A due to the interaction with the particles of body *B* can be resolved into a normal and tangential component. The normal force component is utilised to make sure that the particles of different body do not penetrate into each other, while the tangential component is used to model the friction between the interacting solids. According to Mohseni-Mofidi *et al.* (2021), we divide the bodies under interaction into primary and secondary bodies, as shown in fig. 6.1. The normal force (F_a^n) on particle *a* due to the interaction with the particles *b* of body *B* is computed as,

$$\mathbf{F}_a^n = k_r \delta_{n^c}^a \mathbf{n}_a^c. \tag{3.25}$$

Here, the overlap $\delta_{n^c}^a$ is computed using

$$\delta_{n^c}^a = \Delta x - d_a, \tag{3.26}$$

where,

$$d_a = \frac{\sum\limits_{b=1}^{\text{NP}^b} (\mathbf{n}_a^c \cdot \mathbf{r}_{ab}) \dfrac{m_b}{\rho_b} W_{ab}}{\sum\limits_{b=1}^{\text{NP}^b} \dfrac{m_b}{\rho_b} W_{ab}}, \tag{3.27}$$

and the normal contact vector $\mathbf{n}_a^c$ is computed using

$$\hat{\mathbf{n}}_a^c = \frac{\sum\limits_{b=1}^{\text{NP}^b} \dfrac{\mathbf{r}_{ab}}{r_{ab}} \dfrac{m_b}{\rho_b} W_{ab}}{\sum\limits_{b=1}^{\text{NP}^b} \dfrac{m_b}{\rho_b} W_{ab}}, \tag{3.28}$$

$$\mathbf{n}_a^c = \frac{\hat{\mathbf{n}}_a^c}{\|\hat{\mathbf{n}}_a^c\|}. \tag{3.29}$$

With Δx being the initial spacing between the particles, k_r is the normal spring stiffness coefficient. Note that while computing the overlap of particle *a* with the body *B* we have computed an effective overlap, rather than per particle interaction. This effectively is able to model the interaction between non smooth surfaces in contrast with particle-particle force computation.

3.3.1   Tangential force computation

We associate a tangential spring attached to particle *i* and body *B* to compute the tangential force, which initially has a magnitude of zero ($|\Delta l_a| = 0$). And the tangential

spring is activated when the particle comes into contact with body *B*. The tangential force is history-dependent. The contact friction force is proportional to the tangential spring displacement, which is integrated over the contact time as

$$\mathbf{F}_a^{t^{n+1}} = -k_f \Delta \mathbf{l}_a^{n+1} = -k_f[(\Delta \mathbf{l}_a^n + \mathbf{v}_{ab}^{n+1}\Delta t) \cdot \mathbf{t}_a^{n+1}] \, \mathbf{t}_a^{n+1}, \qquad (3.30)$$

where Δt is the time step, $\mathbf{v}_{ab} = \mathbf{v}_a - \mathbf{v}_b$ is the relative velocity of the primary particle *a* with respect to the closest secondary particle *b*, and k_f is the tangential spring stiffness coefficient. The tangential unit vector is computed by,

$$\mathbf{t}_a = \frac{\mathbf{v}_{ab} - (\mathbf{v}_{ab} \cdot \mathbf{n}_a^c)\mathbf{n}_a^c}{|\mathbf{v}_{ab} - (\mathbf{v}_{ab} \cdot \mathbf{n}_a^c)\mathbf{n}_a^c|}. \qquad (3.31)$$

The tangential force is coupled to the normal force through the Coulomb's law,

$$\mathbf{F}_a^t = \min(\mu|\mathbf{F}_a^n|, |\mathbf{F}_a^t|) \, \frac{\mathbf{F}_a^t}{|\mathbf{F}_a^t|}. \qquad (3.32)$$

This allows us to impose the sliding friction condition between the interacting solids. Finally, the total force acting on the particle *a* due to the interaction with body *B* is:

$$\mathbf{F}_a^{\text{cont}} = \mathbf{F}_a^n + \mathbf{F}_a^t \qquad (3.33)$$
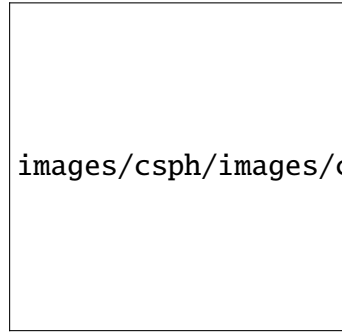
Figure 3.2: Force transfer to the secondary particles *b* from the primary body particle *a*

An equal and opposite force of the same magnitude is applied to the closest secondary particle *b* of *a* as shown in fig. 3.2,

$$\mathbf{F}_b^{\text{cont}} = -\mathbf{F}_a^{\text{cont}}. \qquad (3.34)$$

The current contact force model is sensitive towards the primary body chosen to compute the forces, i.e., the force acting on the particles is not the same when the primary bodies are interchanged. In the current work we have explored the behaviour of the current contact force model when different bodies are chosen as primary and secondary. Simulations such as, a rectangular solid sliding down an inclined plane, and a symmetric collision between elastic solids are two examples, where we have investigated how the bodies would behave when different bodies are chosen as primary.

3.4   Results and discussion

3.4.1   Curved interface
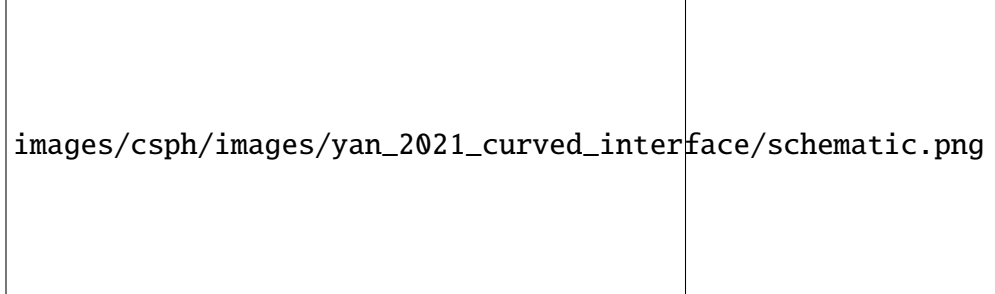
Figure 3.3: Collision between two circular elastic discs. The left disc moves towards the right disc with a constant velocity v_0, while the right disc is at rest.

The collision of two circular elastic solids is considered as the first test case. Figure 3.3 shows the initial configuration where the left disc is initially allowed to move towards the right with a velocity of 20 m s^{-1}. While no velocity is imposed on the right disc. The radius of each disk is 0.4 m, and made of Aluminium, whose material properties are shown in table 3.1. No friction and gravity is assumed in the current case. A particle spacing of 0.01 m is used, resulting in a 4779 number of particles per disc. The numerical parameters utilized in the current example are shown in table 3.2.

Quantity	Values
E, Young's modulus	72 GPa
v, Poisson's ratio	0.3
ρ, density	2785 kg m^{-3}
μ, friction coefficient	0
Time of simulation	4 ms
gravity $[g_x, g_y, g_z]$	$[0.0, 0.0, 0.0]$

Table 3.1: Material parameters used for the impact of curved interface problem.

Figure 3.4 shows the snapshots of particles of the circular disc under contact by the present approach including the stress (σ_{xx}) field at times $t = 0.0, 1.8, 4$ ms. From the figure, we can see that the current numerical scheme is able to reproduce smooth stress fields. The elastic discs are initially in stress free state, and once the bodies collide, the left disc transfers its momentum to the right. Since the discs are elastic, the total momentum

Quantity	Values
δx, Resolution	0.01
$h/\Delta x$, Smoothing length factor	1
α, artificial viscosity	1
β, artificial viscosity	0
k_r, Normal stiffness coefficient	10^{10}
k_f, Tangential stiffness coefficient	10^9

Table 3.2: Numerical parameters used for the impact of curved interface problem.

is not transferred, and the left disc will not come to a halt but rather starts moving with the free vibration of the disc.

(a) t = 0 ms

(b) t = 1.8 ms

(c) t = 4 ms
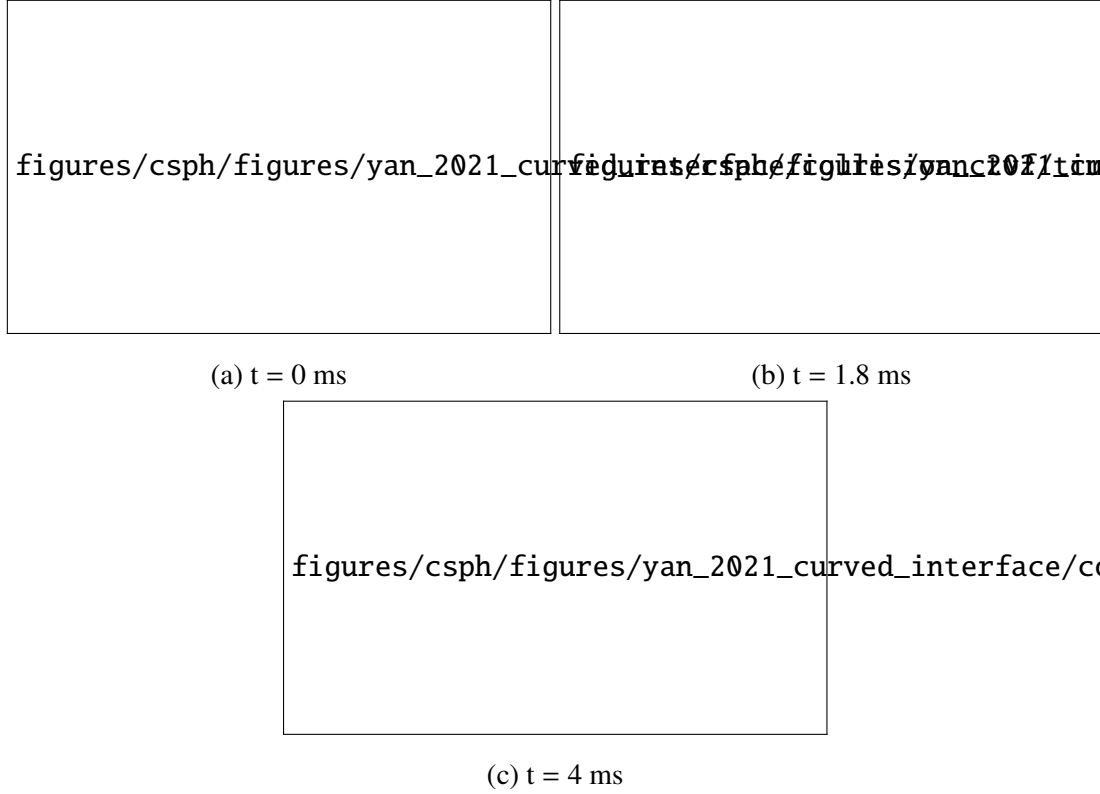
Figure 3.4: The stress field of the elastic discs at three different time instants through the collision.

Figure 3.5 presents the time histories of the velocity of the center of mass of both the discs in comparison with the results by FEM solver presented in (Yan *et al.*, 2021). The rebound the velocity of the bodies with the current scheme is in good match with the FEM result.

figures/csph/figures/yan_2021_curved_interface/velocity_vs_time.pdf

Figure 3.5: Time history of the x component of velocity of center of mass's of the left and the right disc, and compared with the numerical results produced using FEM, CTVF. The Young's modulus of the disc is taken as E=72 GPa.

We check if the elastic disk behave as a rigid disk with an increase in Young's modulus and is able to retrieve the rigid velocity. We expect the right disk to achieve the velocity of 20 m s^{-1} as the Young's modulus is increased. Figure 3.6 shows the variation of the final velocity of the right disc with Young's modulus, where we can see that the proposed model is behaving as expected.

figures/csph/figures/yan_2021_curved_interface/E_vs_velocity.pdf

Figure 3.6: Variation of the x-velocity of the center of mass with Young's modulus of the disc.

3.4.2 Flat interface

In the current section, we test our solver in handling collision between two elastic solids, where the collision front is flat in shape. The model is shown in fig. 3.7. Both the solids are of the same size, 0.2 m in length and 0.1 m in height. The material is the same as in the circular interface problem (section 3.4.1) and can be found in table 3.1, while the numerical parameters are listed in table 3.3. A particle spacing of 0.0025 m is used, resulting in 3321 particles per body.

```
images/csph/images/yan_2021_linear_interface/schematic.pdf
```

Figure 3.7: Collision between two rectangular elastic solids, where, the left solid is allowed to move towards the right solid with a constant velocity v_0, while the right solid is at rest.

Quantity	Values
$h/\Delta x$, Smoothing length factor	1
α, artificial viscosity	1
β, artificial viscosity	0
k_r, Normal stiffness coefficient	10^{11}
k_f, Tangential stiffness coefficient	10^9

Table 3.3: Numerical parameters used for the impact of linear interface problem.

Figure 3.8 shows the velocity of the center of mass of both the bodies using current scheme along with the formulation of Gray *et al.* (2001a) and with FEM results provided by Yan *et al.* (2021). From the fig. 3.8 we can see that rebound velocities match well with the FEM results provided, as well as the interaction between the bodies start when their physical boundaries have come into contact, in contrast to SPH, where the bodies interact when the other body is in its smoothing length influence. The rebound velocity of the current scheme is matches well with FEM result. Since the body is elastic after the collision, both the bodies move with the base oscillation amplitude which is the reason for the left body to not achieve absolute zero velocity. The current scheme results are better than the Adepu and Ramachandran (2021) SPH model.

figures/csph/figures/yan_2021_linear_interface/velocity_vs_time.pdf
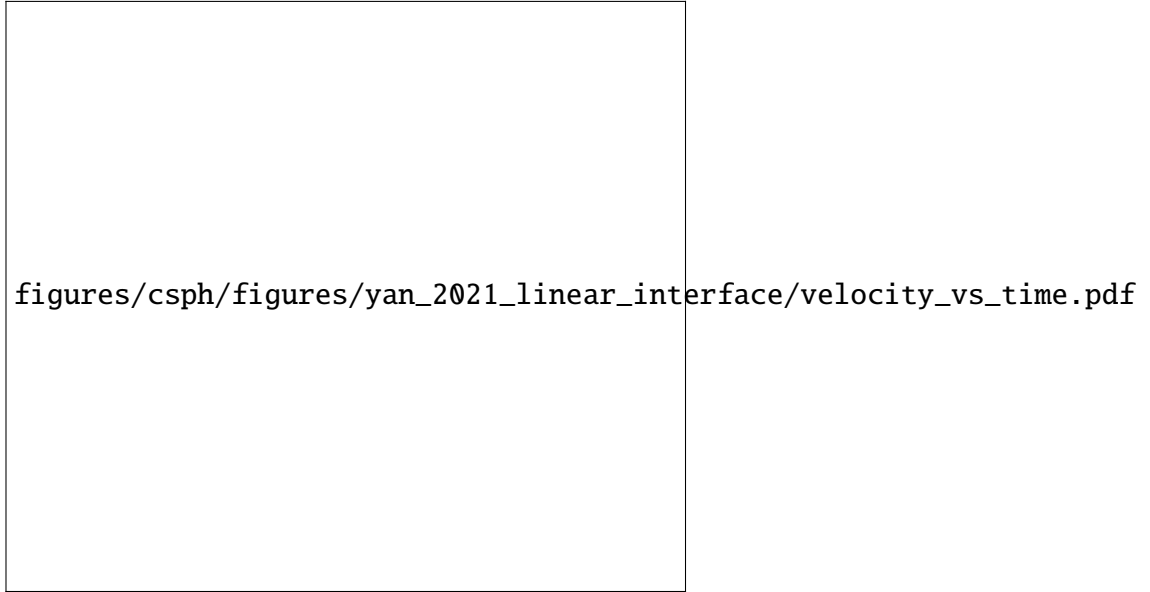
Figure 3.8: Time history of the x component of the center of mass's velocity of the left and the right rectangular bodies, and compared with the numerical results produced using FEM, SPH.

3.4.3 Colliding rubber rings

This test applies the current solver in modeling large deformation solids under collision. We consider the collision between two elastic rubber rings. This benchmark is simulated by various works in SPH literature, such as in Gray *et al.* (2001a); Adepu and Ramachandran (2021); Zhang *et al.* (2017a).

images/csph/images/yan_2021_colliding_rubber_rings/schematic.pdf
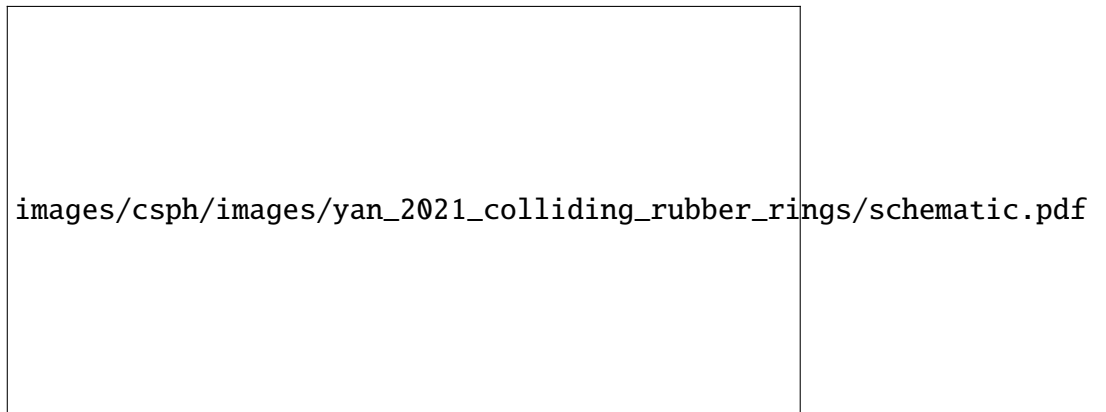
Figure 3.9: Schematic sketch of the initial setup of colliding rubber rings.

The initial positioning, as well as the dimensions of the rings, are shown in fig. 3.9. Both rings are made of the same material, whose material properties are listed in table 3.4, and the numerical parameters in table 3.5, respectively. The initial relative velocity at which the rings collide is $v_0 = 0.12c_0$ m s^{-1}.

Quantity	Values
E, Young's modulus	10 MPa
v, Poisson's ratio	0.47
ρ, density	1200 kg m^{-3}
μ, friction coefficient	0.0
Time of simulation	0.016 s
Resolution, δx	0.001 m
Smoothing length factor, $h/\Delta x$	1.3
gravity $[g_x, g_y, g_z]$	$[0.0, 0.0, 0.0]$

Table 3.4: Material parameters used for modeling the impact of elastic rubber rings.

Quantity	Values
α, artificial viscosity	1
β, artificial viscosity	0
k_r, Normal stiffness coefficient	10^7
k_f, Tangential stiffness coefficient	10^5

Table 3.5: Numerical parameters used for modeling the impact of elastic rubber rings.

The evolution of the rings is shown in fig. 3.10, we can see from the figure that the current model has reproduced a stable and smooth stress field. The rings are stress free before the collision, as shown in fig. 3.10a. Throughout the simulation phase, while the rings are colliding, the kinetic energy of the rings is transferred into elastic and vice versa. At the maximum deformation, the elastic energy stored in the rings is maximum. After that, both the rings bounce off and start to separate. Further, we can see the rings being under tension as well as compression, while it is deforming in fig. 3.10e. The results are consistent with other numerical methods proposed by Gray *et al.* (2001a) and Zhang *et al.* (2017a).

3.4.4 Near miss of two solids

In this section, we simulate two elastic solids which are not touching are moved towards each other with a constant velocity. We show that the current model is able to eliminate the unphysical interaction arises due to the conventional SPH which is due to the physical influence of the particles at the boundary. We expect no change in the velocity of the elastic solids as they pass by. We show that with the current model no

(a) t = 0 ms

(b) t = 1.38 ms

(c) t = 5.17 ms

(d) t = 7.38 ms

(e) t = 11.462 ms

(f) t = 15.4 ms
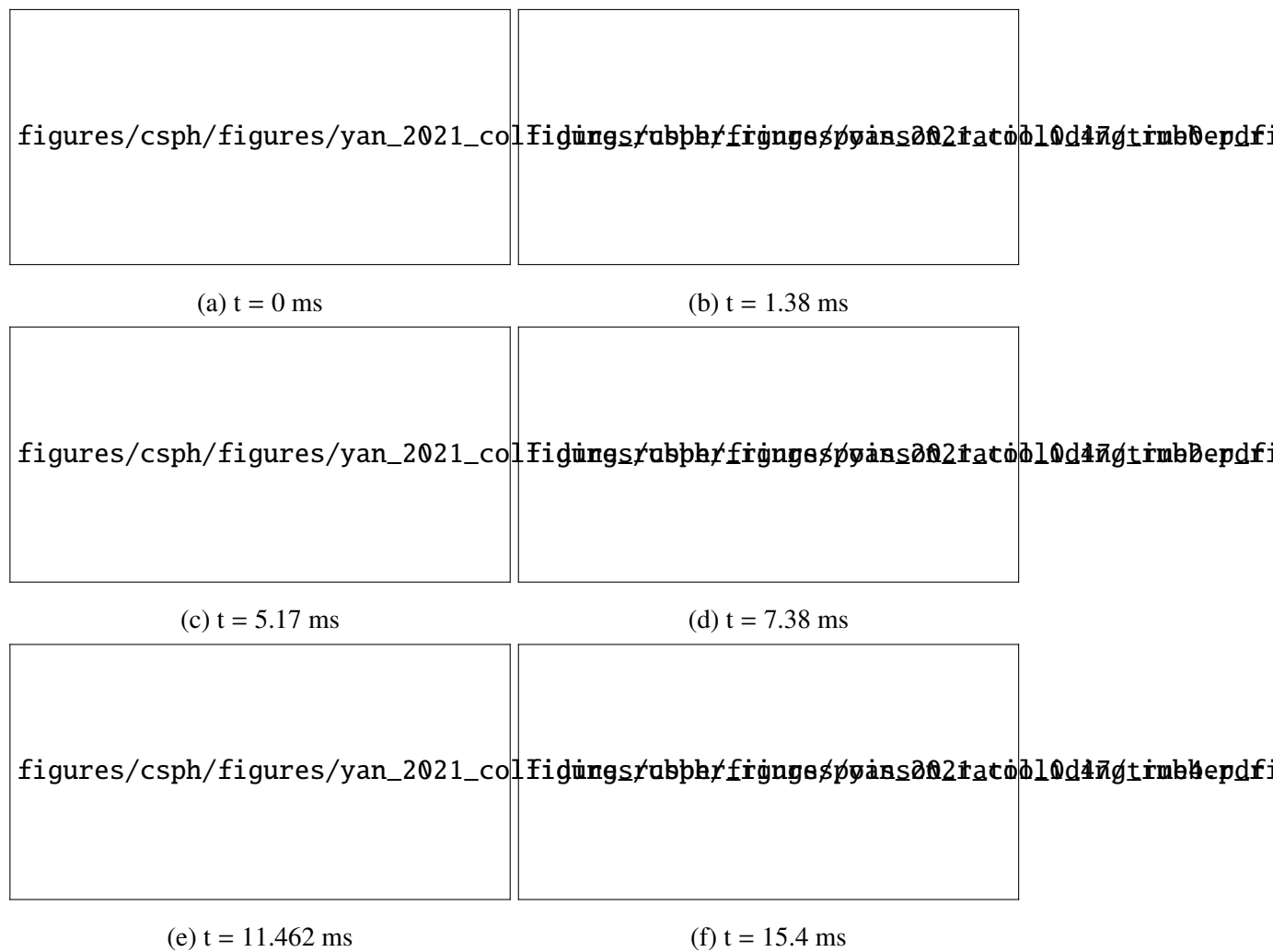
Figure 3.10: Snapshots of particle positions with color indicating the stress field (σ_{xx}) solved by the current solver.

interaction exists when the elastic solids are physically not touching, and no variation in their path is found. As a qualitative validation the particle plots is shown and for quantitative validation, variation of the velocity of the center of mass of the elastic body with time is considered.

images/csph/images/dinesh_2022_elastic_solids_passing_by/schematic.pn

Figure 3.11: Schematic of the two elastic solids which are placed close to each other and allowed to move at a constant velocity v_0.

The dimensions of the elastic bodies under consideration are as follows, the length and height are 0.2 m and 0.1 m, respectively. Both bodies are made of density 1200 kg m^{-3}, Youngạŕs modulus of 10 MPa and Poissonạŕs ratio of 0.4. The schematic is shown in fig. 3.11. The left body is allowed to move to the right in the x-direction with a velocity of $v_0 = 20$ m s^{-1}, and the right body with $v_0 = -20$ m s^{-1}. A particle spacing of dx = 0.0025 m is used, which results in 3321 particles per single body. We have turned off the particle shifting in the current test case as no deformation of the bodies is expected.

(a) t = 0 ms   (b) t = 1.4 ms

(c) t = 10 ms   (d) t = 12 ms

Figure 3.12: Snapshots of the bodies passing close by when simulated with CTVF.

Figure 3.12 shows the snapshots of bodies at multiple time instants simulated using the formulation of Adepu and Ramachandran (2021). From Figure 3.12 we can see that the bodies interact with each other though they are not touching physically, this is because in SPH the particles at the boundaries have an influence radius exceeding its material boundary. Because of the interaction, shear stresses develop, which results in strain in the body as well as it deviates from its path. Figure 3.13 shows the snapshots of bodies when simulated with the current contact force model with the current SPH formulation. From fig. 3.13, we can clearly see that the bodies don't interact and pass freely without

figures/csph/figures/dinesh_2022_elastic_solids_figures/dinesh_2022_elastic_collision_MonaghanVyas/time0.pdf

(a) t = 0 ms

(b) t = 1.4 ms

figures/csph/figures/dinesh_2022_elastic_solids_figures/dinesh_2022_elastic_collision_MonaghanVyas/time2.pdf

(c) t = 10 ms

(d) t = 12 ms
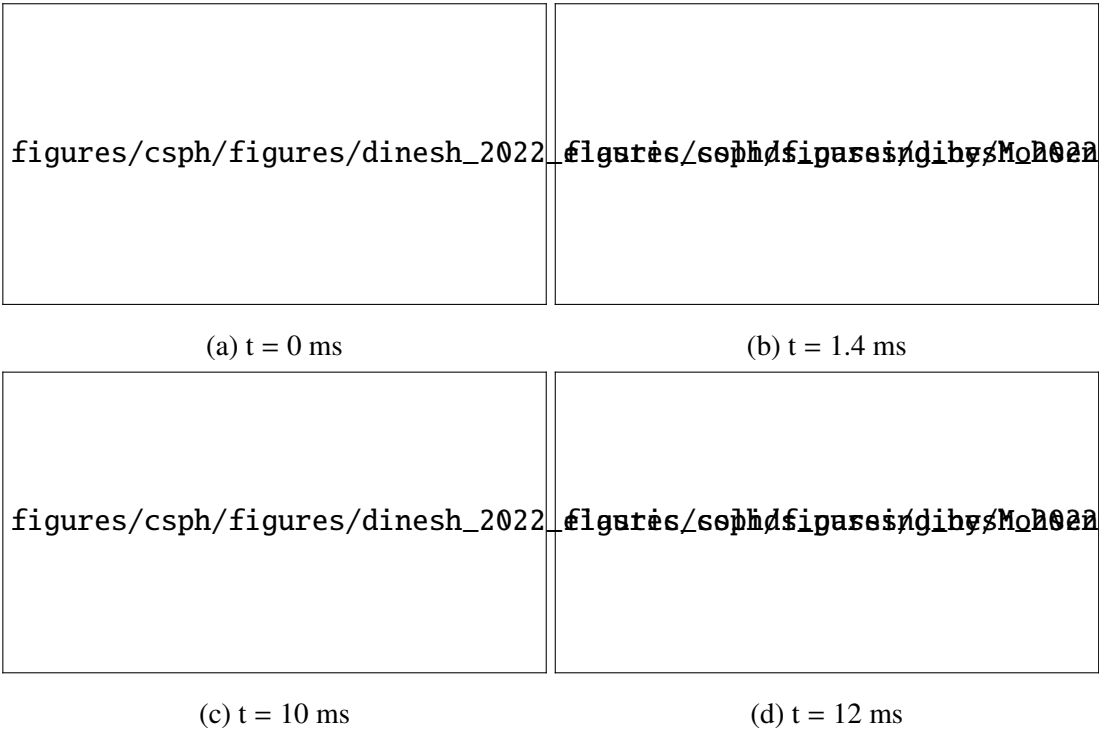
Figure 3.13: Snapshots of the bodies passing close by when simulated with current solver.

figures/csph/figures/dinesh_2022_elastic_solids_passing_by/velocity_vs_time_x.pdf
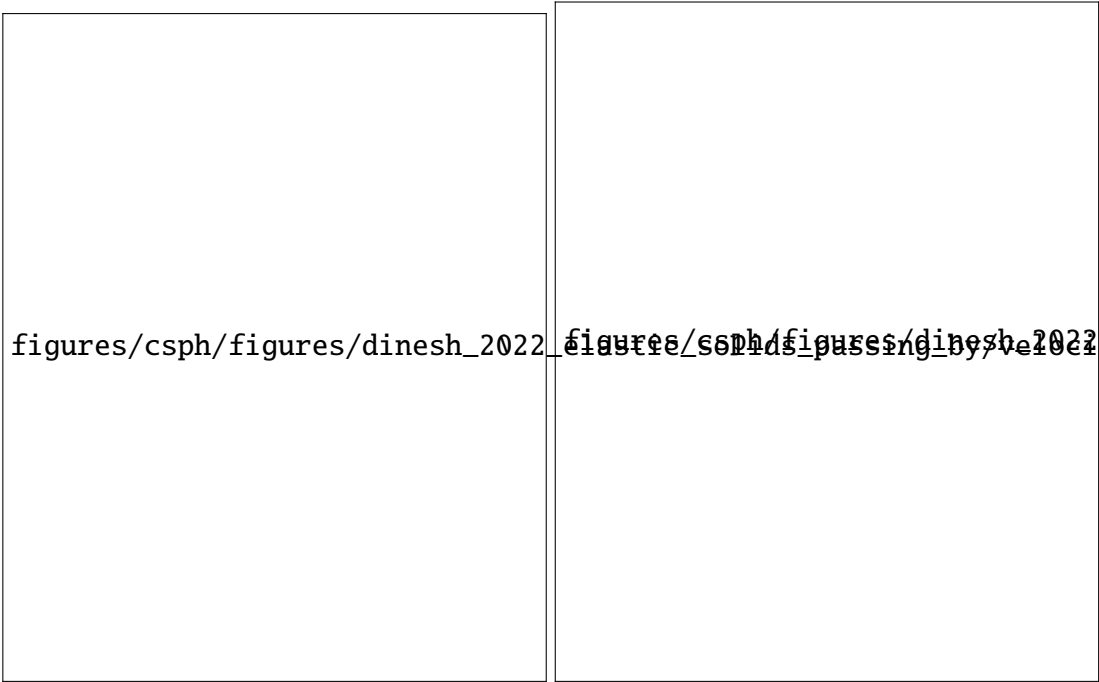
Figure 3.14: Time variation of the x-component and y-component of the velocity of the center of mass of the freely moving rectangular solids when simulated using the CTVF and the current solver.

any deformations or path divergence. Figure 3.14 shows a quantitative validation by considering the time history of the velocity of the center of mass in the x and y-direction. From fig. 3.14 we can see that the velocity of the left body, as well as the right body, is constant throughout the time. While a velocity in the y-direction is induced while simulated using Adepu and Ramachandran (2021) formulation. Hence the current scheme is successful in modeling the free moment of elastic solids passing close by each other.

3.4.5   Elastic solid sliding on a slope

In the current problem, we test if the current scheme models the friction between the elastic solids accurately. The free sliding of an elastic solid on a frictional inclined plane is studied. The initial placement of the elastic solid is shown in fig. 3.15.

figures/csph/figures/mohseni_2021_free_sliding_on_a_slope/f
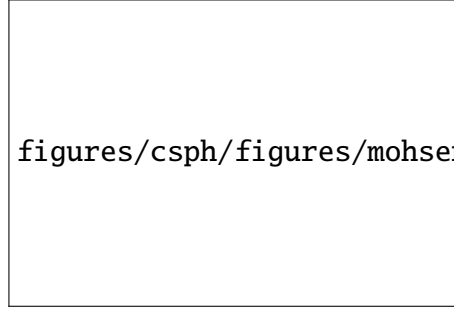
Figure 3.15: Schematic of an elastic body sliding on a frictional slope.

The dimensions of the elastic solid involved are as follows. An elastic solid of length 0.1 m and width 0.1 m is initially placed at zero velocity on an inclined plane at an angle of 30 degrees. The material properties are as follows: An Young's modulus of 10 MPa with a Poisson ratio of 0.3975 is considered. We have turned the particle homogenization off in the current problem, as the particle shifting effects are negligible. A stiffness coefficient k_r of 10^{10} in eq. (5.17) is used. From the analytical solution, we have the evolution of velocity as follows,

$$\mathbf{v}(t) = (\mu\boldsymbol{g}\sin(\theta) - \boldsymbol{g}\cos(\theta))t. \tag{3.35}$$

We consider three different frictional coefficients, $\mu = 0.2, 0.3, 0.4$ while modeling the sliding of the elastic solid. Snapshots at four time instants are depicted in fig. 3.16, corresponding to the frictional coefficient of 0.3. From fig. 3.16 we can see that the elastic solid slides without any oscillations. Figure 3.17 presents the time history of the velocity of center of mass of the elastic body along with the corresponding theoretical solution obtained by frictional coefficients of $\mu = 0.2$, 0.3, and 0.4. From fig. 3.17, the reproduced velocity is in good agreement with the corresponding theoretical solution for all the time.

(a) t = 0 sec

(b) t = 0.5 sec

(c) t = 1. sec

(d) t = 2 sec

Figure 3.16: Snapshots of the elastic solid sliding on an inclined plane at four time steps, where, the friction coefficient between the body and the plane is taken as 0.3.
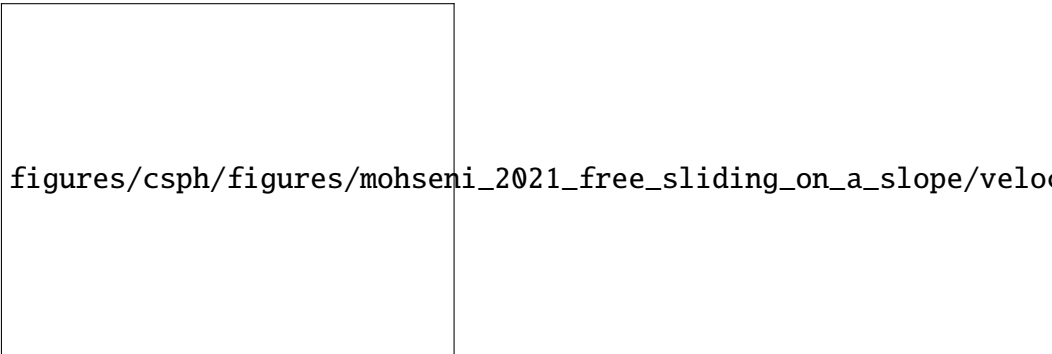
Figure 3.17: Time histories of the velocity of the elastic solid while sliding on an inclined plane for three frictional coefficients, plotted against the analytical solution.

3.4.6   Circular elastic body rolling on a plane

In the current section, the motion of a 2D elastic cylinder rolling on a frictional inclined plane is carried out. The theoretical and computational model are shown in fig. 3.18. In addition to section 3.4.5, the current problem will be helpful in testing the frictional part of the current formulation. A total of two coefficient of friction μ values are

(a)

(b)

Figure 3.18: The rolling body problem: (a) theoretical description (b) numerical model.

simulated. One with a slip case ($\mu = 0.3$) and with $\mu = 0.6$ corresponding to stick case, where the inclination of the plane is chosen to be $\theta = \pi/3$. Table 3.6 shows the material properties along with numerical parameters utilized in the current scheme. The analytical solution of the movement of the center of the circular body for different frictional coefficients is given as

$$x_{cm}(t) = \begin{cases} x_0 + \frac{1}{2}\, g\, t^2\, (\sin(\theta) - \mu \cos(\theta)) & \tan\theta > 3.5\mu, \\ x_0 + \frac{1}{3}\, g\, t^2\, \sin(\theta) & \tan\theta \le 3.5\mu. \end{cases} \tag{3.36}$$

Here, $g = 9.81$ is the magnitude of acceleration due to gravity.

Figure 3.19 and Figure 3.20 shows the snapshots of the cylinder at two different time instants along with the scaled velocity vectors for friction coefficients $\mu = 0.3$ and 0.6 respectively. Finally, fig. 3.21 and fig. 3.22 depicts the x position of the center of mass of the cylinder along with time for a slip and stick case. From these figures, we can see that the current scheme agrees well with the analytical solution.

3.4.7   A rigid sphere hitting a wall at different impact angles

In the current example, we simulate the impact of a 3D sphere on a wall at different incident angles, where the experimental evaluation is done by Thornton *et al.* (2011). The

figures/csph/figures/de_2021_cylinder_rolling/figures/de_2021_cylinder_rolling_on_an_inclined_plane/fig0o3/

(a)   (b)
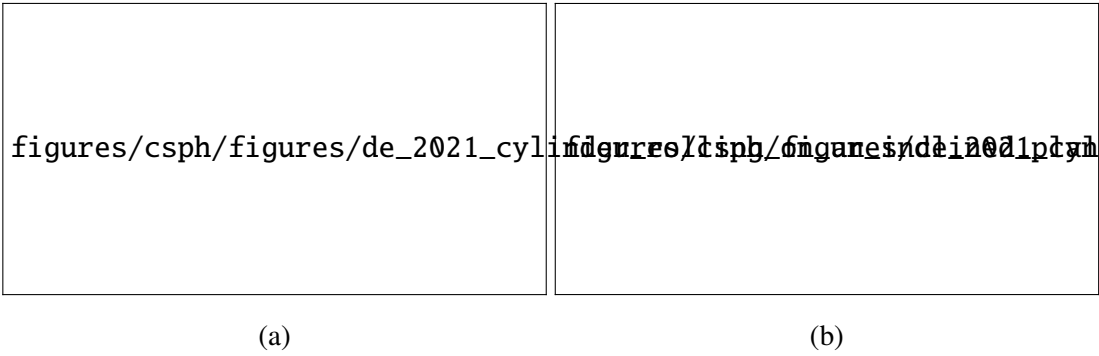
Figure 3.19: Snapshot of a rolling cylinder with the velocity vectors at two time steps for a friction coefficient of 0.3, corresponding to a slip case.

figures/csph/figures/de_2021_cylinder_rolling/figures/de_2021_cylinder_rolling_on_an_inclined_plane/fig0o6/

(a)   (b)
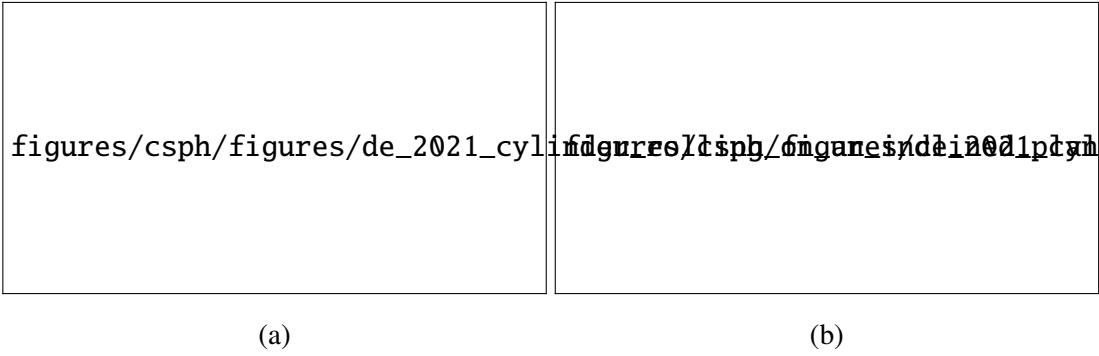
Figure 3.20: Snapshot of a rolling cylinder with the velocity vectors at two time steps for a friction coefficient of 0.6, corresponding to a stick case.

figures/csph/figures/de_2021_cylinder_rolling_on_an_inclined_plane/fr
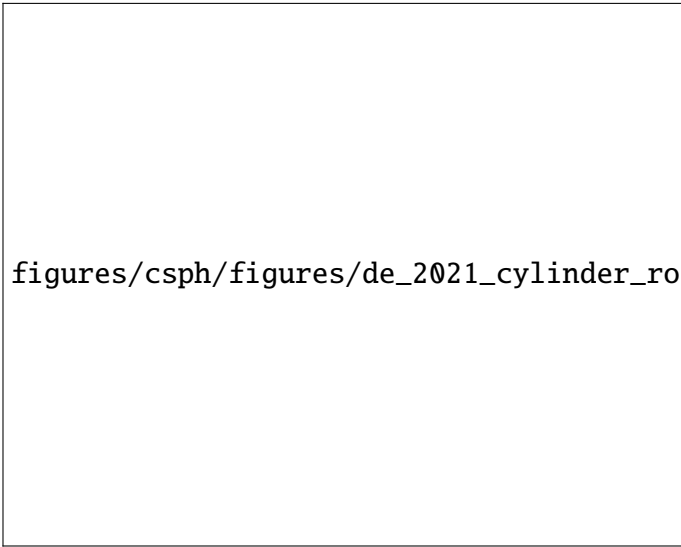
Figure 3.21: Time variation of the x-component of the center of mass of the circular cylinder for a friction coefficient of 0.3.

figures/csph/figures/de_2021_cylinder_rolling_on_an_inclined_plane

Figure 3.22: Time variation of the x-component of the center of mass of the circular cylinder for a friction coefficient of 0.6.

images/csph/images/vyas_2021_rebound_kinematics_3d/schematic.pdf
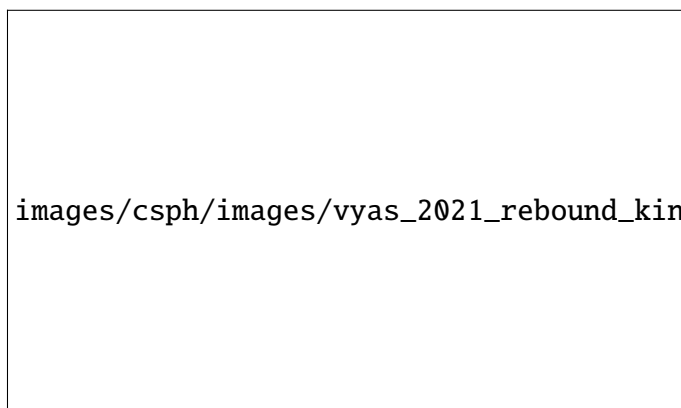
Figure 3.23: 3d rigid body rebound schematic

Quantity	Values
E, Young's modulus	10 MPa
v, Poisson's ratio	0.3975
ρ, density	1200 kg m^{-3}
μ, friction coefficient	0.3 & 0.6
Time of simulation	0.6 s
Resolution, δx	0.0025 m
Smoothing length factor, $h/\Delta x$	1.3
gravity $[g_x, g_y, g_z]$	$[g\,\sin(\theta), g\,\cos(\theta), 0.0]$
α, artificial viscosity	1
β, artificial viscosity	0
k_r, Normal stiffness coefficient	10^7
k_f, Tangential stiffness coefficient	10^5

Table 3.6: Numerical parameters and material properties for the rolling circular cylinder.

model description is shown in fig. 3.23. The sphere is assumed to be rigid and the material properties as well as the numerical parameters used are displayed in table 3.7. The sphere is impacted on the wall by varying the incident angles (θ_i) keeping the magnitude of the velocity constant, 5 m s^{-1}.

Quantity	Values
E, Young's modulus	70 GPa
v, Poisson's ratio	0.3
ρ, density	2650 kg m^{-3}
μ, friction coefficient	0.1
Time of simulation	0.25 ms
Resolution, δx	0.00153 m
Smoothing length factor, $h/\Delta x$	1.0
gravity $[g_x, g_y, g_z]$	$[0.0, -9.81, 0.0]$
k_r, Normal stiffness coefficient	10^7
k_f, Tangential stiffness coefficient	10^5

Table 3.7: Numerical parameters and material properties for sphere impacting a wall.

figures/csph/figures/vyas_2021_rebound_kinematics_3d/theta_vs_omeg
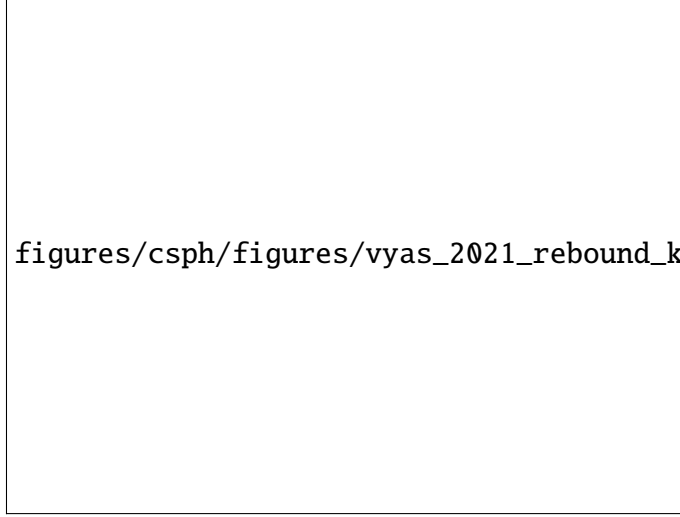
Figure 3.24: The plot of the variation of ω_r^* with θ_i^* of the impacting sphere simulated with the current numerical scheme, compared with the experimental result by Thornton *et al.* (2011).

Figure 3.24 depicts the variation of the non-dimensional angular velocity ω_r^* against the non-dimensional incident angle θ_i^*, where θ^* and ω_r^* are defined as

$$\theta_i^* = \frac{2\tan(\theta_i)}{(1+e_n)\mu}, \tag{3.37}$$

$$\omega_r^* = \frac{2R\omega_r}{(1+e_n)\mu V_{ni}}, \tag{3.38}$$

respectively. Here, ω_r corresponds to the z-component of the angular velocity vector. The simulated results are compared to the experimental results by Thornton *et al.* (2011). From the fig. 3.24, we can see that the current solver is able to replicate the original behavior to an acceptable approximation. We observe that the variation of the ω_r^* with θ_i^* to be linear with the current solver whereas the experimental result to be a nonlinear, this may be due to the usage of the linear force model in the current scheme.

3.4.8   Stress wave propagation in granular media

So far, we have modeled the collision between two bodies, in the current section, we study the collision among multiple bodies. The elastic wave propagation in a granular media is carried out, and whose experimental study was executed by Guilkey *et al.* (2001). To our knowledge this problem has not yet done in SPH literature yet. We consider five identical disks placed at an angle of 45 degrees, allowed to be impacted by a striker from right with a velocity 5.6 m s^{-1} in horizontal direction as depicted in fig. 3.25. Each granular disk has a radius of 50 mm, which are initially placed such that just touching. A particle

images/csph/images/de_2021_stress_wave_in_granular_material_part_2/schematic.pdf

Figure 3.25: Schematic of the initial placement of the frictional granular media including the impactor and walls

spacing of 1.25 mm is used, which results in 7830 particles per disk. The rigid box are modelled as rigid surfaces. The material parameters of the disc as well as the numerical parameters used in the numerical simulation are listed in table 3.8. Figure 3.26 shows the

Quantity	Values
K, Bulk modulus	102 GPa
G, Shear modulus	72 GPa
ρ, density	1900 kg m^{-3}
gravity $[g_x, g_y, g_z]$	[0.0, 0.0, 0.0]
k_r, Normal stiffness coefficient	1.75×10^{11}
k_f, Tangential stiffness coefficient	5×10^{10}
μ, Friction coefficient	0.5

Table 3.8: Material and numerical parameters used for the stress wave propagation problem.

particle plots of the granular discs with the stress fringes from the experiment (Guilkey *et al.*, 2001), and the simulation carried in the present study, and from the numerical study of de Vaucorbeil and Nguyen (2021), where the simulation is carried out using a total Lagrangian material point method (TLMPM). The snapshots of the current work are taken at time 0.2 ms, while the results of experimental and TLMPM result correspond to the time at 0.12 ms. This is due to the initial placement of the discs in the current work and the stress fringes being sensitive to initial placement. Here, the stress fringes in the

experimental work are evaluated using photo-elasticity. While, in the numerical work, the fringes are generated by plotting σ_f, computed as:

$$\sigma_f = 1 - \sin^2(f(\sigma_1 - \sigma_3)),$$ (3.39)

where f is a optical parameter which controls the fringe density, taken as $\pi/0.07\,\mathrm{G\,Pa}^{-1}$. The difference in the in-plane principal stress is computed using,

$$\sigma_1 - \sigma_3 = 2R = \sqrt{4\tau_{xy}^2 + (\sigma_x - \sigma_y)^2}$$ (3.40)

 From the qualitative comparison of the stress fringes in the granular discs of the current scheme with the experimental as well as the numerical result of TLMPM, the current scheme fringes are smooth and are similar to the experimental result.

3.4.9   Primary secondary analysis

In the current section we have studied the dependence of the behaviour of current contact force model on the variation of different bodies being primary. We have considered the following examples:

- Collision between symmetric bodies

- Circular cylinder rolling down an inclined plane

- Square solid sliding down an inclined plane

- Impact of a 3D sphere against a target wall.

Figure 3.27 depicts the variation of velocity or position of the elastic bodies involved in above cases. From fig. 3.27 we can see that the velocities of the elastic solids in a symmetric collision are invariant to the primary body chosen. While, considering the wall as primary in rolling cylinder, and sliding solid case, the error is more compared to the body being taken as primary. And in the case of granular particle impacting a wall, the angular velocity of the granular particle deviates from the experimental result when the wall being the primary body. With these results, we conclude that body with more curvature is advised to take as primary.

3.5   Conclusions

In this paper we have demonstrated a simple approach to effectively handle the collision between elastic solids modeled using an updated Lagrangian SPH model. A contact force

(a)

(b)

(c)

Figure 3.26: Stress fringes of the granular discs from (a) experiment (Guilkey *et al.*, 2001), (b) TLMPM (de Vaucorbeil and Nguyen, 2021) (c) Current work

(a) Collision between a flat interface solids.

(b) An elastic body sliding down an inclined plane

(c) A circular cylinder rolling on an inclined plane

(d) Variation of the angular velocity with respect to the incident theta.
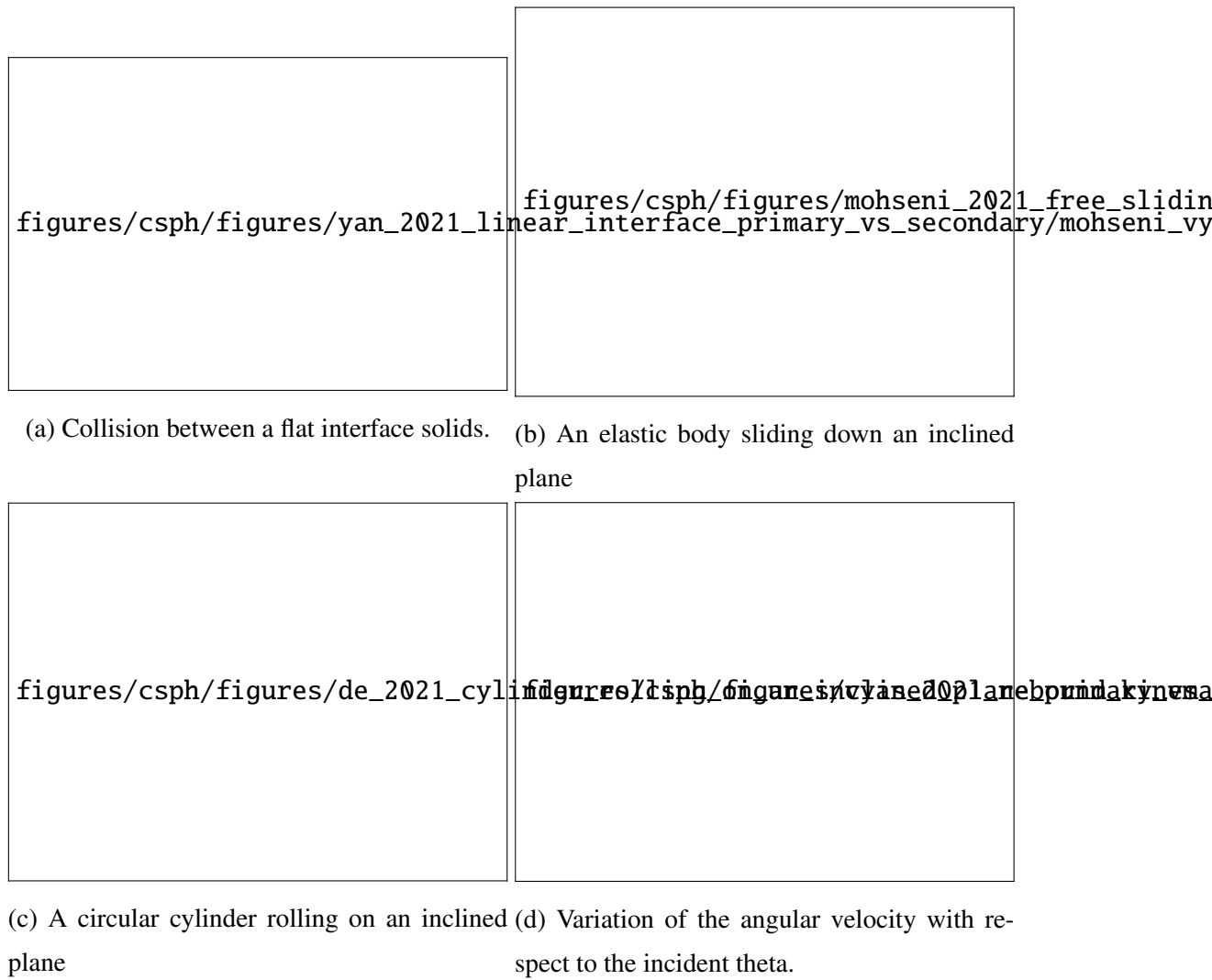
Figure 3.27

model is used to handle the collision between bodies. A surface aware spring based contact force is used to handle the collision between bodies. This effectively allows us to model collision and friction accurately. In addition this eliminates any spurious forces that are commonly seen with SPH when two bodies are nearby but not in actual contact. The contact force model utilized in the current work is sensitive towards the primary and the secondary body chosen. A careful analysis is carried out to understand which body is to be considered as primary among the colliding solids, and it is found that choosing the body with the highest curvature as the primary body gives the best results. Further, we have made our implementation open-source.

It has been demonstrated that the current model is able to predict the post collision behaviour of the colliding bodies by simulating collision between flat, and curved interfaces in two and three dimensions. A sliding elastic body is simulated to test the frictional part of the contact model. Finally, the full scale model is applied to model the stress propagation in granular discs for the first time in SPH. The results compare well with those of FEM as well as analytical studies.

A non-linear contact force model can be implemented in the future work. The current work can be easily extended to the modeling of collision between elastic and elastic-plastic bodies. Also, the collision between the bodies undergoing breakage can be easily captured with the current framework.

Till now, we have a Lagrangian solver without any problems, with good particle homogenization and a higher Poisson ratio; in the current chapter, we have incorporated a contact force model to handle the collision between arbitrarily shaped elastic solids. This eliminates the spurious interaction between the bodies moving close but not touching and includes friction. This chapter's work in handling collision is extended to the rigid-elastic and rigid-plastic contacts in the next few chapters. We have modeled the elastic phase, fluid phase, and the collision between the impacting solids in our aim of handling abrasive water jet machining. In the next chapter, we will model the interaction between the fluid and the elastic structure, fluid-structure interaction, as this is seen when the water from the inlet impacts the target. We will propose an updated Lagrangian solver by coupling the solver developed in chapter 2 and handling fluid-structure interaction.

Chapter 4

Fluid structure interaction

4.1 Introduction

Till now we have developed solvers to model the fluid and elastic dynamics. With in the abrasive water jet machining, the interaction between the fluid and the rigid or elastic part is remained. In the current chapter we utilize the CTVF scheme developed in chapter 2 for fluid and elastic dynamics is coupled to handle the fluid structure interaction in the current chapter. Problems with free surface and analytical solution are used to validate.

Fluid-structure interaction (FSI) is a common engineering problem that is seen in daily life. Some examples include the deformation of the wind turbine blade due to the fluid flow, the flow traversal due to the deflected blade, blood flow in heart value, coastal engineering, and vortex-induced vibration (Williamson *et al.*, 2004; Bearman, 2011). An accurate study of FSI can allow us to optimize the systems where FSI is dominant. However, studying the FSI phenomena through experiments or analytical techniques is complex due to its nonlinear behavior.

Handling FSI problems with the transport velocity formulation framework is advantageous as it can solve the tensile instability issue in solid dynamics and inhomogeneous particle distribution in fluids. In the current chapter, we handle FSI problems by the CTVF method, where both fluids and solid phases are modeled using CTVF alone. To validate the proposed method, we consider three numerical test cases. A uniformly distributed load over a clamped beam (UDL) problem is considered to validate the elastic dynamics of CTVF. An aluminum plate over a hydrostatic tank for FSI validation is considered. Finally, it is applied to a fluid flow hitting an elastic plate. Here, the deformation of the elastic plate is compared against the experimental results. A convergence analysis is undertaken for both UDL and elastic deformation under hydrodynamic load problems. All the results are fully automated with the automan package (Ramachandran, 2018b) and

made hundred percent reproducible. The source code for all the problems demonstrated in this manuscript is made available at `https://github.com/dineshadepu/fsi_etvf`.

4.2   Methodology

We follow CTVF formulation to model the fluid and solid phase. Following CTVF, the particles are moved with a transport velocity rather than the momentum velocity, with which we get a homogenized particle distribution as well as it eliminates the tensile instability. In the next two sections we show the discretized equations of both fluid and solid phase. Please see (Adepu and Ramachandran, 2021) for more details.

4.2.1   Discrete equations of the fluid medium

The governing equations of the fluid are conservation of mass and momentum. Following the weakly compressible SPH scheme, we use an equation of state to complete the system. The SPH discretization of the continuity equation (5.27) and the EDAC based PRKP:edac-sph-iccm2015 pressure evolution equation (5.31) respectively are,

$$\frac{\tilde{d}\rho_a}{dt} = \sum_b \frac{m_b}{\rho_b} \left(\rho_a \, \tilde{\mathbf{u}}_{ab} \; + \; (\rho \, (\tilde{\mathbf{u}} \; - \; \mathbf{u}))_{ab} \right) \cdot \nabla_a W_{ab}, \tag{4.1}$$

$$\frac{\tilde{d}p_a}{dt} = \sum_b \frac{m_b}{\rho_b} \left((p_a - \rho_a c_s^2) \, \mathbf{u}_{ab} \; + \; p_a \, \tilde{\mathbf{u}}_{ab} \; - \; (p \, (\tilde{\mathbf{u}} - \mathbf{u}))_{ab} \; + \right.$$
$$\left. 4 \, \nu_{edac} \frac{p_a - p_b}{(\rho_a + \rho_b)(r_{ab}^2 + 0.01 h_{ab}^2)} \mathbf{r}_{ab} \right) \cdot \nabla_a W_{ab}. \tag{4.2}$$

Where $\frac{\tilde{d}}{dt}$ is the material derivative, with $\tilde{u}$ being the transport velocity of the particles, $\mathbf{u}_{ab} = \mathbf{u}_a - \mathbf{u}_b$. Similarly, the discretized momentum equation for fluids is written as,

$$\frac{\tilde{d}\mathbf{u}_a}{dt} = - \sum_b m_b \left[\left(\frac{p_a}{\rho_a^2} + \frac{p_b}{\rho_b^2} \right) \mathbf{I} - \left(\frac{\mathbf{A}_a}{\rho_a^2} + \frac{\mathbf{A}_b}{\rho_b^2} + \Pi_{ab} \mathbf{I} \right) \right] \cdot \nabla_a W_{ab}$$
$$+ \mathbf{u}_a \sum_b \frac{m_b}{\rho_b} \, \tilde{\mathbf{u}}_{ab} \cdot \nabla_a W_{ab}$$
$$+ \sum_b m_b \frac{4\eta \nabla W_{ab} \cdot \mathbf{r}_{ab}}{(\rho_a + \rho_b)(r_{ab}^2 + 0.01 h_{ab}^2)} \mathbf{u}_{ab} + \mathbf{g}_a + \frac{\mathbf{F}_{\text{FSI}}^a}{m_a} \tag{4.3}$$

where $\mathbf{A}_a = \rho_a \mathbf{u}_a \otimes (\tilde{\mathbf{u}}_a - \mathbf{u}_a)$, $\mathbf{I}$ is the identity matrix, η is the kinematic viscosity of the fluid and (Morris *et al.*, 1997b) formulation is used to discretize the viscosity term. Π_{ab} is the artificial viscosity (Monaghan, 2005a) to maintain the stability of the numerical

scheme. It is given as,

$$\Pi_{ab} = \begin{cases} \dfrac{-\alpha h_{ab} \bar{c}_{ab} \phi_{ab}}{\bar{\rho}_{ab}} & \mathbf{u}_{ab} \cdot \mathbf{r}_{ab} < 0, \\ 0 & \mathbf{u}_{ab} \cdot \mathbf{r}_{ab} \geq 0, \end{cases} \tag{4.4}$$

where,

$$\phi_{ab} = \frac{\mathbf{u}_{ab} \cdot \mathbf{r}_{ab}}{r_{ab}^2 + 0.01 h_{ab}^2}, \tag{4.5}$$

where, $\mathbf{r}_{ab} = \mathbf{r}_a - \mathbf{r}_b$, $h_{ab} = (h_a + h_b)/2$, $\bar{\rho}_{ab} = (\rho_a + \rho_b)/2$, $\bar{c}_{ab} = (c_a + c_b)/2$, and α is the artificial viscosity parameter. $\mathbf{F}_{\mathrm{FSI}}^a$ is the force due to the interaction with elastic structure. This force modeling is explained in section 4.2.4. We utilize the ghost particle approach proposed in (Adami *et al.*, 2012) to handle the boundaries.

4.2.2   Solid phase modeling

Similar to discretized fluid governing equation, the elastic structure equations are (5.27), and the momentum equation,

$$\frac{\tilde{d}\mathbf{u}_a}{dt} = -\sum_b m_b \left[\left(\frac{p_a}{\rho_a^2} + \frac{p_b}{\rho_b^2} \right) \mathbf{I} - \left(\frac{\boldsymbol{\sigma}_a'}{\rho_a^2} + \frac{\boldsymbol{\sigma}_b'}{\rho_b^2} + \Pi_{ab}\mathbf{I} \right) \right] \cdot \nabla_a W_{ab}$$

$$+ \mathbf{g}_a + \frac{\mathbf{F}_{\mathrm{FSI}}^a}{m_a}, \quad (4.6)$$

while the additional stress terms, $\mathbf{A}$ in momentum equation of solid mechanics are not considered as it has a negligible effect. An equation of state is utilized to link the pressure with density following a weakly compressible SPH scheme. Jaumann stress rate equation is solved to evolve the shear stress, given as,

$$\frac{\tilde{d}\boldsymbol{\sigma}_a'}{dt} \qquad = \qquad 2G(\dot{\boldsymbol{\epsilon}}_a \qquad - \qquad \frac{1}{3}\dot{\boldsymbol{\epsilon}}_a\mathbf{I}) \qquad + \qquad \boldsymbol{\sigma}_a'\boldsymbol{\Omega}_a^T \qquad + \qquad \boldsymbol{\Omega}_a\boldsymbol{\sigma}_a' \tag{4.7}$$

The SPH discretization of the gradient of velocity is given as,

$$\nabla \mathbf{u}_a = -\sum_b \frac{m_b}{\rho_b} (\mathbf{u}_a - \mathbf{u}_b) \otimes (\nabla_a W_{ab}), \tag{4.8}$$

where $\otimes$ is the outer product. With the strain and rotation tensors as,

$$\dot{\epsilon}_{ij} = \frac{1}{2} \left(\frac{\partial u_i}{\partial x_j} + \frac{\partial u_j}{\partial x_i} \right), \tag{4.9}$$

and Ω_{ij} is the rotation tensor,

$$\Omega_{ij} = \frac{1}{2} \left(\frac{\partial u_i}{\partial x_j} - \frac{\partial u_j}{\partial x_i} \right). \tag{4.10}$$

4.2.3   Transport velocity computation

The particles in the current scheme are moved with the transport velocity,

$$\frac{d\mathbf{r}_a}{dt} = \tilde{\mathbf{u}}_a. \tag{4.11}$$

The transport velocity is updated using,

$$\tilde{\mathbf{u}}_a(t + \Delta t) = \mathbf{u}_a(t) + \Delta t \frac{\tilde{d}\mathbf{u}_a}{dt} + \left(\frac{d\mathbf{u}_a}{dt}\right)_{\text{c}} \Delta t \tag{4.12}$$

Where $\left(\frac{d\mathbf{u}_a}{dt}\right)_{\text{c}}$ is the homogenization acceleration which ensures that the particle positions are homogeneous. In the current work we have used Sun's (Sun *et al.*, 2019a) PST to homogenization the fluid medium while iterative PST (IPST)(Huang *et al.*, 2019) for the solid phase. According to (Adepu and Ramachandran, 2021) the force formulation of (Sun *et al.*, 2019a) is,

$$\left(\frac{d\mathbf{u}_a}{dt}\right)_{\text{c}} = -\frac{\text{M} \, (2h)c_0}{\Delta t} \sum_b \left[1 + R\left(\frac{W_{ab}}{W(\Delta x)}\right)^n\right] \nabla_a W_{ab} V_b, \tag{4.13}$$

where R is an adjustment factor to handle the tensile instability, and M is the mach number of the flow. V_b is the volume of the bth particle, c_0 is the speed of sound. The acceleration is modified to account for particles on the free surface. Here, $R = 0.2$ and $n = 4$ are used. Please see (Adepu and Ramachandran, 2021) for detailed explanation of PST.

4.2.4   Fluid-structure interaction

Coupling is handled in a straight forward way in SPH. While modelling the fluid phase and treating the fluid-structure interactions, the structure particles are assumed to be boundary particles. From the boundary handling given in Adami (Adami *et al.*, 2012), we compute the pressure of the boundary particles from the extrapolated equation as,

$$p_s = \frac{\Sigma_f p_f W_{sf} + (\mathbf{g} - \mathbf{a_s}) \cdot \Sigma_f \rho_f \mathbf{r}_{sf} W_{sf}}{\Sigma_f W_{sf}}. \tag{4.14}$$

Here, $\mathbf{a}_s$ is the acceleration of the structure particles. The subscript f denotes the fluid particles and s denotes the structure particles. By the extrapolated pressure, hydrodynamic density of structure properties are computed. Please note that the pressure we set here are only pertaining to the FSI force and does not correspond to the real pressure or density of the structure particles. By utilizing the previously set hydrodynamic properties on the structure, the interaction force is computed using,

$$\mathbf{F}^i_{\text{FSI}} = -m_i \sum_a m_a \left(\frac{p_i}{\rho_i^2} + \frac{p_a}{\rho_a^2} + \Pi_{ia}\right) \nabla_i W(x_{ia}) \tag{4.15}$$

where i is fluid particle, a is structure particle.
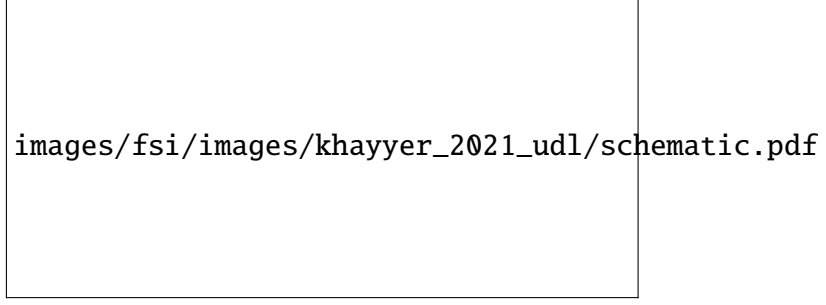
Figure 4.1: The schematic of a clamped elastic beam being acted upon by a uniformly distributed load.

4.3   Results And Discussion

4.3.1   Uniformly distributed loading (UDL) on a clamped beam

In the first test case, we validate the structural part of the current solver. We chose a homogeneous elastic plate clamped on both ends acted upon by a uniformly distributed load ($q = 20$ Nm^{-1}) as shown in fig. 4.1. The beam's length (L) and height (H) is 0.2 m and 0.012 m, respectively. The mechanical properties of the plate are set as $E = 10^7$ Pa in Young's modulus, $v = 0$ in Poisson's ratio and $\rho = 1000$ kgm^{-3}) in density. The numerical solution of the y-displacement at the center of the beam is compared against the analytical counterpart. The analytical solution for the deflection of a uniformly distributed beam clamped at both ends is given by

$$\eta\left(\frac{L}{2}\right) = \frac{qL^4}{384D}, \tag{4.16}$$

where, D is defined as $\frac{Eh^3}{12(1-(v)^2)}$. We consider three particle resolutions such that, 10, 15, and 20 particles along the beam's width are used. We run for a total physical time of 2 seconds.

Figure 4.2 depicts the time history of y-displacement of the beam center for different particle resolutions computed using the current solver compared against the analytical solution. From fig. 4.2, we can see that the current solver can accurately predict the displacement of the clamped beam. Convergence of the current scheme is captured in fig. 4.2, and the computational results are within a reasonable variation of the analytical solution with the variation of the particle spacing.

4.3.2   Hydrostatic water column on an elastic plate

In this example we study the deformation of an elastic plate due to the hydrostatic water column. We utilise the current example to examine the accuracy and convergence

figures/fsi/figures/khayyer_2021_udl/homogenous.pdf
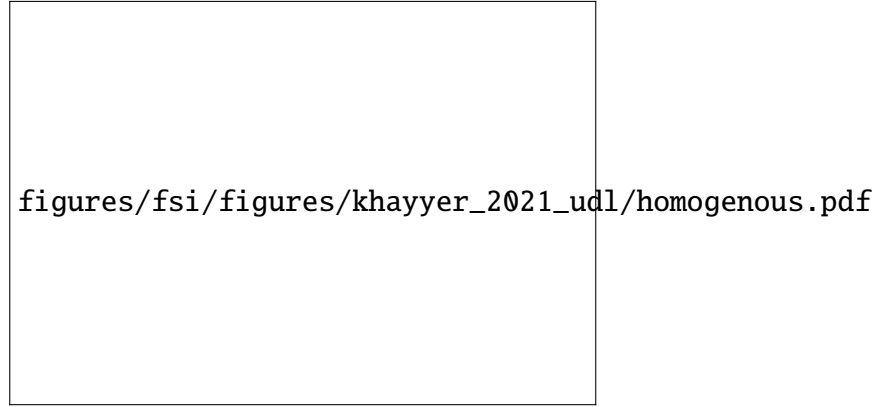
Figure 4.2: Time variation of the y-displacement of the center of the beam for three different resolutions, compared against the analytical result.

images/fsi/images/ng_2020_hydrostatic_water_column_on_elastic_plate/
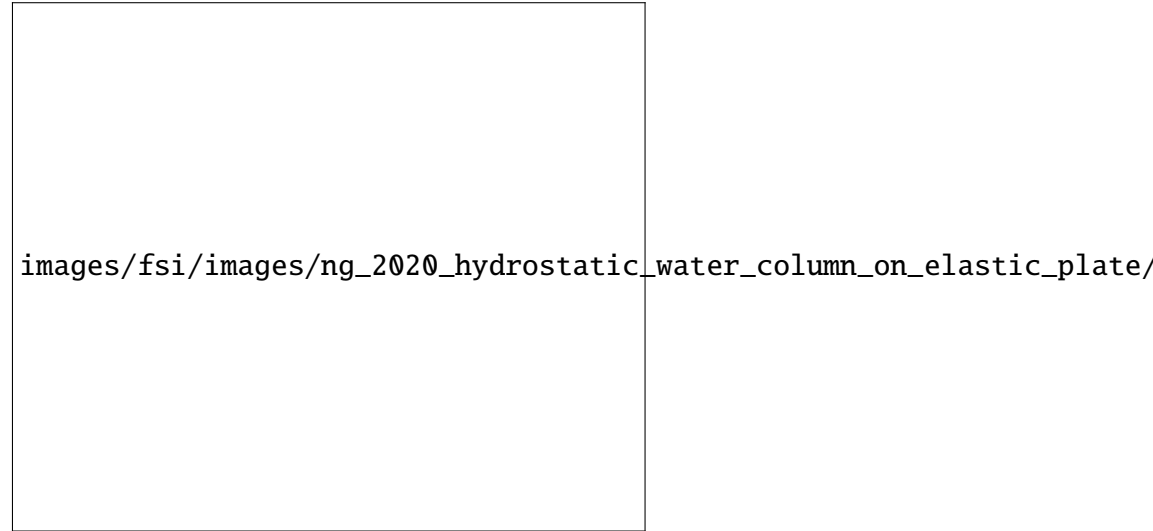
Figure 4.3: Schematic of the hydrostatic water column on an elastic plate. Fluid particle color represents pressure.

of the current solver. The schematic of fluid with the elastic beam is shown in fig. 4.3 along with the initial pressure distribution in the fluid. The figure includes the dimensions as well. The material properties of the beam are, a density of 2700 kgm^{-3}, with an Young's modulus of 67.5 GPa, and a Poisson ratio of 0.34. The material properties of the fluid are, a density of 1000 kgm^{-3}, with a dynamic viscosity of 0 kgm^{-1}s^{-1}. We consider two particle resolutions such that we get 10, 15 and 20 particles along the width directing of the beam. We run the simulation for a total physical time of 3 seconds. The y-displacement at the center of the beam is compared against the analytical with the current numerical solver for quantitative validation. Here, the beam deflection computed using an analytical expression results in a deflection $d = -6.85 \times 10^{-5}$ m.

Figure 4.4 shows the particle plot of the fluid along with the elastic solid at time 2 seconds with color of the fluid particles describing the pressure. This snapshot corresponds to the highest particle resolution i.e., 20 particles along the width direction. From the fig. 4.4, we can see that the current solver produces a smooth pressure distribution

figures/fsi/figures/ng_2020_hydrostatic_water_column/figures/fsi/figures/ng_2020_hydro/
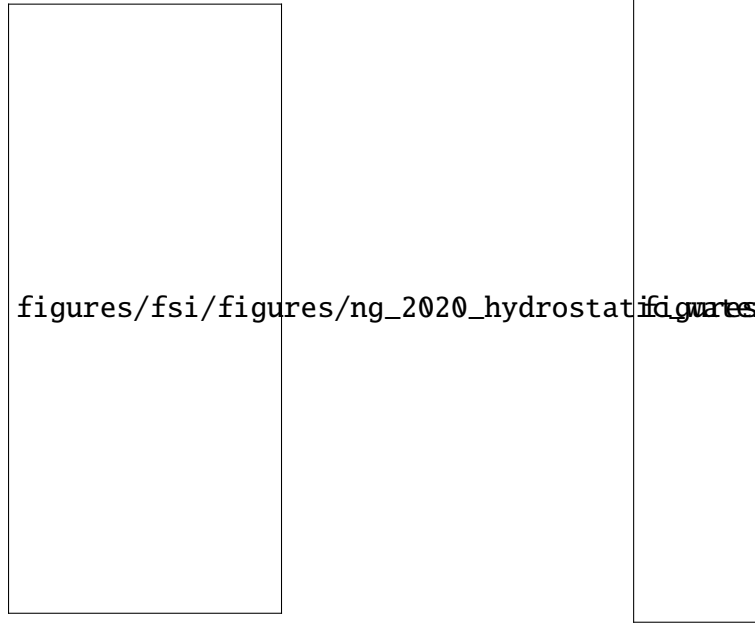
Figure 4.4: Snapshot of the fluid and the elastic structure at time 0.5 sec including the pressure of the fluid.

demonstrating the stability of the current solver. Figure 4.5 depicts the time history of y-displacement of the beam center for different particle resolutions computed using the current solver compared against the analytical solution. From fig. 4.5 we can see that the current solver is able to predict the displacement of the clamped beam within the vicinity of the analytical results. Also as the particle spacing is reduced, the beam displacement is converging as well.

4.3.3   Water impact onto an elastic plate

In this case, we study the deformation of the elastic plate due to the impact of a dam breaking flow. Figure 4.6 shows the initial positions of fluid and the structure inside the dam, including the dimensions. Following (Sun *et al.*, 2019b) we set the material properties of the elastic plate, a density of 2500 kgm^{-3}, with an Young's modulus of 10^6 Pa, and a Poisson ratio of 0. The material properties of the fluid are, a density of 1000 kgm^{-3}, with a dynamic viscosity of 0 kgm^{-1}s^{-1}. A particle spacing of 5×10^{-4} m is taken, resulting in a total of 182911 particles, which includes fluid, structure and solid wall. We run a total physical time of 0.7 seconds. Here the fluid is initially released which attains

figures/fsi/figures/ng_2020_hydrostatic_water_column_on_elastic_pl
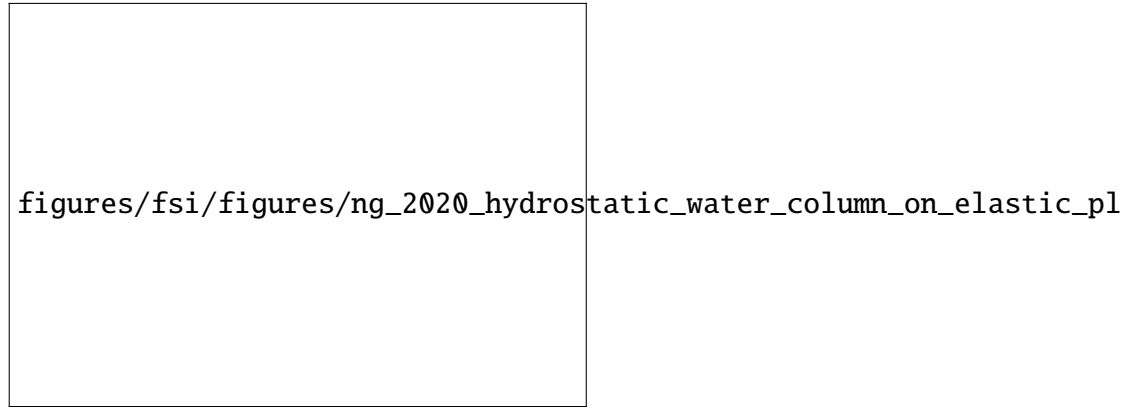
Figure 4.5: The mid-span deflection of the structure under hydrodynamic loading with time for different resolutions, compared against the analytical and the numerical result of (Ng *et al.*, 2020)

images/fsi/images/sun_2019_dam_breaking_flow_impacting_an_elastic_p
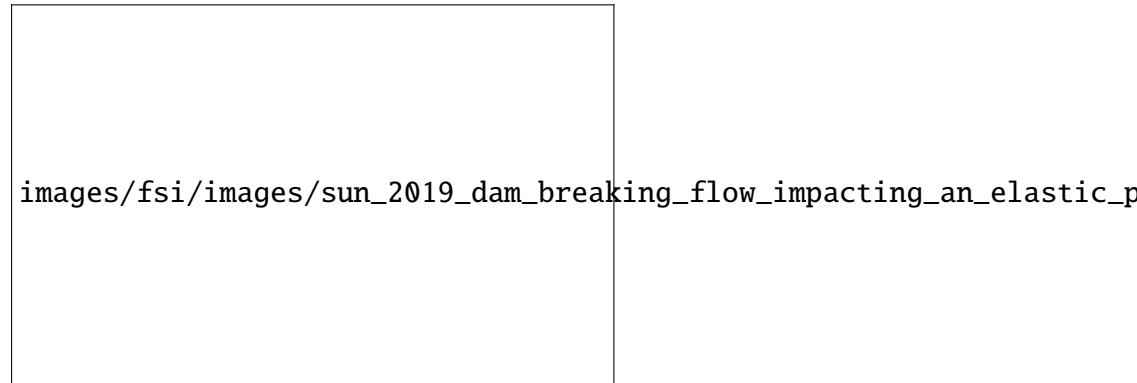
Figure 4.6: Schematic of the dam-break flow impacting an elastic plate. All dimensions are in meters.

a certain velocity by the time it impacts the structure. The structure will obstruct the fluid making it rise and the fluid will deform the elastic plate. The fluid will rise and hit the other end of the dam, following it comes back and hits the structure from the back. For a quantitative validation, we compare the current solver results to the other numerical techniques.

The time variation of the x-displacement of the elastic structure is compared against other numerical results (Sun *et al.*, 2019b; Bogaers *et al.*, 2016). From the fig. 4.7 we can see that the displacement computed by the current solver is with in a vicinity of the other results produced. Figure 4.8 shows the snapshots of the fluid and the elastic structure at different time instances. From fig. 4.8, we can see that the fluid after hitting the structure rises and hits the other end of the tank and travels back to hit the structure again.
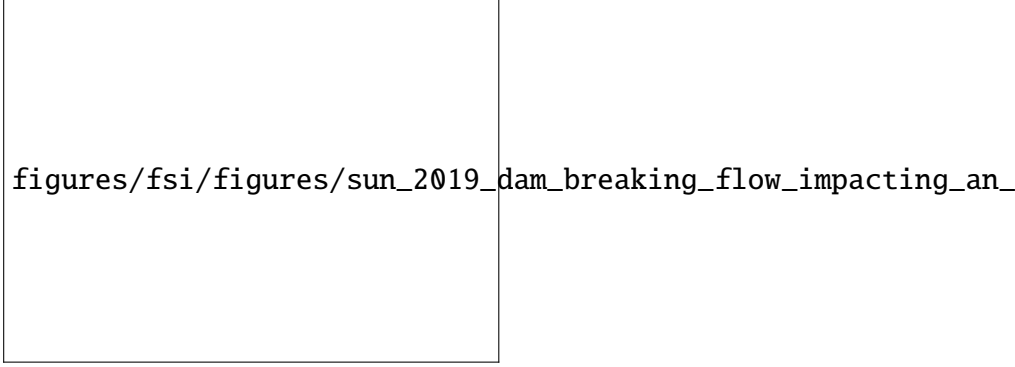
Figure 4.7: Time histories of horizontal displacement of the free end of the elastic structure compared against the numerical results of (Sun *et al.*, 2019b; Bogaers *et al.*, 2016)-Water impact onto an elastic plate.

4.4   Summary

CTVF is able to eliminate several issues SPH faces while solving fluid and solid problems. Through particle shifting techniques and incorporating the missing terms, CTVF can produce better approximations in simulating fluid problems. Similarly, elimination of tensile instability while solving elastic dynamics problems is done with CTVF. With these advantages, we solved both fluid and solid phases with CTVF while handling the FSI problems.

We validated the current schemes by solving a UDL problem to test the structure equations, and an aluminum plate over a hydrostatic tank where an analytical solution is available is utilized to validate the FSI part of the current solver. The current solver is applied to the wavefront arising due to a dam break hitting an elastic plate. Here, the deformation of the elastic plate is compared to the experimental results. A convergence analysis is undertaken for both fundamental benchmarks, UDL, and hydrostatic tank.

In the current chapter we have handled the fluid structure interaction using the CTVF scheme. With fluid, elastic, contact modeling, and rigid fluid coupling, FSI is one essential multiphysics problem to be modeled to handle abrasive water jet machining. One of the physics needed to model to handle the water jet machining. Leaving us with rigid fluid coupling and solid body erosion. In the next chapter we will handle the rigid fluid coupling as it allows us to study coupled behaviour of fluid and rigid body together.

figures/fsi/figures/sun_2019_dam_breaking_flow_impacting_an_elast

figures/fsi/figures/sun_2019_dam_breaking_flow_impacting_an_elast

figures/fsi/figures/sun_2019_dam_breaking_flow_impacting_an_elast

figures/fsi/figures/sun_2019_dam_breaking_flow_impacting_an_elast

figures/fsi/figures/sun_2019_dam_breaking_flow_impacting_an_elast
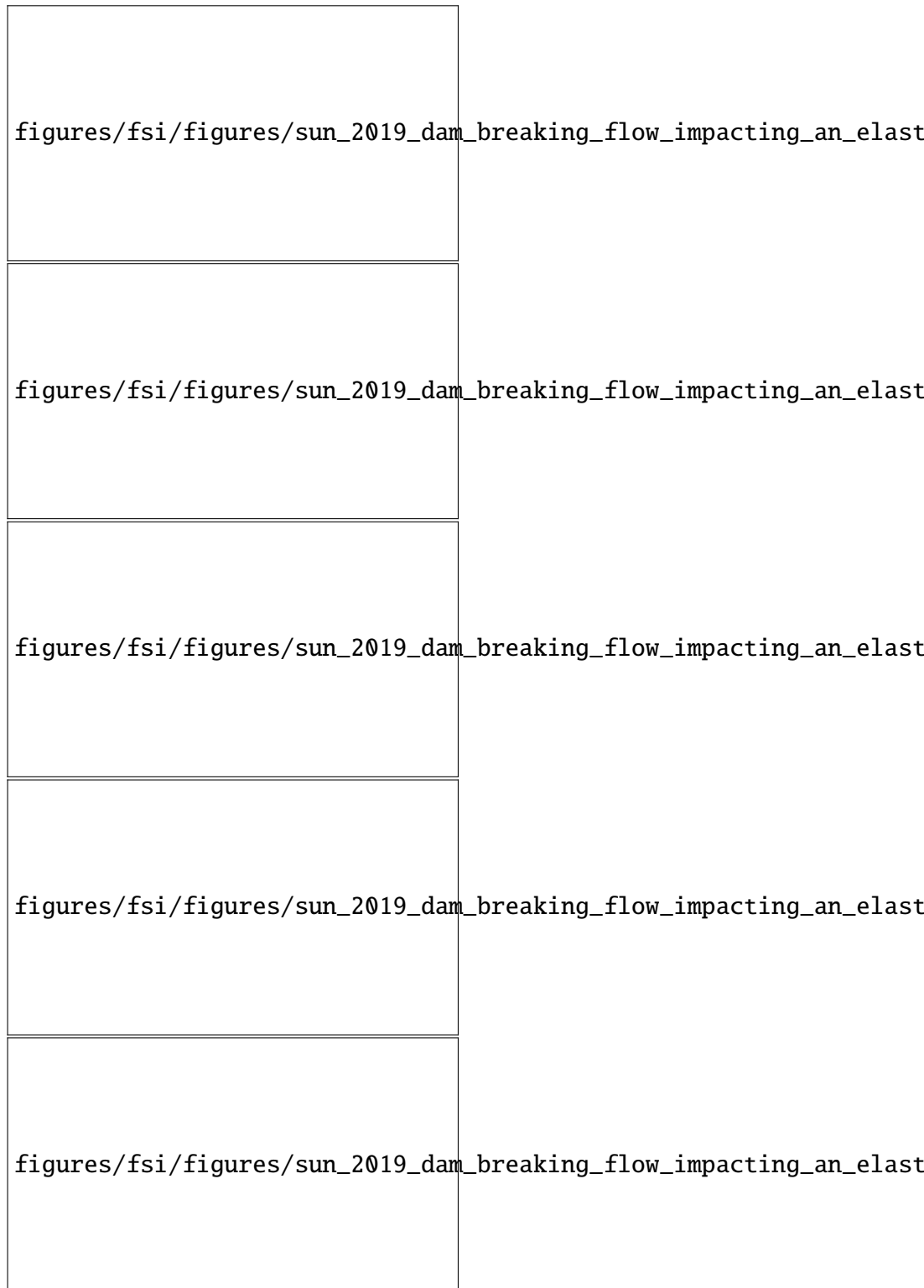
Figure 4.8: Snapshot of the fluid and the structure at different time stamps.

Chapter 5

Rigid fluid coupling

5.1 Introduction

In the current chapter, we model the dynamics of rigid bodies in fluid flow and the coupled behavior of fluid and rigid bodies. As part of AWJM, the behavior of the abrasive particles in the fluid jet can be modeled by studying the rigid-fluid coupling phenomenon.

Transport of arbitrarily shaped rigid bodies in fluid flows is a common phenomenon that occurs widely in nature. Bodies transport in internal systems (Dai *et al.*, 2021), debris flow (Qingyun *et al.*, 2022), the food processing industry (Karunasena *et al.*, 2014), and ice-sea modeling (Mintu and Molyneux, 2018) are a few areas to mention. The two-way coupling between the rigid and the fluid flow is nonlinear, and a numerical study is chosen due to its flexibility in modeling the physics accurately. Numerically rigid fluid coupling (RFC) can be studied with mesh-based, or meshless techniques can be utilized.

In the current chapter, we couple CTVF with MDEM to handle the rigid fluid coupling problems. The fluid phase is modeled using a corrected transport velocity formulation developed by (Adepu and Ramachandran, 2021). CTVF provides smooth pressure distribution with EDAC formulation and homogeneous particle distribution, resulting in accurate fluid modeling. Rigid-rigid interactions are modeled with MDEM and is applied to 3D problems. A damping term is introduced into the contact force model to account for the energy loss during the collision. The interaction between the fluid phase and rigid bodies is handled using the dummy particle approach (Adami *et al.*, 2012). Numerical examples were simulated to validate the resulting RFC model, including the water entry of a cube, a circular body, and two circular bodies in series in a hydrostatic tank. Rigid-rigid interaction solver is validated using 2D and 3D reference test cases with analytical and experimental solutions available. A freely and controlled sliding body, a rolling cylinder, and the collapse of a stack of cylinders under gravity are simulated. The

proposed MDEM-CTVF model has been found satisfactory in modeling rigid-fluid coupling simulations with acceptable accuracy and performance. All the results are fully automated with the automan package (Ramachandran, 2018b) and made hundred percent reproducible. The source code for all the problems demonstrated in this manuscript is made available at `https://github.com/dineshadepu/rfc`.

5.2 Rigid body dynamics

The equations governing the dynamics of a rigid body are, balance of linear and angular momentum given by,

$$\frac{d\,(M\mathbf{v}_{cm})}{dt} = \sum_i \mathbf{F}_i, \tag{5.1}$$

$$\frac{d\mathbf{L}}{dt} = \boldsymbol{\tau}_{cm}, \tag{5.2}$$

where M, $\mathbf{v}_{cm}$ are the mass and velocity of the rigid body. $\mathbf{F}_i, \boldsymbol{\tau}_{cm}, \mathbf{L}$ are force acting at point i, torque and angular momentum about the center of mass of the rigid body. In the current case, force acting on the particle i ($\mathbf{F}_i$) is due to the interaction with the other bodies and with the fluid particles, and any other body forces. The torque ($\boldsymbol{\tau}_{cm}$) and angular momentum ($\mathbf{L}$) are computed as,

$$\boldsymbol{\tau}_{cm} = \sum_i \mathbf{F}_i \times (\mathbf{x}_{cm} - \mathbf{x}_i), \tag{5.3}$$

$$\boldsymbol{L} = \sum_i \mathbf{r}_i \times (\boldsymbol{\omega} \times \mathbf{r}_i) = \sum_i m_i \left[(\mathbf{r}_i \cdot \mathbf{r}_i)\mathbf{I} - \mathbf{r}_i \otimes \mathbf{r}_i \right]. \tag{5.4}$$

Here $\mathbf{x}_{cm}$ and ω are the position of the center of mass and angular velocity of the rigid body. m_i, $\mathbf{x}_i$, $\mathbf{r}_i$ are the mass, position of particle, and vector from center of mass to the particle i.

Figure 5.1: Body frame and local frame description of rigid body

We use two coordinate frames to capture the dynamics of the rigid body, a global frame and a body frame as shown in fig. 5.1. The body fixed frame, which moves with rigid body is located always at the center of mass ($\mathbf{x}_{cm}$). The state of the rigid body at a given time (t) can be described using position ($\mathbf{x}_{cm}$) and velocity ($\mathbf{v}_{cm}$) of the center of mass, a rotation matrix($\mathbf{R}$) to represent the orientation of the rigid body with respect to the global frame, and angular velocity(ω). The center of mass is computed with

$$\mathbf{x}_{cm} = \frac{\sum_i m_i \, \mathbf{x}_i}{\sum_i m_i} \tag{5.5}$$

The position of the discretized particle (i) in fig. 5.1 belonging to the rigid body at time t can be computed ,

$$\mathbf{x}_i = \mathbf{x}_{cm} + \mathbf{r}_i, \tag{5.6}$$

with

$$\mathbf{r}_i = \mathbf{R} \cdot \bar{\mathbf{r}}_i. \tag{5.7}$$

Here $\bar{\mathbf{r}}_i$ is the position of the particle i about the body frame axis and remains constant through out the simulation. The rotation matrix $\mathbf{R}$ is used to bring the body frame position vector to the global frame $\mathbf{O}$. Similarly the velocity vector is computed as,

$$\mathbf{v}_i = \mathbf{v}_{cm} + \omega \times \mathbf{r}_i. \tag{5.8}$$

We evolve the state of the rigid body through the integration of the eqs. (6.14) and (6.15). The linear velocity of the center of mass ($\mathbf{v}_{cm}$) and angular momentum ($\mathbf{L}$) at the next timestep are computed as,

$$\mathbf{v}_{cm}^{n+1} = \mathbf{v}_{cm}^{n} + \frac{\mathbf{F}_{cm}}{M} \, \Delta t, \tag{5.9}$$

$$\mathbf{L}^{n+1} = \mathbf{L}^{n} + \tau_{cm} \, \Delta t. \tag{5.10}$$

The position of the center of mass and orientation ($\mathbf{R}$) are updated by,

$$\mathbf{x}_{cm}^{n+1} = \mathbf{x}_{cm}^{n} + \mathbf{v}_{cm}^{n} \, \Delta t, \mathbf{R}^{n+1} = \mathbf{R}^{n} + \tilde{\omega}^{n} \, \mathbf{R}^{n} \, \Delta t, \tag{5.11}$$

where $\tilde{\omega}^{n}$ is matrix formulation of angular velocity ω. The angular velocity at the new time step is computed with

$$\omega^{n+1} = (\mathbf{I}^{-1})^{n+1} \, \mathbf{L}^{n+1}. \tag{5.12}$$

Here, moment of inertia at the new time step is computed as,

$$(\mathbf{I}^{-1})^{n+1} = \mathbf{R}^{n+1} \bar{\mathbf{I}}^{-1} (\mathbf{R}^{n+1})^{T}. \tag{5.13}$$

where moment of inertia ($\overline{\boldsymbol{I}}^{-1}$) in body frame is used to compute in global frame at every time instant for faster computations. The position and velocity of the particles of the rigid body are updated by

$$\mathbf{r}_i = \mathbf{R} \cdot \overline{\mathbf{r}}_i, \tag{5.14}$$

$$\mathbf{x}_i = \mathbf{x}_{cm} + \mathbf{r}_i, \tag{5.15}$$

$$\mathbf{v}_i = \mathbf{v}_{cm} + \omega \times \mathbf{r}_i. \tag{5.16}$$

5.2.1   Contact algorithm

Figure 5.2: Contact force description

To handle the contact we mark the bodies under contact as primary and secondary. Each body is discretized into equispaced points, each having mass equivalent to their density times the volume spanned by the spacing. The force on each particle is computed due to the interaction with the other body. The force is computed on the primary body particles due to the interaction with the secondary body and an equal and opposite force is transferred to the closest particle on the secondary body. The force acting on particle i due to the interaction with body B, can be resolved into a normal and tangential part. Here, we utilize Mohseni-Mofidi *et al.* (2021) to compute these forces. Rather than computing the force on particle i due to each individual particle j, we consider the force due to the full body B, with which we are able to consider the shape of the body, and not computing the force by assuming the body's shape at the interaction as being spherical. In traditional DEM, to compute the force on particle i, we compute the overlap of particle i with each and every particle j of body B, where both particle i and j are assumed to be spherical in shape. This leads to inaccurate modeling of contact when the bodies in interaction are

not spherical in shape. We request the reader to see Mohseni-Mofidi *et al.* (2021), and (Adepu and Ramachandran, 2022) for clear description.

The contact force is resolved into a normal and tagential part. The normal force is used to eliminate the two bodies to penetrate, while the tangential part for friction modeling. The normal force $\mathbf{F}_i$ due to the interaction with body B is computed as,

$$\mathbf{F}_i = K_r \delta_n^i \mathbf{n}_i. \tag{5.17}$$

Here, to compute the overlap δ_n^i, the distance (d_i) of particle i from the boundary particles j of body B is used,

$$d_i = \frac{\sum_{j=1}^{\mathrm{NP}^b} (\mathbf{n}_i \cdot \mathbf{x}_{ij}) \frac{m_j}{\rho_j} W_{ij}}{\sum_{j=1}^{\mathrm{NP}^b} \frac{m_j}{\rho_j} W_{ij}}. \tag{5.18}$$

Here, the normal contact vector $\mathbf{n}_i$ is computed using

$$\hat{\mathbf{n}}_i = \frac{\sum_{j=1}^{\mathrm{NP}^j} \frac{\mathbf{r}_{ij}}{r_{ij}} \frac{m_j}{\rho_j} W_{ij}}{\sum_{j=1}^{\mathrm{NP}^j} \frac{m_j}{\rho_j} W_{ij}}, \tag{5.19}$$

$$\mathbf{n}_i = \frac{\hat{\boldsymbol{n}}_i}{\|\hat{\boldsymbol{n}}_i\|}. \tag{5.20}$$

Utilizing d_i, the overlap δ_n^i is computed by

$$\delta_n^i = \Delta x - d_i, \tag{5.21}$$

where Δx is the initial spacing between the particles. Note that while computing the overlap of particle i with the body B, we have computed an effective overlap, rather than per particle interaction. This effectively is able to model the interaction between non smooth surfaces, contrast from particle particle force computation.

To compute the tangential force, we associate a tangential spring attached to particle i and the interacting body B. The tangential spring is activated when the particle comes into contact with body B, which is conformed by eq. (5.21). The magnitude of the tangential spring is initiated to zero ($|\Delta l_i| = 0$) at the beginning of the contact. The tangential force is history-dependent. The contact friction force is proportional to the tangential spring displacement, which is integrated over the contact time as

$$\mathbf{F}_i^{t^{n+1}} = -k_f \Delta l_i^{n+1} = -k_f [(\Delta l_i^n + \mathbf{v}_{ij}^{n+1} \Delta t) \cdot \mathbf{t}_i^{n+1}] \, \mathbf{t}_i^{n+1}, \tag{5.22}$$

where Δt is the time step, $\mathbf{v}_{ij} = \mathbf{v}_i - \mathbf{v}_j$ is the relative velocity of the primary particle i with respect to the secondary particle j. The tangential unit vector is computed by,

$$\mathbf{t}_i = \frac{\mathbf{v}_{ij} - (\mathbf{v}_{ij} \cdot \mathbf{n}_i)\mathbf{n}_i}{|\mathbf{v}_{ij} - (\mathbf{v}_{ij} \cdot \mathbf{n}_i)\mathbf{n}_i|}. \tag{5.23}$$

Sliding friction condition between the interacting solids is imposed through the Coulomb's law, this is done by coupling the tangential force with the normal force as,

$$\mathbf{F}_i^t = \min(\mu|\mathbf{F}_i^n|, |\mathbf{F}_i^t|) \, \frac{\mathbf{F}_i^t}{|\mathbf{F}_i^t|}. \tag{5.24}$$

The total force acting on the particle i due to the interaction with body B is:

$$\mathbf{F}_i^{cont} = \mathbf{F}_i^n + \mathbf{F}_i^t \tag{5.25}$$

Figure 5.3: Force transfer to the secondary particles j from the primary body particle i

An equal and opposite force of the same magnitude is applied to the closest secondary particle j of i (fig. 5.3),

$$\mathbf{F}_j^{cont} = -\mathbf{F}_i^{cont} \tag{5.26}$$

5.3 Fluid phase modeling

To model the fluid phase, we use CTVF Adepu and Ramachandran (2021) scheme. According to CTVF, the discretized continuity and momentum equation are:

$$\frac{\tilde{d}\rho_a}{dt} = \sum_b \frac{m_b}{\rho_b} \left(\rho_a \, \tilde{\mathbf{u}}_{ab} + (\rho \, (\tilde{\mathbf{u}} - \mathbf{u}))_{ab} \right) \cdot \nabla_a W_{ab}, \tag{5.27}$$

$$\frac{\tilde{d}\mathbf{u}_a}{dt} = -\sum_b m_b \left[\left(\frac{p_a}{\rho_a^2} + \frac{p_b}{\rho_b^2} \right)\mathbf{I} - \left(\frac{\mathbf{A}_a}{\rho_a^2} + \frac{\mathbf{A}_b}{\rho_b^2} \right) \right] \cdot \nabla_a W_{ab}$$
$$+ \mathbf{u}_a \sum_b \frac{m_b}{\rho_b} \, \tilde{\mathbf{u}}_{ab} \cdot \nabla_a W_{ab} + \sum_b m_b \frac{4\eta \nabla W_{ab} \cdot \mathbf{r}_{ab}}{(\rho_a + \rho_b)(r_{ab}^2 + 0.01h_{ab}^2)}\mathbf{u}_{ab} + \mathbf{g}_a, \tag{5.28}$$

where ρ, m, p refer to the is the density, mass, and the pressure respectively. $\mathbf{g}$ represents the gravitational acceleration and η is the kinematic viscosity of the fluid.

where $\mathbf{A}_a = \rho_a \mathbf{u}_a \otimes (\tilde{\mathbf{u}}_a - \mathbf{u}_a)$, $\mathbf{I}$ is the identity matrix, η is the kinematic viscosity of the fluid and Morris *et al.* (1997a) formulation is used to discretize the viscosity term. We add to the momentum equation an additional artificial viscosity term Π_{ab} (Monaghan, 2005a) to maintain the stability of the numerical scheme, given as,

$$\Pi_{ab} = \begin{cases} \frac{-\alpha h_{ab} \bar{c}_{ab} \phi_{ab}}{\bar{\rho}_{ab}} & \mathbf{u}_{ab} \cdot \mathbf{r}_{ab} < 0, \\ 0 & \mathbf{u}_{ab} \cdot \mathbf{r}_{ab} \geq 0, \end{cases} \tag{5.29}$$

where,

$$\phi_{ab} = \frac{\mathbf{u}_{ab} \cdot \mathbf{r}_{ab}}{r_{ab}^2 + 0.01 h_{ab}^2}, \tag{5.30}$$

where $\mathbf{r}_{ab} = \mathbf{r}_a - \mathbf{r}_b$, $\mathbf{u}_{ab} = \mathbf{u}_a - \mathbf{u}_b$, $h_{ab} = (h_a + h_b)/2$, $\bar{\rho}_{ab} = (\rho_a + \rho_b)/2$, $\bar{c}_{ab} = (c_a + c_b)/2$, and α is the artificial viscosity parameter.

For a smoother pressure distribution we use EDAC equation,

$$\frac{\tilde{d}p_a}{dt} = \sum_b \frac{m_b}{\rho_b} \left((p_a - \rho_a c_s^2) \, \mathbf{u}_{ab} \; + \; p_a \, \tilde{\mathbf{u}}_{ab} \; - \; (p \, (\tilde{\mathbf{u}} - \mathbf{u}))_{ab} \; + \right.$$
$$\left. 4 \, \nu_{edac} \frac{p_a - p_b}{(\rho_a + \rho_b)(r_{ab}^2 + 0.01 h_{ab}^2)} \mathbf{r}_{ab} \right) \cdot \nabla_a W_{ab}. \tag{5.31}$$

The particles are moved with a transport velocity for a homogenized particle distribution, where the transport velocity is computed as,

$$\frac{d\mathbf{r}_a}{dt} = \tilde{\mathbf{u}}_a. \tag{5.32}$$

The transport velocity is updated using,

$$\tilde{\mathbf{u}}_a(t + \Delta t) = \mathbf{u}_a(t) + \Delta t \, \frac{\tilde{d}\mathbf{u}_a}{dt} + \left(\frac{d\mathbf{u}_a}{dt} \right)_c \Delta t, \tag{5.33}$$

where $\left(\frac{d\mathbf{u}_a}{dt} \right)_c$ is the homogenization acceleration which ensures that the particle positions are homogeneous. is a displacement based technique due to Sun *et al.* (2017),

$$\left(\frac{d\mathbf{u}_a}{dt} \right)_c = -\frac{\mathrm{Ma} \, (2h)c_0}{\Delta t} \sum_b \left[1 + R \left(\frac{W_{ab}}{W(\Delta x)} \right)^n \right] \nabla_a W_{ab} V_b, \tag{5.34}$$

where R is an adjustment factor to handle the tensile instability, and Ma is the mach number of the flow. V_b is the volume of the bth particle. The acceleration is changed to account for particles that are on the free surface. We use $R = 0.2$ and $n = 4$ as suggested by Sun *et al.* (2019a). Further, the homogenization force has to be adjusted at the free

surface,

$$
\left(\frac{d\mathbf{u}_a}{dt}\right)_{\mathrm{c}} = \begin{cases} 0 & \text{if boundary,} \\ \left(\frac{d\mathbf{u}_a}{dt}\right)_{\mathrm{c}} - \left(\left(\frac{d\mathbf{u}_a}{dt}\right)_{\mathrm{c}} \cdot \mathbf{n}_a\right)\mathbf{n}_a & \text{if } h_b < h, \\ \left(\frac{d\mathbf{u}_a}{dt}\right)_{\mathrm{c}} & \text{if } h_b = h. \end{cases} \tag{5.35}
$$

Where we have utilized the free surface identification scheme provided by (Adepu and Ramachandran, 2021).

5.3.1   Boundary conditions

The dummy particle approach of Adami *et al.* (2012) is used to model the boundaries. We use three layers of dummy particles to model the solid wall. The properties of the solid wall are interpolated from the fluid particles.

When computing the divergence of the velocity field on fluid particles, we enforce a no-penetration boundary condition and not a no-slip boundary condition. The velocity of the fluid is projected onto the ghost particles using,

$$
\hat{\mathbf{u}}_a = \frac{\sum_b \mathbf{u}_b W_{ab}}{\sum_b W_{ab}}, \tag{5.36}
$$

$$
\check{\mathbf{u}}_a = \frac{\sum_b \tilde{\mathbf{u}}_b W_{ab}}{\sum_b W_{ab}}, \tag{5.37}
$$

where $\mathbf{u}_b$, $\tilde{\mathbf{u}}_b$ are the momentum and transport velocity of the fluid respectively and W_{ab} is the kernel value between the fluid particle and the ghost particle.

The normal component of this projected velocity is then reflected and set as the ghost particle velocity,

$$
\mathbf{u}_{\mathrm{Ga}} = 2\hat{\mathbf{n}}((\mathbf{u}_{\mathrm{p}} - \hat{\mathbf{u}}_{\mathrm{a}}) \cdot \hat{\mathbf{n}}) + \hat{\mathbf{u}}_{\mathrm{a}}, \tag{5.38}
$$

where $\mathbf{u}_{\mathrm{p}}$ is the local velocity of the boundary and $\hat{\mathbf{n}}$ is the unit normal to the boundary particle *a*. Similarly the transport velocity of the ghost particle is set as,

$$
\tilde{\mathbf{u}}_{\mathrm{Gi}} = 2\hat{\mathbf{n}}((\mathbf{u}_{\mathrm{p}} - \check{\mathbf{u}}_{\mathrm{i}}) \cdot \hat{\mathbf{n}}) + \check{\mathbf{u}}_{\mathrm{i}}, \tag{5.39}
$$

When the viscous force is computed, the no slip boundary condition is used, where the velocity on the boundary set as,

$$
\mathbf{u}_{\mathrm{Ga}} = 2\mathbf{u}_{\mathrm{p}} - \hat{\mathbf{u}}_{\mathrm{a}}, \tag{5.40}
$$

a similar form is used for the transport velocity here too,

$$
\tilde{\mathbf{u}}_{\mathrm{Ga}} = 2\mathbf{u}_{\mathrm{p}} - \check{\mathbf{u}}_{\mathrm{a}}. \tag{5.41}
$$

The pressure of the boundary particle is extrapolated from its surrounding fluid particles by the following equation,

$$p_w = \frac{\Sigma_f p_f W_{wf} + (\mathbf{g} - \mathbf{a_w}) \cdot \Sigma_f \rho_f \mathbf{r}_{wf} W_{wf}}{\Sigma_f W_{wf}},$$
(5.42)

where $\mathbf{a}_w$ is the acceleration of the wall. The subscript f denotes the fluid particles and w denotes the wall particles.

5.3.2   Rigid fluid coupling

The interaction between the fluid and the rigid body are handled using the dummy particle approach of (Adami *et al.*, 2012). The particles of the rigid body are assumed as dummy particles with hydrodynamics properties of mass and density while interacting with the fluid particles. We set the pressure of the boundary particles from the extrapolated equation (Adami *et al.*, 2012) as,

$$p_s = \frac{\Sigma_f p_f W_{sf} + (\mathbf{g} - \mathbf{a_s}) \cdot \Sigma_f \rho_f \mathbf{r}_{sf} W_{sf}}{\Sigma_f W_{sf}}.$$
(5.43)

Here, $\mathbf{a}_s$ is the acceleration of the rigid body particles. The subscript f denotes the fluid and s the rigid body particles. Using the extrapolated pressure, the hydrodynamic density and mass of rigid body particle is set as,

$$\rho_{s0} = p_s/c_0^2 + \rho_0$$
(5.44)

$$m_{s0} = \rho_{s0} V_s$$
(5.45)

Here the volume of the particle remains same, and is set to dx^2 in two dimensions and dx^3 in three dimensions.

By utilizing the previously set hydrodynamic properties on the rigid body, the interaction force is computed using,

$$\mathbf{F}_{\text{RFC}}^i = -m_i \sum_s m_s \left(\frac{p_i}{\rho_i^2} + \frac{p_s}{\rho_s^2} \right) \nabla_i W(x_{is})$$
(5.46)

where i is fluid particle, s is particle of rigid body.

5.3.3   Time integration

We use the kick-drift-kick scheme for the time integration. We first move the velocities of the particles to half time step,

$$\mathbf{u}_a^{n+\frac{1}{2}} = \mathbf{u}_a^n + \frac{\Delta t}{2} \left(\frac{\tilde{d}\mathbf{u}_a}{dt} \right)^n,$$
(5.47)

$$\tilde{\mathbf{u}}_a^{n+\frac{1}{2}} = \mathbf{u}_a^{n+\frac{1}{2}} + \frac{\Delta t}{2}\left(\frac{d\mathbf{u}_a}{dt}\right)_c^n. \tag{5.48}$$

Then the time derivatives of density and pressure are calculated using the eq. (5.27) and eq. (5.31). The new time step density, pressure and particle position are updated by,

$$\rho_a^{n+1} = \rho_a^n + \Delta t \left(\frac{\tilde{d}\rho_a}{dt}\right)^{n+\frac{1}{2}}, \tag{5.49}$$

$$p_a^{n+1} = p_a^n + \Delta t \left(\frac{\tilde{d}p_a}{dt}\right)^{n+\frac{1}{2}}, \tag{5.50}$$

$$\mathbf{r}_a^{n+1} = \mathbf{r}_a^n + \Delta t\,\tilde{\mathbf{u}}_a^{n+1}. \tag{5.51}$$

Finally, at new time-step particle position, the momentum velocity is updated

$$\mathbf{u}_a^{n+1} = \mathbf{u}_a^{n+\frac{1}{2}} + \frac{\Delta t}{2}\left(\frac{\tilde{d}\mathbf{u}_a}{dt}\right)^{n+1}. \tag{5.52}$$

For the numerical stability of fluid phase, the time step depends on the CFL condition as,

$$(\Delta t)_{\text{fluid}} = \min\left(0.25\,\frac{h}{c+|U|}, 0.25\,\frac{h^2}{\nu}, 0.25\,\frac{h^2}{g}\right), \tag{5.53}$$

where $|U|$ is the maximum velocity magnitude, c is the speed of sound typically chosen as $10|U|$ for fluids in this work. For rigid body, the time step is constrained as,

$$(\Delta t)_{\text{rb}} \le \frac{\pi}{50}\sqrt{\frac{m}{K_r}}. \tag{5.54}$$

We choose minimum of both the phases fields for a stable simulation as following,

$$\Delta t = min((\Delta t)_{\text{fluid}}, (\Delta t)_{\text{rb}}) \tag{5.55}$$

5.4 Results and discussion

5.4.1 Cylinder rolling on an inclined plane

A cylinder of diameter 1.0 m rolling on an inclined plane under gravity is simulated in the current test case. The physical model is shown in fig. 5.4a, while the computational model is in fig. 5.4b. In the computational model the x-axis points in the direction of the slope, where the gravity makes an angle θ with the vertical. The physical and the numerical parameters are given in table 5.1. A total of two friction coefficients are simulated. Analytical expression of the variation of the center of mass of the cylinder with time is,

$$x_{cm}(t) = \begin{cases} x_0 + \frac{1}{2}\,g\,t^2\,(\sin(\theta) - \mu\cos(\theta)) & \tan\theta > 3.5\mu, \\ x_0 + \frac{1}{3}\,g\,t^2\,\sin(\theta) & \tan\theta \le 3.5\mu. \end{cases} \tag{5.56}$$

(a)

(b)
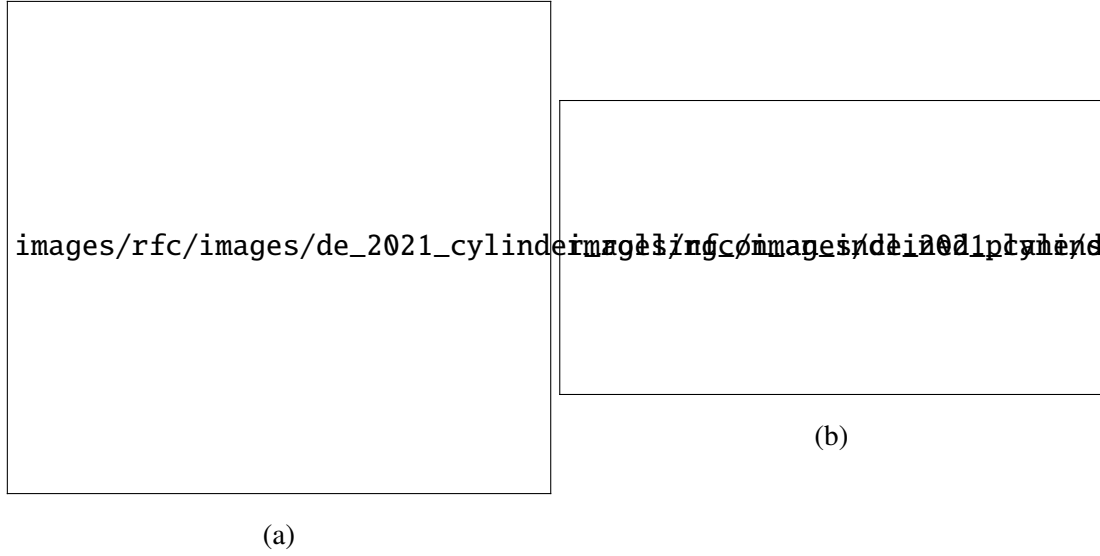
Figure 5.4: A (a) physical and (b) computational model of the rolling cylinder on a plane inclined at an angle θ.

Quantity	Values
ρ, density	2700 kg m^{-3}
μ, friction coefficient	0.3 & 0.6
Time of simulation	0.6 s
Resolution, δx	0.0025 m
Smoothing length factor, $h/\Delta x$	1
gravity $[g_x, g_y, g_z]$	$[g \, \sin(\theta), g \, \cos(\theta), 0.0]$
k_r, Repulsive stiffness coefficient	$1e7$
k_f, Repulsive stiffness coefficient	$1e5$
α_{damp}	0.

Table 5.1: Material properties and numerical parameters used for the rolling of cylinder on an inclined surface.

Here, x_0 is the initial position of the center of mass of the cylinder.

Figure 5.5 depicts the variation of center of mass of the cylinder with time for friction coefficients 0.3 and 0.6, respectively. From the fig. 5.5 we can see that the current solver matches well with the analytical solution.

5.4.2   Rigid body sliding down an inclined plane

In this test case, free sliding of a rigid cube on a frictional inclined plane is studied. The frictional part of the current solver is validated through this test. The velocity of

figures/rfc/figures/de_2021_cylinder_rolling_on_an_inclined_pl
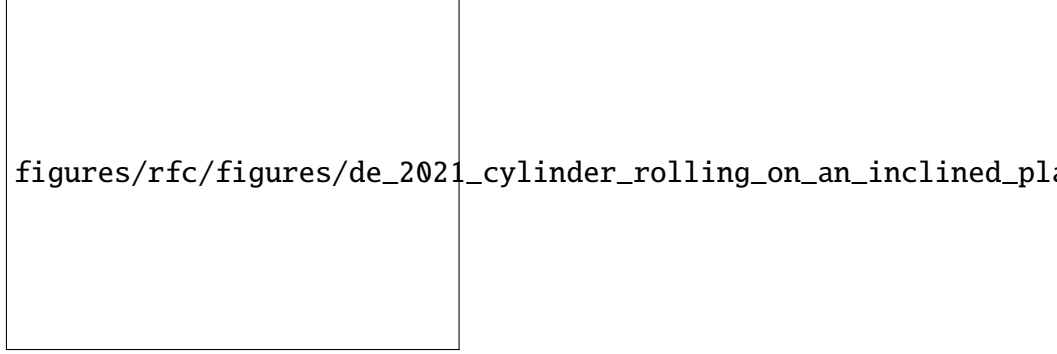
Figure 5.5: x-component of center of mass variation with time for a cylinder rolling down an inclined plane.

the center of mass of the cube is compared against the analytical solution for quantitative validation. The schematic is shown is fig. 5.6. The rigid body of length 0.1 m, height 0.1

images/rfc/images/rigid_body_sliding/schematic.png
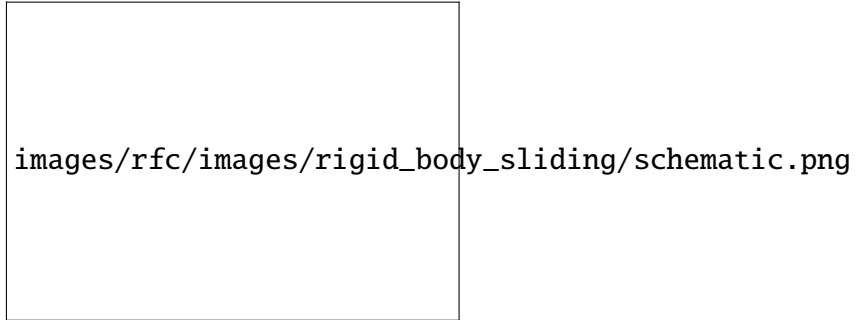
Figure 5.6: Schematic of a square body sliding down an inclined plane under gravity.

m, is allowed to slide on a frictional surface which is at an angle $\frac{\pi}{3}$. A density of 2000 kg m^{-3} is used for the body. Other numerical parameters, such as the repulsive spring stiffness $k_r = 3.0 \times 10^5$ N/m and tangential spring stiffness $k_t = 3.0 \times 10^5$ N/m is chosen, respectively. A particle spacing of 0.001 m is considered, resulting in 120 particles in rigid body discretization. From the analytical solution, the evolution of velocity is given by,

$$\mathbf{v}(t) = (\mu \boldsymbol{g} \sin(\theta) - \boldsymbol{g} \cos(\theta))t. \tag{5.57}$$

We have considered three different friction coefficients, $\mu = 0.2$, $\mu = 0.3$, and $\mu = 0.6$. From the analytical solution, when the friction coefficient is greater than $\tan(\frac{\pi}{3})$, we have no slip condition and the body doesn't slide.

Figure 5.7 shows the snapshots of the rigid body at three time instants. From fig. 5.7 we can see that the the body is freely sliding with out having any oscillations or unphysical jumping off the inclined wall. This is because of the new surface aware contact model as force is not computed by considering the wall as spherical particles but by ensemble of

figures/rfc/figures/mohseni_2021_free_sliding_on_a_slope_2d/fr

(a) t = 0 s

(b) t = 0.5 s

figures/rfc/figures/mohseni_2021_free_sliding_on_a_slope_2d/fr

(c) t = 1 s

Figure 5.7: Snapshots of rigid body sliding down an inclined plane with a friction coefficient of 0.2.

an overlap. The snapshots correspond to a friction coefficient of 0.2. Figure 5.8 shows a evolution of velocity of the center of mass of the rigid body for different frictional coefficients against the analytical solution. From fig. 5.8 we can see that the current solver has an excellent match with the analytical solution and covers all the regimes of the sliding case.

Figure 5.8: Variation of the velocity of the rigid body with time for different friction coefficients. Present result is compared against the analytical result.

3D sliding

Figure 5.10 shows the snapshots of the rigid body at three time instants for a 3D sliding case. From fig. 5.10 we can see that the the body is freely sliding with out having any oscillations or unphysical jumping off the inclined wall. The snapshots correspond to a friction coefficient of 0.4. Figure 5.9 shows a evolution of velocity of the center of mass of the rigid body for different frictional coefficients against the analytical solution. From Figure 5.9 we can see that the current solver has an excellent match with the analytical solution and covers all the regimes of the sliding case for a 3D case.

5.4.3   Controlled Sliding on a Flat Surface

A controlled sliding of rigid body on a frictional surface is studied in the current test case. The schematic of the rigid body as well as the wall is shown in fig. 5.11. The rigid body is acted upon by normal (**F**) and tangential force (**T**), where, force **F** is applied on top of the body for 1.0 second, which gradually increases to 2000 N till 0.5 seconds, and stays constant till 1.0 second. Once the normal force **N** reaches 2000 N, we start applying the tangential force of magnitude 4000 N, which increases linearly till 1.0 seconds. The friction coefficient between the body and wall is assumed to be 0.5.

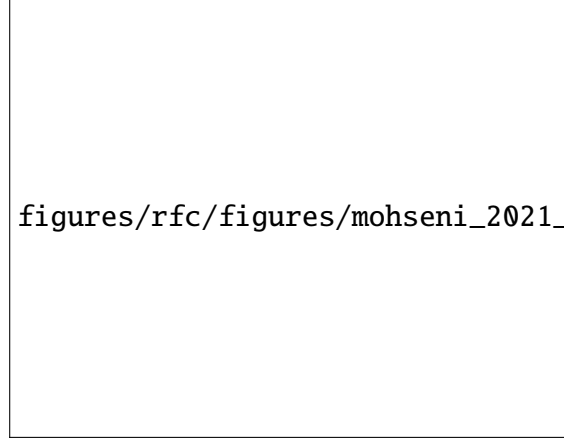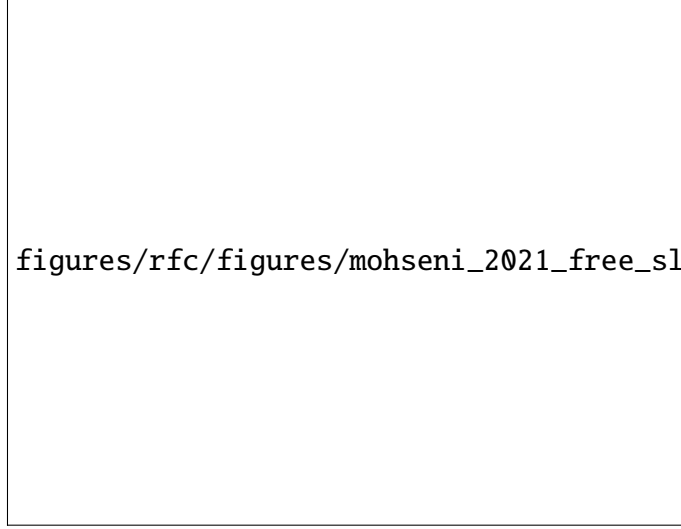Figure 5.9: A 3D case - Variation of the velocity of the rigid body with time for different friction coefficients. Present result is compared against the analytical result.

Figure 5.12 depicts the time histories of velocity of the center of mass of the rigid body with time, as well as the variation of applied external normal **F** and tangential **T** forces against the velocity computed using analytical solution.

5.4.4   Stack of cylinders

This test case is used to validate the current solid-solid contact force model with the help of a experimental problem. A stack of cylinders initially at rest are allowed to settle under gravity inside a tank. This experiment is conducted by (Zhang *et al.*, 2009), and a numerical analysis is carried out by the same with DEM. The material and numerical parameters are listed in Table 5.2.

Figure 5.13 presents a set of snapshots corresponding to the simulation of a stack of cylinders collapsing under gravity using developed solver in comparison with the corresponding experimental photos by (Zhang *et al.*, 2009). From the presented fig. 5.13, the reproduced cylinders' positions appear to be consistent with those observed in the experiment. From fig. 5.13, the current solver has presented proper level of stability.

Figures 5.14 and 5.15 presents the time histories of the x and y components of the center of mass of the cylinders respectively as well as those from the experimental result of (Zhang *et al.*, 2009). From the presented figure, we can see that the effective center of mass of the cylinders is in good agreement with the experiment.

(a) t = 0 sec

(b) t = 0.5 sec

(c) t = 1.0 sec
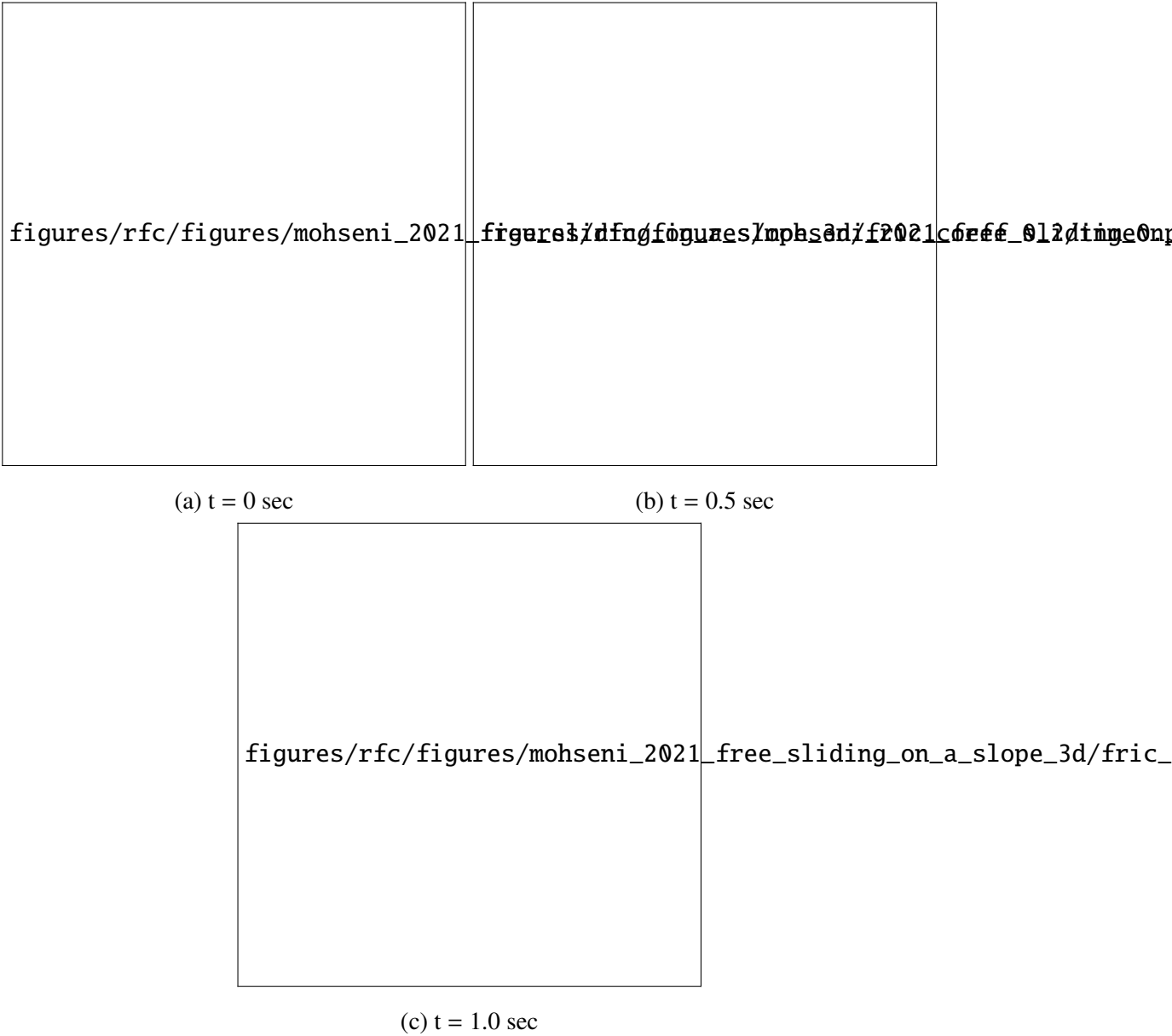
Figure 5.10: 3D case - Snapshots of rigid body sliding down an inclined plane with a friction coefficient of 0.2.
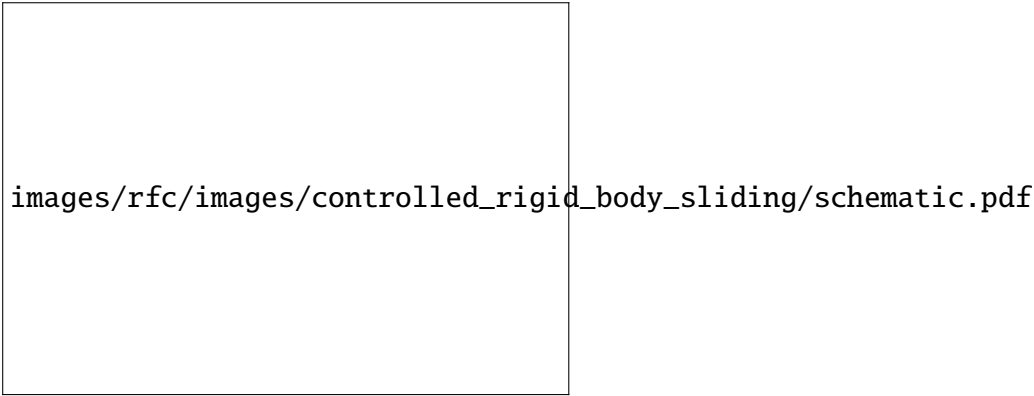
Figure 5.11: Schematic of the controlled sliding of a rigid body.

figures/rfc/figures/mohseni_2021_controlled_sliding_on_a_flat_surface

Figure 5.12: Force and Velocity vs time curves of the of the controlled rigid slider.

Quantity	Values
L, length of the tank	0.26 m
Diameter of the cylinder	0.01 m
Friction coefficient	0.45
ρ_b, density of the cylinder	2700 kg/m^3
Spacing, dx	0.001m
Normal stiffness, K_r	10^7 N/m^1
Tangential stiffness, K_t	10^5 N/m^1
Smoothing length factor, $h/\Delta x$	1.0

Table 5.2: Numerical and material parameters used in the simulation of collapse of stack of cylinders in a tank.

5.4.5   Falling cube of density 2200 kg/m^3 in a steady hydrostatic tank in water

In this section, the rigid fluid coupling part of the current solver is evaluated by simulation of a rigid cube falling in an hydrostatic tank (Qiu *et al.*, 2017). The CTVF-DEM solver is employed to simulate water entry of a rigid cube, which is studied experimentally by (Wu). The numerical and material parameters of the current test case are listed in table 5.3.

figures/rfc/figures/stack_of_cylinders_image/onsen/imagas/stack.pngcylinders_experime

figures/rfc/figures/stack_of_cylinders_image/onsen/imagas/stack.pngcylinders_experime

figures/rfc/figures/stack_of_cylinders_image/onsen/imagas/stack.pngcylinders_experime

figures/rfc/figures/stack_of_cylinders_image/onsen/imagas/stack.pngcylinders_experime
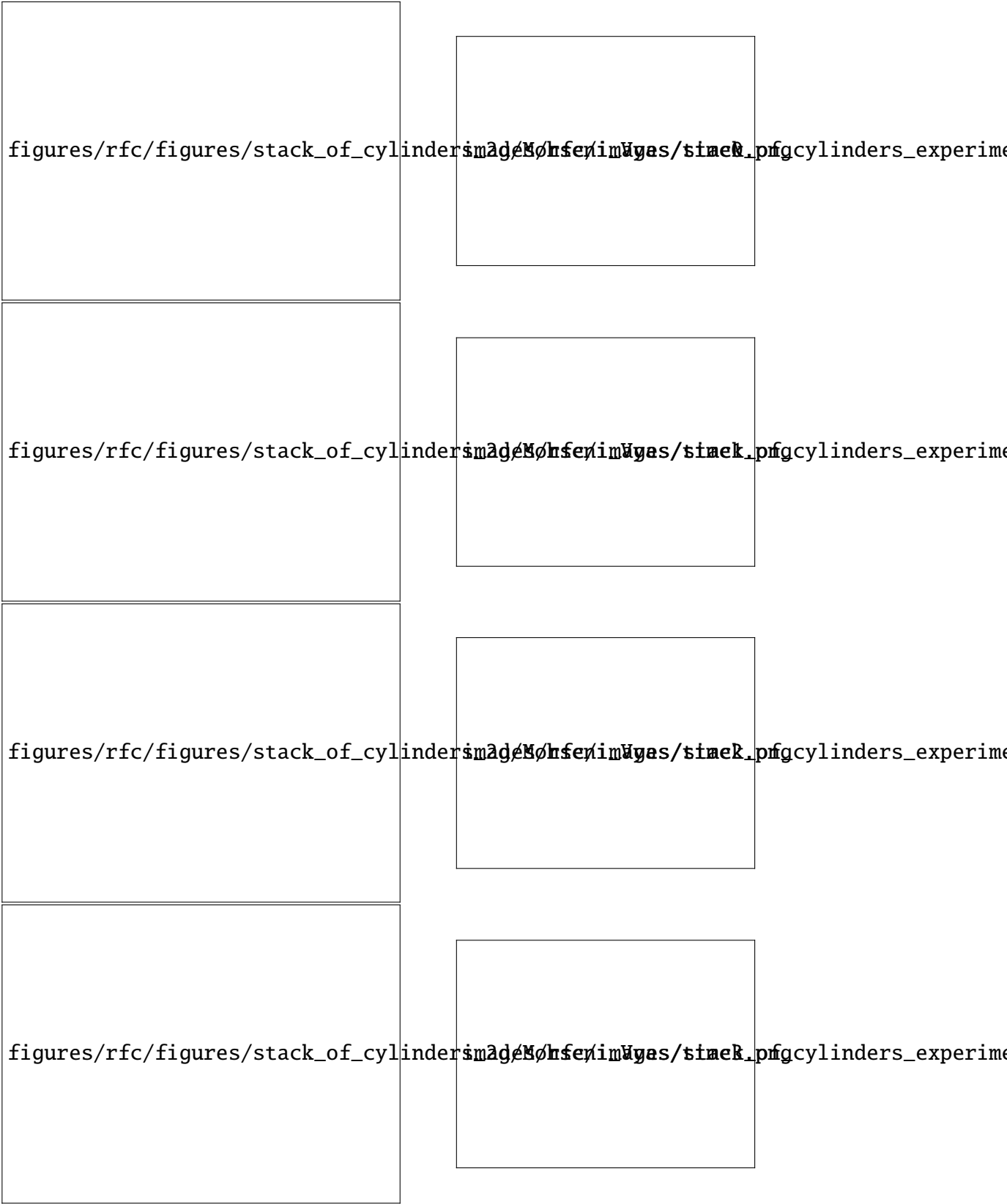
Figure 5.13: Snapshot of the collapsing cylinders at different time stamps simulated with
the current solver, compared against the experimental pictures (Zhang *et al.*, 2009).

figures/rfc/figures/stack_of_cylinders_2d/Mohseni_Vyas/xcom
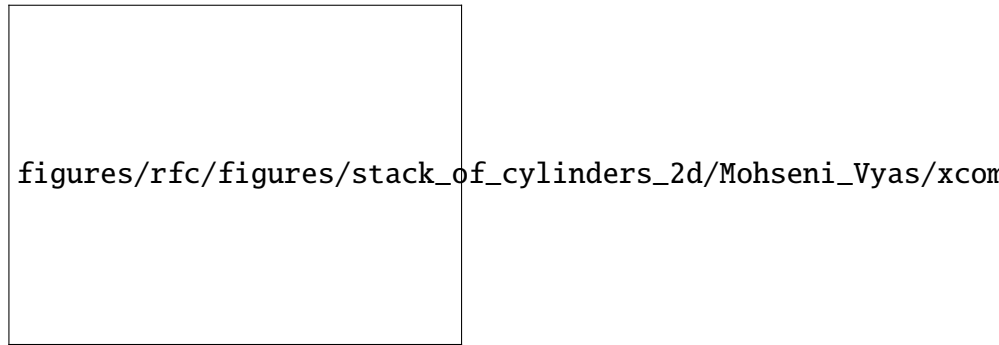
Figure 5.14: Variation of the x-component of the center of mass of the collapsing cylinders computed using the current solver compared against experimental results.

figures/rfc/figures/stack_of_cylinders_2d/Mohseni_Vyas/ycom
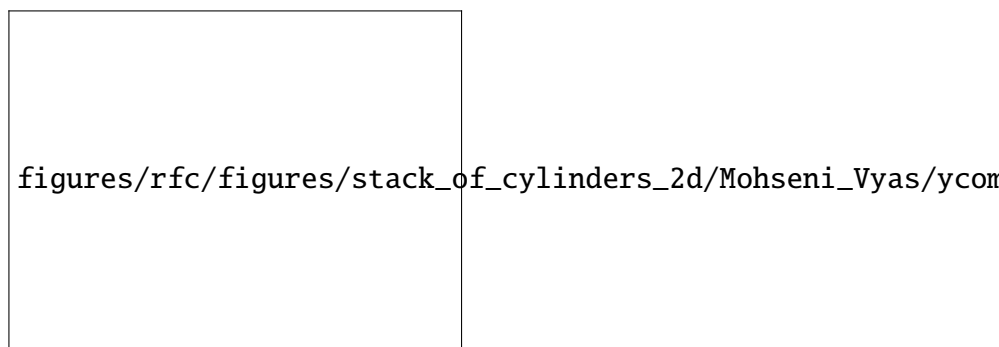
Figure 5.15: Variation of the y-component of the center of mass of the collapsing cylinders computed using the current solver compared against experimental results.

Quantity	Values
L, length of the domain	1 m
Time of simulation	2.5 s
c_s	10 m/s
ρ_0, reference density	1 kg/m^3
Reynolds number	200 & 1000
Resolution, $L/\Delta x_{\max} : L/\Delta x_{\min}$	[100 : 200] & [150 : 300]
Smoothing length factor, $h/\Delta x$	1.0

Table 5.3: Numerical and material parameters used in the simulation of water entry of a rigid cube.

A rigid cube of a side length of 30 mm enters the water initially at hydrostatic state with a velocity of 30 m/s in z-direction. Figure 5.16 presents a snapshots of the rigid cube falling in an hydrostatic tank with the current solver as well as WCSPH-DEM solver as well as the experimental result. From the presented figure Figure 5.16, we can see that the pressure distribution is smooth and the simulation is stable. From fig. 5.16 we can see that the fluid particle distribution around the body with CTVF scheme is uniform, this is because of the transport velocity formulation. Figure 5.20 presents the time history of the displacement of the rigid cube with time in comparison with the experimental result by (citep experimental paper). From the presented figure, the CTVF-DEM model has reproduced the displacement of the rigid cube with acceptable levels of stability as well as accuracy.

5.4.6   Water-entry of a single sphere

In this section we reproduce the water entry of a single sphere experiment done by (Aristoff *et al.*, 2010). A sphere of diameter 24.4 mm is allowed to settle under gravity in a water tank of dimensions, 0.2 m × 0.2 m × 0.14 m, with a water depth of 0.11 m (fig. 5.18). The initial velocity of the sphere is 2.17 m/s. A convergence study of the current rigid fluid coupling algorithm is carried out by simulating a total of 3 resolution studies (0.01 m, 0.005 m, 0.002 m) is carried out.

5.5   Summary

A coupled solver, CTVF-DEM is developed to simulate a two-way rigid-fluid coupling phenomenon. The fluid phase is handled by the CTVF scheme, while DEM is used to

(a) t = 0 sec

(b) t = 0.2 sec

(c) t = 0.3 sec

(d) t = 0.5 sec
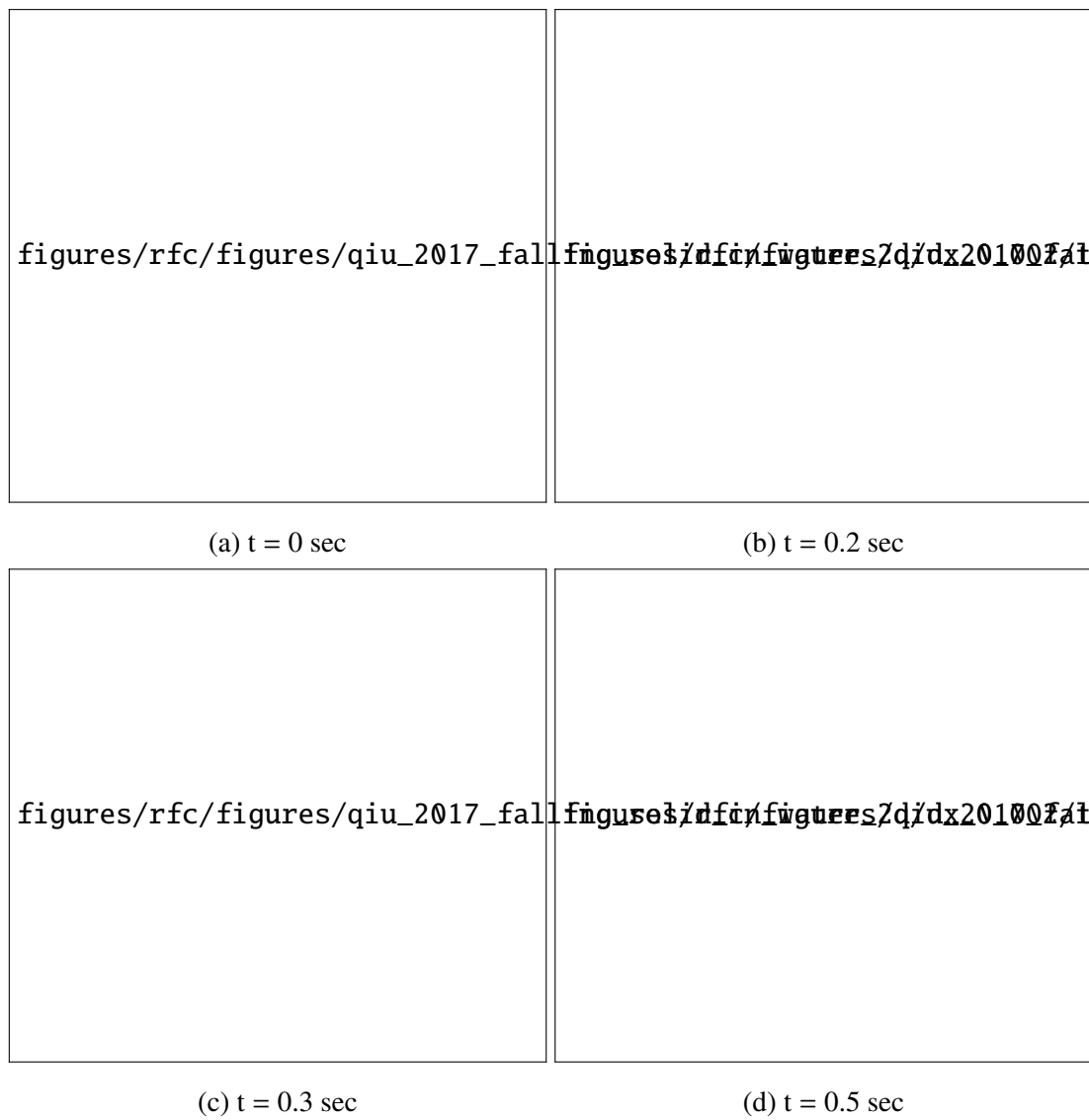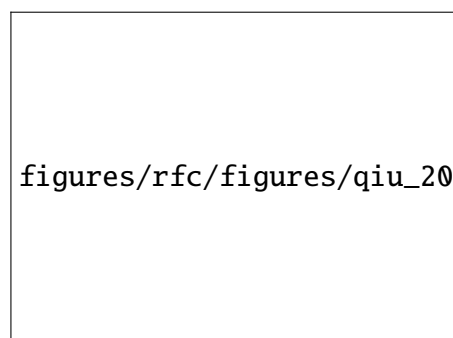
Figure 5.16

Figure 5.17: Snapshots of the rigid cube entering a hydrostatic tank at four different time instants simulated with the current solver.

images/rfc/images/water_entry_of_sphere/schematic.pdf

Figure 5.18

figures/rfc/figures/dinesh_2022_body_in_hs_tank_2d/figures/dinesh_2022_body_in_hs_tank_2

figures/rfc/figures/dinesh_2022_body_in_hs_tank_2d/figures/dinesh_2022_body_in_hs_tank_2

(a) t = 0 sec   (b) t = 0 sec

figures/rfc/figures/dinesh_2022_body_in_hs_tank_2d/figures/dinesh_2022_body_in_hs_tank_2

figures/rfc/figures/dinesh_2022_body_in_hs_tank_2d/figures/dinesh_2022_body_in_hs_tank_2

(c) t = 0 sec   (d) t = 0 sec
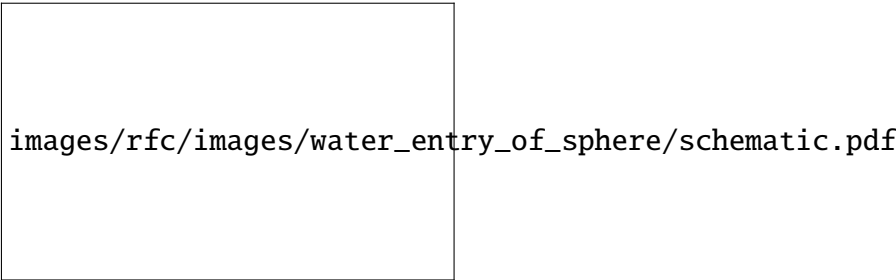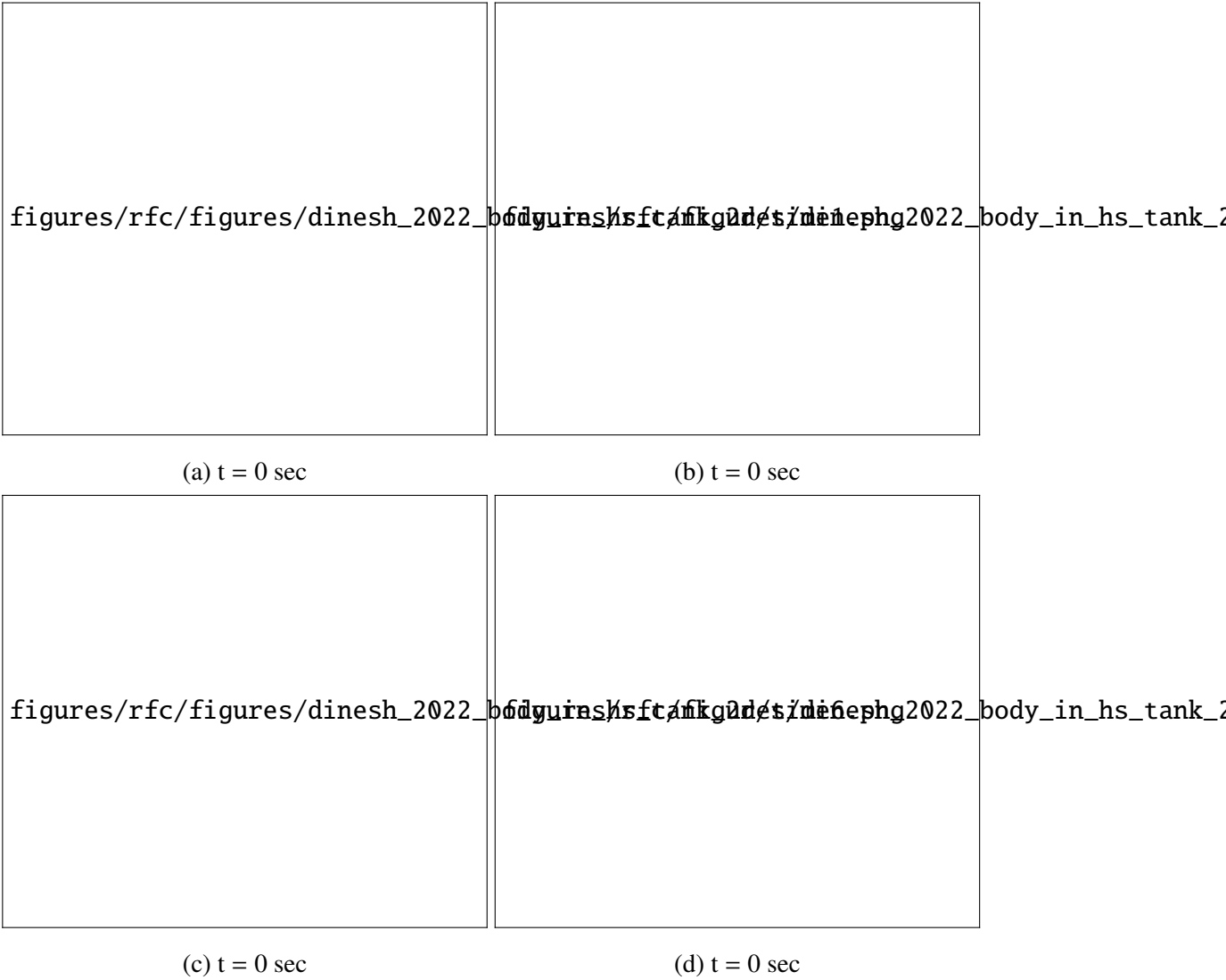
Figure 5.19: Snapshots of a 2D-cylinder of density 500 kg^{-3} rising in a hydrostatic tank at four different time instants simulated with the current solver.
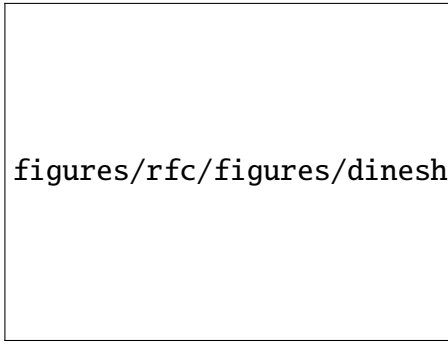
Figure 5.20

handle the interaction between the arbitrarily shaped rigid bodies. A modified contact force formulation is utilized in DEM to handle the contact between the arbitrarily shaped bodies.

It has been demonstrated that the current model is able to predict behaviour of rigid bodies under the influence of fluid flow with different test cases. A square cube sliding down an inclined plane is simulated to test the interaction model between the rigid bodies. Different test cases are used to test the rigid -fluid coupling phenomenon. Water entry and rising of solid bodies is studied as part of the rigid-fluid coupling analysis. Further, we have made our implementation open-source and fully reproducible.

With the completion of modeling fluid, elastic, fluid-structure and the contact between the solids, in the current chapter we have modeled dynamics of rigid bodies in fluid flows and rigid-rigid interaction. In the next chapter we will model the interaction between the rigid and a ductile target. The ductile target is modelled assuming elastic-plastic, where the solver in chapter 2 is extended to handle the plastic behaviour through Johnson-Cook constitutive model.

Chapter 6

Erosion

6.1   Introduction

Solid body erosion can be seen in every day life in various physical processes. It is commonly seen in areas where solid particles are carried in a pipe, body part erosion of an aircraft due to high speed impact of particles. Due to the continuous erosion, the conveying systems can result in total damage and failure of the manufacturing system. Similarly, the aerodynamic performance of the wings as well as other parts of an aircraft may reduce. An accurate study of the solid particle erosion can be helpful in improving the life and efficiency of such systems and reduce the maintenance cost. Experimental investigation is complex. Also, the experimental investigation will not give insight into the details of the erosion process.

In the current chapter we model the solid particle erosion of a ductile target. We utilise the developments done to this point. Handling of collision between the rigid bodies, elastic bodies and modeling of elastic structure in chapters 2 to 3 is utilized. We develop a numerical method to simulate elastic-plastic solids. The current scheme is able to eliminate several issues in classic SPH method. A contact force model is used to handle the collision between the impactor and the target. The developed technique is further applied to handle rigid fluid coupling as well as to model fluid structure interaction problems. Finally, an elastic-plastic algorithm is incorporated in the new scheme to model the solid particle erosion. The complete work is made open source and is fully reproducible.

6.2   Numerical method

In the current section we write the equations governing the behaviour elastic-plastic target. We utilise the scheme developed in chapter 2 to model the elastic solids, to which we add

additional equations to consider the plastic behaviour. We employ the equations used in chapter 5 to model the dynamics of the rigid bodies as well as their interaction. From chapter 3 and chapter 5, we develop a contact force formulation and adapt it to handle the contact between the rigid and an elastic-plastic body.

6.2.1 Discrete governing equations of the ductile target

In addition to the equations of an elastic solid in section 2.3.2, i.e., continuity and momentum, we consider energy equation to track the temperature of the solid particles. While the momentum equation is modified to consider the contact due to the external impact. The new set of equations are,

Figure 6.1: Bodies under collision which are divided into primary and secondary.

$$\frac{\tilde{d}\mathbf{u}_a}{dt} = -\sum_{b \in A} m_b \left[\left(\frac{p_a}{\rho_a^2} + \frac{p_b}{\rho_b^2} \right) \mathbf{I} - \left(\frac{\sigma_a'}{\rho_a^2} + \frac{\sigma_b'}{\rho_b^2} + \Pi_{ab}\mathbf{I} \right) \right] \cdot \nabla_a W_{ab} + \mathbf{g}_a + \frac{1}{m_a} \sum_{b \in B} \mathbf{F}_{a \leftarrow b}^{\text{cont}} \quad (6.1)$$

$$\frac{\tilde{d}e_a}{dt} = -\frac{1}{2} \sum_{b \in A} m_b \left(\frac{p_a}{\rho_a^2} + \frac{p_b}{\rho_b^2} + \Pi_{ab} \right) (\mathbf{v}_a - \mathbf{v}_b) \cdot \nabla_a W_{ab} + \frac{1}{\rho_a} \sigma_a' \epsilon_a. \quad (6.2)$$

Here, $\mathbf{F}_a^{cont}$ is the force acting on particle a due to contact with the other impacting rigid bodies which will be discussed in section 6.2.3. The boundary conditions, particle position evolution are similar to chapter 2. These equations are combined with von-Mises flow criterion to model the plasticity as described below.

We consider Johnson-Cook constitutive law to compute the flow stress of the ductile body. Johnson-Cook model accounts for the effects of strain hardening, strain rate hardening, and thermal softening. The flow stress is computed using

$$\sigma_y = \left[A + B(\epsilon_{eff}^p)^N \right] \left[1 + C \ln \left(\frac{\dot{\epsilon}_{eff}^p}{\dot{\epsilon}_0} \right) \right] \left[1 - (T^*)^M \right], \quad (6.3)$$

where,

$$\dot{\epsilon}^p_{eff} = \sqrt{\dot{\epsilon}_{\alpha\beta}\dot{\epsilon}_{\alpha\beta}}, \tag{6.4}$$

$A, B, N, \dot{\epsilon}_0, C, M$ are the Johnson-Cook parameters. T^* is given as

$$T^* = \frac{T - T_{ref}}{T_{melt} - T_{ref}}, \tag{6.5}$$

where T_{ref}, T_{melt}, T are the room temperature, and melting point temperature. T is the temperature of the particle evolved using an energy equation. The stress of the particle is adjusted in the integrator step (see **??**). The trial deviatoric stress $\sigma^{'\,*}_{\alpha\beta}$ at the next time step is given as,

$$\sigma^{'\,*}_{\alpha\beta} = \sigma^{'\,n}_{\alpha\beta} + \left(\frac{d\sigma^{'}}{dt}\right)_{\alpha\beta} dt \tag{6.6}$$

By using the flow stress computing using the Johnson-Cook model, we check if the trial stress exceeds the yield value, which in case will be bought back to the limit using the following equations,

$$f_y = \min(\sigma_y/\sigma^{'\,*}, 1). \tag{6.7}$$

where $\sigma^{'\,*} = \sqrt{\frac{3}{2}\sigma^{'\,*}_{ij}\sigma^{'\,*}_{\alpha\beta}}$.

$$\sigma^{'\,n+1}_{\alpha\beta} = \hat{f}\,\sigma^{'\,*}_{\alpha\beta} \tag{6.8}$$

Finally, the new stress state is computed as

$$\sigma^{n+1}_{\alpha\beta} = -P^{n+1}\delta_{\alpha\beta} + \sigma^{'\,n+1}_{\alpha\beta} \tag{6.9}$$

Similarly, the plastic strain increment is given by

$$\Delta\epsilon^p_{\alpha\beta} = (1 - \hat{f})\sigma^{'\,*}_{\alpha\beta}/2\mu, \tag{6.10}$$

and the effective plastic strain increment is computed as,

$$\Delta\epsilon^p = \frac{1}{3}\frac{1 - \hat{f}}{\mu}\sigma^{'\,*} \tag{6.11}$$

$$\epsilon_{\text{failure}} = [D_1 + D_2 \exp(D_3\sigma^*)]\left[1 + D_4 ln(\frac{\dot{\epsilon}^p_{eff}}{\dot{\epsilon}_0})\right][1 + D_5 T^*] \tag{6.12}$$

$$D = \sum \frac{\Delta\epsilon^p_{eff}}{\epsilon_{\text{failure}}} \tag{6.13}$$

6.2.2   Rigid body dynamics

Following **?**, the governing equations of the rigid body are,

$$\frac{d\,(M\mathbf{v}_{cm})}{dt} = \sum_i \mathbf{F}_i,$$ (6.14)

$$\frac{d\mathbf{L}}{dt} = \tau$$ (6.15)

where $\mathbf{F}_a = \mathbf{F}_a^{RB} + \mathbf{F}_a^{DS}$ are due to the interaction with other rigid bodies ($\mathbf{F}_a^{RB}$) and the ductile solid($\mathbf{F}_a^{DS}$). Force due to the other rigid bodies ($\mathbf{F}_a^{RB}$) is computed using the formulation provided in **?** while the force between the rigid body and the ductile solid is shown in section 6.2.2.

6.2.3   Contact force law

Following sections 3.3 and 5.2.1, we compute the forces on the ductile body as well as the rigid body. In the current case we consider the ductile body as the primary body and the rigid projectile as secondary. This is due to the fact that the boundary particles of the rigid body remains constant while the ductile target undergoes erosion and the surface particles needs to be recomputed at every time instant if the target erodes.

images/erosion/images/contact_force/contact_force_divide.pdf

Figure 6.2: Bodies under collision which are divided into primary and secondary.

Force on the particle *i* of elastic-plastic structure is computed as,

6.3   Result: A rigid sphere hitting a ductile specimen at different impact velocities

In the current example, we simulate the impact of a 3D sphere on a wall at different impact velocities, where the experimental evaluation is done by Zang *et al.* (2022). The
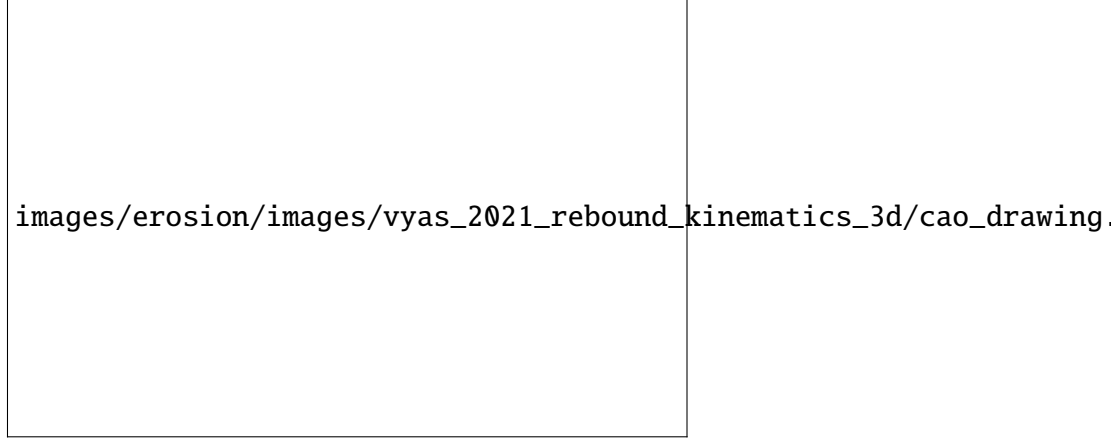
Figure 6.3: A spherical particle impacting a ductile target at an impact angle with a velocity $\mathbf{V}_i$.

model description is shown in fig. 6.3. The sphere is assumed to be rigid and the material properties as well as the numerical parameters used are displayed in table 6.1. The sphere is impacted on the wall by varying the incident velocities ($\mathbf{V}_i$) keeping the incident angle constant, 45 degrees.

Quantity	Values
E, Young's modulus	70 GPa
ν, Poisson's ratio	0.33
ρ, density	2700 kg m^{-3}
μ, friction coefficient	0.1
Time of simulation	0.25 ms
Resolution, δx	0.00153 m
Smoothing length factor, $h/\Delta x$	1.0
gravity $[g_x, g_y, g_z]$	$[0.0, -9.81, 0.0]$
k_r, Normal stiffness coefficient	10^7
k_f, Tangential stiffness coefficient	10^5
Radius, Sphere radius	5×10^{-3} m

Table 6.1: Numerical parameters and material properties for sphere impacting a target.

Figure 6.4 depicts the variation of the depth against the incident velocity $\mathbf{V}_i$. The simulated results are compared to the experimental results by Zang *et al.* (2022) as well as the computational results simulated using finite element method modeling. We wish to complete this problem till the time of thesis submission.

Quantity	Values
A	335 MPa
B	85 MPa
C	0.012
m	1
n	0.11
T_{ref}	292K
T_{melt}	925K

Table 6.2: Johnson-Cook constitutive model parameters for the target.

figures/erosion/figures/cao_xuerui_2022_spherical_particle_impact_3d/

Figure 6.4: Variation of the penetration depth with the varying incident velocity magnitude compared against the experimental and numerical study with the current solve.

Chapter 7

Conclusions and Future Work

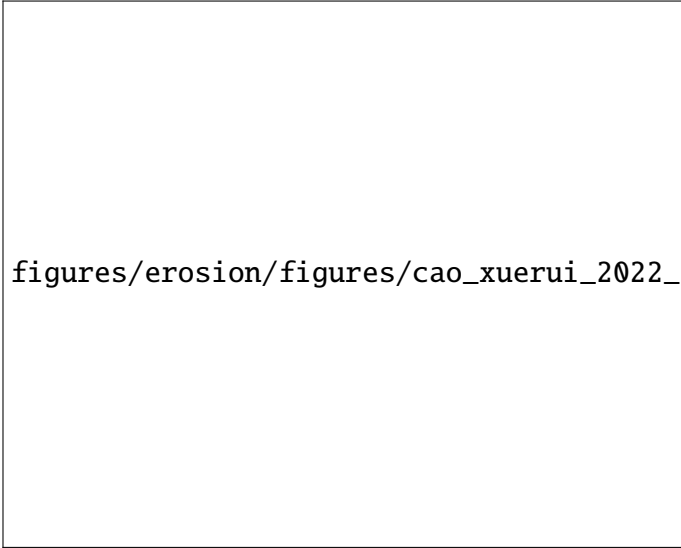Abrasive water jet machining is widely seen phenomenon. AWJM involves several physical processes. Fluid, elastic plastic, rigid bodies collision, interaction between fluid and elastic solids. Meshbased methods are difficult, faces issues modeling free surface flows, large deformation problems, and multiphysics or multiphase problems. We have chosen a particle based methods to study the physics involved in AWJM. Each subprocess is modelled individually and validated against analytical and experimental results.

We started with SPH to model the elastic dynamics and fluid flow. After basic SPH introduction is given, it is applied to classic problems of fluid and elastic dynamics. It is found that SPH suffers from tensile instability, particle inhomogeneity, high pressure oscillation problems. A corrected transport velocity formulation in SPH is developed to solve the issues faced by the classical SPH. While there exists transport velocity formulation, where the particles are moved with transport velocity rather than momentum velocity. The corrected transport velocity formulation considers the additional terms missed by original formulation, thereafter performing better in terms of accuracy of the fluid simulations and at elimination of tensile instability. Smoother pressure distributions is achieved with EDAC formulation.

A contact force model based on DEM is incorporated in the developed updated Lagrangian SPH model (CTVF) to handle the collision between elastic solids. Collision among frictional solids is modeled with the developed solver. Spurious interaction between bodies close by but not touching is eliminated. Collision between bodies of arbitrary shape were simulated to validate the model. Multiple bodies collision, sliding and rolling body cases are considered to validate the model.

The developed solver to model fluid and solid dynamics, CTVF, is extended to solve fluid structure interaction phenomenon. Both the phases are modeled using a single unified scheme and by modeling hydrostatic water column on a clamped beam and dam

breaking flow onto an elastic plate validated. This essentially solved the modeling of the interaction between the high speed jet with the target.

The influence of the jet on the oncoming projectiles is modeled using the coupled CTVF-DEM approach. Here, the interaction among the rigid bodies is handled using the discrete element method.

Erosion.

An opensource formulation.

7.1   Future work

7.1.1   CTVF

The newly proposed method has not been applied to three dimensional problems or to fluid structure interaction (FSI) problems. We believe that the method would be easier to use in the context of FSI since it can handle both fluids and solids in the same formulation. We propose to investigate these in the future.

7.1.2   CSPH

A non-linear contact force model can be implemented in the future work. The current work can be easily extended to the modeling of collision between elastic and elastic-plastic bodies. Also, the collision between the bodies undergoing breakage can be easily captured with the current framework.

7.1.3   FSI

For the future work, we plan to extend the current solver being extended to handle the anisotropic structures and 3D FSI problems.

7.1.4   RFC

For future work, we plan to extend the current solver being extended to handle rigid fluid coupling in multiphase flows. Cavitation induced due to the entry of rigid objects can be studied. The particle-shifting strategy will be helpful in studying the occurring of cavitation due to rigid body entries. Further, the current work can be applied to study biomedical applications, such as red blood cells transport in a non-newtonian fluid flow, impact of arbitrarily shaped rigid objects in fluid flow to note a few.

7.1.5   Erosion

For future work, we plan to extend the current solver being extended to handle rigid fluid coupling in multiphase flows. Cavitation induced due to the entry of rigid objects can be studied. The particle-shifting strategy will be helpful in studying the occurring of cavitation due to rigid body entries. Further, the current work can be applied to study biomedical applications, such as red blood cells transport in a non-newtonian fluid flow, impact of arbitrarily shaped rigid objects in fluid flow to note a few.

7.1.6   Water jet machining

For future work, we plan to extend the current solver being extended to handle rigid fluid coupling in multiphase flows. Cavitation induced due to the entry of rigid objects can be studied. The particle-shifting strategy will be helpful in studying the occurring of cavitation due to rigid body entries. Further, the current work can be applied to study biomedical applications, such as red blood cells transport in a non-newtonian fluid flow, impact of arbitrarily shaped rigid objects in fluid flow to note a few.

References

Adami, S., Hu, X., and Adams, N., 2012 Aug., "A generalized wall boundary condition for smoothed particle hydrodynamics," *Journal of Computational Physics* **231**, 7057–7075.

Adami, S., Hu, X., and Adams, N., 2013 Maya, "A transport-velocity formulation for smoothed particle hydrodynamics," *Journal of Computational Physics* **241**, 292–307.

Adami, S., Hu, X., and Adams, N. A., 2013b, "A transport-velocity formulation for smoothed particle hydrodynamics," *Journal of Computational Physics* **241**, 292–307.

Adepu, D., and Ramachandran, P., 2021, "A corrected transport-velocity formulation for fluid and structural mechanics with sph," *arXiv preprint arXiv:2106.00756* doi: \bibinfo{doi}{10.48550/arXiv.2106.00756}

Adepu, D., and Ramachandran, P., 2022 Aug., "Improved collision handling of elastic solids in SPH using a contact force model," doi:\bibinfo{doi}{10.31224/2503}

Aich, U., Banerjee, S., Bandyopadhyay, A., and Das, P. K., 2014 Jan., "Abrasive Water Jet Cutting of Borosilicate Glass," *Procedia Materials Science*, 3rd International Conference on Materials Processing and Characterisation (ICMPC 2014) **6**, 775–785.

Alberdi, A., SuÃąrez, A., Artaza, T., Escobar-Palafox, G. A., and Ridgway, K., 2013 Jan., "Composite Cutting with Abrasive Water Jet," *Procedia Engineering*, The Manufacturing Engineering Society International Conference, MESIC 2013 **63**, 421–429.

Amicarelli, A., Albano, R., Mirauda, D., Agate, G., Sole, A., and Guandalini, R., 2015, "A smoothed particle hydrodynamics model for 3d solid body transport in free surface flows," *Computers & fluids* **116**, 205–228.

Antoci, C., Gallati, M., and Sibilla, S., 2007, "Numerical simulation of fluid–structure interaction by sph," *Computers & structures* **85**, 879–890.

Antuono, M., Colagrossi, A., Marrone, S., and Molteni, D., 2010, "Free-surface flows solved by means of SPH schemes with numerical diffusive terms," *Computer Physics Communications* **181**, 532–549.

Antuono, M., Sun, P., Marrone, S., and Colagrossi, A., 2021, "The δ-ale-sph model: An arbitrary lagrangian-eulerian framework for the δ-sph model with particle shifting technique," *Computers & Fluids* **216**, 104806.

Aristoff, J. M., Truscott, T. T., Techet, A. H., and Bush, J. W. M., 2010, "The water entry of decelerating spheres," **22**, 032102.

Bearman, P., 2011, "Circular cylinder wakes and vortex-induced vibrations," *Journal of Fluids and Structures* **27**, 648–658.

Belytschko, T., Guo, Y., Kam Liu, W., and Ping Xiao, S., 2000, "A unified stability analysis of meshless particle methods," *International Journal for Numerical Methods in Engineering* **48**, 1359–1400.

Bitter, J., 1963, "A study of erosion phenomena part i," *wear* **6**, 5–21.

Bogaers, A. E., Kok, S., Reddy, B. D., and Franz, T., 2016, "An evaluation of quasi-newton methods for application to fsi problems involving free surface flow and solid body contact," *Computers & Structures* **173**, 71–83.

Bonet, J., and Kulasegaram, S., 2002, "Alternative total lagrangian formulations for corrected smooth particle hydrodynamics (csph) methods in large strain dynamic problems," *Revue Européenne des Éléments Finis* **11**, 893–912.

Bui, H. H., Fukagawa, R., Sako, K., and Ohno, S., 2008, "Lagrangian meshfree particles method (sph) for large deformation and failure flows of geomaterial using elastic–plastic soil constitutive model," *International journal for numerical and analytical methods in geomechanics* **32**, 1537–1570.

Bui, H. H., and Nguyen, G. D., 2021, "Smoothed particle hydrodynamics (sph) and its applications in geomechanics: From solid fracture to granular behaviour and multiphase flows in porous media," *Computers and Geotechnics* **138**, 104315.

Canelas, R. B., Crespo, A. J., Dominguez, J. M., Ferreira, R. M., and Gomez-Gesteira, M., 2016, "Sph–dcdem model for arbitrary geometries in free surface solid–fluid flows," *Computer Physics Communications* **202**, 131–140.

Clausen, J. R., 2013 Jan., "Entropically damped form of artificial compressibility for explicit simulation of incompressible flow," *Physical Review E* **87**, 013309–1–013309–12.

Cleary, P. W., 2010, "Elastoplastic deformation during projectile–wall collision," *Applied Mathematical Modelling* **34**, 266–283.

Cummins, S. J., and Rudman, M., 1999, "An SPH projection method," *Journal of Computational Physics* **152**, 584–607.

Cundall, P. A., and Strack, O. D. L., 1979, "A discrete numerical model for granular assemblies," **29**, 47–65.

Dai, Y., Zhang, Y., and Li, X., 2021 Jan., "Numerical and experimental investigations on pipeline internal solid-liquid mixed fluid for deep ocean mining," *Ocean Engineering* **220**, 108411.

Dalrymple, R. A., and Knio, O., 2001, "Sph modelling of water waves," in *Coastal dynamics' 01*, pp. 779–787.

Das, R., and Cleary, P. W., 2015, "Evaluation of accuracy and stability of the classical sph method under uniaxial compression," *Journal of Scientific Computing* **64**, 858–897.

Dettmer, W., and PeriÄĞ, D., 2006, "A computational framework for fluidâĂŞrigid body interaction: Finite element formulation and applications," A Tribute to Thomas J.R. Hughes on the Occasion of his 60th Birthday **195**, 1633–1666.

Dong, X., Liu, G., Li, Z., and Zeng, W., 2016, "A smoothed particle hydrodynamics (sph) model for simulating surface erosion by impacts of foreign particles," *Tribology International* **95**, 267–278.

Duriez, J., and Bonelli, S., 2021, "Precision and computational costs of level set-discrete element method (ls-dem) with respect to dem," *Computers and Geotechnics* **134**, 104033.

Dyka, C., and Ingel, R., 1995, "An approach for tension instability in smoothed particle hydrodynamics (sph)," *Computers & structures* **57**, 573–580.

Finnie, I., 1972, "Some observations on the erosion of ductile metals," *wear* **19**, 81–90.

Ghia, U., Ghia, K. N., and Shin, C. T., 1982, "High-Re solutions for incompressible flow using the Navier-Stokes equations and a multigrid method," *Journal of Computational Physics* **48**, 387–411.

Gingold, R. A., and Monaghan, J. J., 1977a, "Smoothed particle hydrodynamics: Theory and application to non-spherical stars," *Monthly Notices of the Royal Astronomical Society* **181**, 375–389.

Gingold, R. A., and Monaghan, J. J., 1977b, "Smoothed particle hydrodynamics: theory and application to non-spherical stars," *Monthly notices of the royal astronomical society* **181**, 375–389.

Gray, J. P., Monaghan, J. J., and Swift, R., 2001a, "Sph elastic dynamics," *Computer methods in applied mechanics and engineering* **190**, 6641–6662.

Gray, J., Monaghan, J., and Swift, R., 2001 Oct.b, "SPH elastic dynamics," *Computer Methods in Applied Mechanics and Engineering* **190**, 6641–6662.

Guilkey, J. E., Bardenhagen, S., Roessig, K., Brackbill, J., Witzel, W., and Foster, J., 2001, "Improved contact algorithm for the material point method and application to stress propagation in granular material," doi:\bibinfo{doi}{10.3970/cmes.2001.002.509}

Guo, K., Chen, R., Li, Y., Qiu, S., and Su, G., 2017, "Numerical investigation of the fluid-solid mixture flow using the focus code," *Progress in Nuclear Energy* **97**, 197–213.

He, J., Tofighi, N., Yildiz, M., Lei, J., and Suleman, A., 2017, "A coupled wc-tl sph method for simulation of hydroelastic problems," *International Journal of Computational Fluid Dynamics* **31**, 174–187.

Howell, B., and Ball, G., 2002, "A free-lagrange augmented Godunov method for the simulation of elastic–plastic solids," *Journal of Computational Physics* **175**, 128–167.

Hu, P., Xue, L., Mao, S., Kamakoti, R., Zhao, H., Dittakavi, N., Ni, K., Wang, Z., and Li, Q., 2010, "Material point method applied to fluid-structure interaction (fsi)/aeroelasticity problems," in *48th AIAA aerospace sciences meeting including the new horizons forum and aerospace exposition*, p. 1464.

Huang, C., Long, T., Li, S., and Liu, M., 2019 Sep., "A kernel gradient-free SPH method with iterative particle shifting technology for modeling low-Reynolds flows around airfoils," *Engineering Analysis with Boundary Elements* **106**, 571–587.

Hutchings, I. M., 1977, "The erosion of metals by solid particles-a study using high-speed photography," in *12th Intl Congress on High Speed Photography*, Vol. 97 (SPIE). pp. 358–361.

Islam, M. R. I., Bansal, A., and Peng, C., 2020, "Numerical simulation of metal machining process with eulerian and total lagrangian sph," *Engineering Analysis with Boundary Elements* **117**, 269–283.

Jasak, H., 2007, "Updated lagrangian finite volume solver for large deformation dynamic response of elastic body," *Transactions of FAMENA* **31**, 55.

Karunasena, H., Senadeera, W., Gu, Y., and Brown, R., 2014 Aug., "A coupled SPH-DEM model for micro-scale structural deformations of plant cells during drying," *Applied Mathematical Modelling* **38**, 3781–3801.

Khayyer, A., Gotoh, H., Falahaty, H., and Shimizu, Y., 2018, "An enhanced isph–sph coupled method for simulation of incompressible fluid–elastic structure interactions," *Computer Physics Communications* **232**, 139–164.

Khayyer, A., Gotoh, H., and Shimizu, Y., 2022, "On systematic development of fsi solvers in the context of particle methods," *Journal of Hydrodynamics* **34**, 395–407.

Koshizuka, S., and Oka, Y., 1996, "Moving-particle semi-implicit method for fragmentation of incompressible fluid," *Nuclear science and engineering* **123**, 421–434.

Kruggel-Emden, H., Rickelt, S., Wirtz, S., and Scherer, V., 2008 Dec., "A study on the validity of the multi-sphere Discrete Element Method," *Powder Technology* **188**, 153–165.

Lai, Z., Chen, Q., and Huang, L., 2020, "Fourier series-based discrete element method for computational mechanics of irregular-shaped particles," **362**, 112873.

Landau, L. D., Lifshitz, E. M., Sykes, J. B., Reid, W. H., and Dill, E. H., 1960 Jul., "Theory of elasticity: Vol. 7 of course of theoretical physics," *Physics Today* **13**, 44–46.

Li, X., Yao, J., Sun, Y., and Wu, Y., 2022, "Material point method analysis of fluid–structure interaction in geohazards," *Natural Hazards*, 1–19.

Libersky, L. D., and Petschek, A. G., 1991, "Smooth particle hydrodynamics with strength of materials," in *Advances in the free-Lagrange method including contributions on adaptive gridding and the smooth particle hydrodynamics method* (Springer). pp. 248–257.

Lind, S., Xu, R., Stansby, P., and Rogers, B., 2012, "Incompressible smoothed particle hydrodynamics for free-surface flows: A generalised diffusion-based algorithm for

stability and validations for impulsive flows and propagating waves," *Journal of Computational Physics* **231**, 1499–1523.

Liu, L., and Ji, S., 2020, "A new contact detection method for arbitrary dilated polyhedra with potential function in discrete element method," **121**, 5742–5765.

Llanto, J. M., Tolouei-Rad, M., Vafadar, A., and Aamir, M., 2021 Jan., "Recent Progress Trend on Abrasive Waterjet Cutting of Metallic Materials: A Review," *Applied Sciences* **11**, 3344.

Lozovskiy, A., Olshanskii, M. A., Salamatova, V., and Vassilevski, Y. V., 2015, "An unconditionally stable semi-implicit fsi finite element method," *Computer Methods in Applied Mechanics and Engineering* **297**, 437–454.

Lu, G., Third, J., and Müller, C., 2012, "Critical assessment of two approaches for evaluating contacts between super-quadric shaped particles in dem simulations," *Chemical engineering science* **78**, 226–235.

Lucy, L. B., 1977, "A numerical approach to testing the fission hypothesis," *The Astronomical Journal* **82**, 1013–1024.

Marrone, S., Colagrossi, A., Le TouzÃl', D., and Graziani, G., 2010 May, "Fast free-surface detection and level-set function definition in SPH solvers," *Journal of Computational Physics* **229**, 3652–3663.

Mintu, S., and Molyneux, D., 2018 Nov., "Simulation of ice-structure interactions using a coupled SPH-DEM method," in *Day 1 Mon, November 05, 2018* (OTC).

Mohseni-Mofidi, S., Drescher, E., Kruggel-Emden, H., Teschner, M., and Bierwisch, C., 2021, "Particle-based numerical simulation study of solid particle erosion of ductile materials leading to an erosion model, including the particle shape effect," *Materials* **15**, 286.

Molinari, J., and Ortiz, M., 2002, "A study of solid-particle erosion of metallic targets," *International Journal of Impact Engineering* **27**, 347–358.

Monaghan, J. J., 1994, "Simulating free surface flows with SPH," *Journal of Computational Physics* **110**, 399–406.

Monaghan, J. J., 2005a, "Smoothed Particle Hydrodynamics," *Reports on Progress in Physics* **68**, 1703–1759.

Monaghan, J. J., 2005b, "Smoothed particle hydrodynamics," *Reports on progress in physics* **68**, 1703.

Monaghan, J. J., 2000, "Sph without a tensile instability," *Journal of computational physics* **159**, 290–311.

Monaghan, J. J., 2012, "Smoothed particle hydrodynamics and its diverse applications," *Annual Review of Fluid Mechanics* **44**, 323–346.

Moresi, L., Dufour, F., and Mühlhaus, H.-B., 2003, "A lagrangian integration point finite element method for large deformation modeling of viscoelastic geomaterials," *Journal of computational physics* **184**, 476–497.

Morris, J. P., Fox, P. J., and Zhu, Y., 1997a, "Modeling low reynolds number incompressible flows using sph," *Journal of computational physics* **136**, 214–226.

Morris, J. P., Fox, P. J., and Zhu, Y., 1997b, "Modeling low reynolds number incompressible flows using SPH," *Journal of Computational Physics* **136**, 214–226.

Muta, A., Ramachandran, P., and Negi, P., 2020 Oct., "An efficient, open source, iterative ISPH scheme," *Computer Physics Communications* **255**, 107283.

Natarajan, Y., Murugesan, P. K., Mohan, M., and Khan, S. A. L. A., 2020, "Abrasive water jet machining process: A state of art of review," *Journal of Manufacturing Processes* **49**, 271–322.

Ng, K., Alexiadis, A., Chen, H., and Sheu, T., 2020, "A coupled smoothed particle hydrodynamics-volume compensated particle method (sph-vcpm) for fluid structure interaction (fsi) modelling," *Ocean Engineering* **218**, 107923.

Oger, G., Marrone, S., Le TouzÃl', D., and de Leffe, M., 2016 May, "SPH accuracy improvement through the combination of a quasi-Lagrangian shifting transport velocity and consistent ALE formalisms," *Journal of Computational Physics* **313**, 76–98.

Peng, Y.-X., Zhang, A.-M., and Wang, S.-P., 2021, "Coupling of wcsph and rkpm for the simulation of incompressible fluid–structure interactions," *Journal of Fluids and Structures* **102**, 103254.

Qingyun, Z., Mingxin, Z., and Dan, H., 2022 Jan., "Numerical simulation of impact and entrainment behaviors of debris flow by using SPH–DEM–FEM coupling method," *Open Geosciences* **14**, 1020–1047.

Qiu, L.-C., Liu, Y., and Han, Y., 2017 Jan., "A 3D Simulation of a Moving Solid in Viscous Free-Surface Flows by Coupling SPH and DEM," *Mathematical Problems in Engineering* **2017**, e3174904.

Ramachandran, P., 2016, "PySPH: a reproducible and high-performance framework for smoothed particle hydrodynamics," in *Proceedings of the 15th Python in Science Conference*, edited by Benthall, S. and Rostrup, S., pp. 127–135.

Ramachandran, P., 2018 Sep./Oct.a, "automan: A python-based automation framework for numerical computing," *Computing in Science & Engineering* **20**, 81–97.

Ramachandran, P., 2018b, "automan: A python-based automation framework for numerical computing," *Computing in Science & Engineering* **20**, 81–97.

Ramachandran, P., Bhosale, A., Puri, K., Negi, P., Muta, A., Adepu, D., Menon, D., Govind, R., Sanka, S., Sebastian, A. S., Sen, A., Kaushik, R., Kumar, A., Kurapati, V., Patil, M., Tavker, D., Pandey, P., Kaushik, C., Dutt, A., and Agarwal, A., 2020, "PySPH: a Python-based framework for smoothed particle hydrodynamics," *arXiv preprint arXiv:1909.04504*

Ramachandran, P., and Puri, K., 2015 14th – 17th, July, "Entropically damped artificial compressibility for SPH," in *Proceedings of the 6th International Conference on Computational Methods 5 conference*, Vol. 2, edited by Liu, G. R. and Das, R. (Auckland, New Zealand). p. Paper ID 1210.

Ramachandran, P., and Puri, K., 2019 January, "Entropically damped artificial compressibility for SPH," *Computers and Fluids* **179**, 579–594.

Randles, P., and Libersky, L., 1996 Dec., "Smoothed Particle Hydrodynamics: Some recent improvements and applications," *Computer Methods in Applied Mechanics and Engineering* **139**, 375–408.

Rodrigues, G., Weber, H., and Driemeier, L., 2019, "Elastic and plastic collision comparison using finite element method," *International Journal of Mechanical and Mechatronics Engineering* **13**, 354–358.

Salehizadeh, A., and Shafiei, A., 2022, "A coupled isph-tlsph method for simulating fluid-elastic structure interaction problems," *Journal of Marine Science and Application* **21**, 15–36.

Shao, S., and Lo, E. Y., 2003, "Incompressible sph method for simulating newtonian and non-newtonian flows with a free surface," *Advances in water resources* **26**, 787–800.

Singer, V., Sautter, K. B., Larese, A., Wüchner, R., and Bletzinger, K.-U., 2022, "A partitioned material point method and discrete element method coupling scheme," *Advanced Modeling and Simulation in Engineering Sciences* **9**, 1–24.

Skillen, A., Lind, S., Stansby, P. K., and Rogers, B. D., 2013, "Incompressible smoothed particle hydrodynamics (sph) with reduced temporal noise and generalised fickian smoothing applied to bodyâĂŞwater slam and efficient waveâĂŞbody interaction," *Computer Methods in Applied Mechanics and Engineering* **265**, 163–173.

Sugiura, K., and Inutsuka, S.-i., 2017, "An extension of godunov sph ii: Application to elastic dynamics," *Journal of Computational Physics* **333**, 78–103.

Sulsky, D., Chen, Z., and Schreyer, H. L., 1994, "A particle method for history-dependent materials," *Computer methods in applied mechanics and engineering* **118**, 179–196.

Sun, P., Colagrossi, A., Marrone, S., Antuono, M., and Zhang, A.-M., 2019 Maya, "A consistent approach to particle shifting in the delta - Plus -SPH model," *Computer Methods in Applied Mechanics and Engineering* **348**, 912–934.

Sun, P., Colagrossi, A., Marrone, S., and Zhang, A., 2017, "The δplus-sph model: Simple procedures for a further improvement of the sph scheme," *Computer Methods in Applied Mechanics and Engineering* **315**, 25–49.

Sun, W.-K., Zhang, L.-W., and Liew, K., 2020, "A smoothed particle hydrodynamics–peridynamics coupling strategy for modeling fluid–structure interaction problems," *Computer Methods in Applied Mechanics and Engineering* **371**, 113298.

Sun, Y., Xi, G., and Sun, Z., 2019b, "A fully lagrangian method for fluid–structure interaction problems with deformable floating structure," *Journal of Fluids and Structures* **90**, 379–395.

Swegle, J. W., Hicks, D. L., and Attaway, S., 1995, "Smoothed particle hydrodynamics stability analysis," *Journal of computational physics* **116**, 123–134.

Takaffoli, M., and Papini, M., 2009, "Finite element analysis of single impacts of angular particles on ductile targets," *Wear* **267**, 144–151.

Thornton, C., Cummins, S. J., and Cleary, P. W., 2011, "An investigation of the comparative behaviour of alternative contact force models during elastic collisions," *Powder Technology* **210**, 189–197.

de Vaucorbeil, A., and Nguyen, V. P., 2021, "Modelling contacts with a total lagrangian material point method," *Computer Methods in Applied Mechanics and Engineering* **373**, 113503.

Vignjevic, R., Reveles, J. R., and Campbell, J., 2006, "Sph in a total lagrangian formalism," *CMC-Tech Science Press-* **4**, 181.

Vyas, D. R., Cummins, S. J., Rudman, M., Cleary, P. W., Delaney, G. W., and Khakhar, D. V., 2021, "Collisional sph: A method to model frictional collisions with sph," *Applied Mathematical Modelling* **94**, 13–35.

Wachs, A., Girolami, L., Vinay, G., and Ferrer, G., 2012, "Grains3d, a flexible dem approach for particles of arbitrary convex shapeâĂŤpart i: Numerical model and validations," *Powder technology* **224**, 374–389.

Walkley, M. A., Gaskell, P. H., Jimack, P. K., Kelmanson, M. A., and Summers, J. L., 2005, "Finite element simulation of three-dimensional free-surface flow problems," **24**, 147–162.

Williamson, C. H., Govardhan, R., *et al.*, 2004, "Vortex-induced vibrations," *Annual review of fluid mechanics* **36**, 413–455.

Wu, K., Yang, D., and Wright, N., 2016, "A coupled sph-dem model for fluid-structure interaction problems with free-surface flow and structural failure," *Computers & Structures* **177**, 141–161.

Xu, R., Stansby, P., and Laurence, D., 2009a, "Accuracy and stability in incompressible sph (ISPH) based on the projection method and a new approach," *Journal of Computational Physics* **228**, 6703–6725.

Xu, R., Stansby, P., and Laurence, D., 2009b, "Accuracy and stability in incompressible sph (isph) based on the projection method and a new approach," *Journal of computational Physics* **228**, 6703–6725.

Yan, R., Bi, Y.-q., and Jiang, W., 2021, "Simulation of contact interface between elastic solids using smoothed particle hydrodynamics," *Computational Particle Mechanics*, 1–11.

Ye, T., Pan, D., Huang, C., and Liu, M., 2019, "Smoothed particle hydrodynamics (SPH) for complex fluid flows: Recent d evelopments in methodology and applications," *Physics of Fluids* **31**, 011301.

Zang, X., Cao, X., Zhang, J., Xie, Z., Xiong, N., Darihaki, F., and Bian, J., 2022, "Investigation of surface damage of ductile materials caused by rotating particles," *Wear* **488**, 204185.

Zhan, L., Peng, C., Zhang, B., and Wu, W., 2019, "A stabilized tl–wc sph approach with gpu acceleration for three-dimensional fluid–structure interaction," *Journal of Fluids and Structures* **86**, 329–353.

Zhan, L., Peng, C., Zhang, B., and Wu, W., 2021, "A surface mesh represented discrete element method (smr-dem) for particles of arbitrary shape," *Powder Technology* **377**, 760–779.

Zhang, C., Hu, X. Y., and Adams, N. A., 2017a, "A generalized transport-velocity formulation for smoothed particle hydrodynamics," *Journal of Computational Physics* **337**, 216–232.

Zhang, C., Hu, X. Y. T., and Adams, N. A., 2017b, "A generalized transport-velocity formulation for smoothed particle hydrodynamics," *Journal of Computational Physics* **337**, 216–232.

Zhang, S., Kuwabara, S., Suzuki, T., Kawano, Y., Morita, K., and Fukuda, K., 2009 Apr., "Simulation of solidâĂŞfluid mixture flow using moving particle methods," *Journal of Computational Physics* **228**, 2552–2565.

List of Publications

Put your publications from the thesis here. The packages `multibib` or `bibtopic` or `biblatex` or enumerate environment or thebibliography environment etc. can be used to handle multiple different bibliographies in the document.